AN ABSTRACT OF THE DISSERTATION OF

Benjamin M. Adam for the degree of Doctor of Philosophy in Materials Science presented on May 11, 2018.

Title: Characterization and Development of Ni-based Superalloys for Supercritical Carbon Dioxide Applications.

Abstract approved: _____

Julie D. Tucker

The advent of supercritical CO_2 as a new heat-exchange medium has seen strong interest from the power industry and the energy research field recently. It is advantageous in comparison with other heat-exchange cycles, as it can be operated safely at much higher temperatures and pressures, thus increasing the thermal efficiency greatly. In turn, the system size can be reduced and CO_2 emissions lowered. In general, the process conditions are temperatures of up to 700 ℃ and pressures of up to 30 MPa. Here, only high-temperature alloys, such as Ni-based superalloys, are a viable option. However, there is a lack of knowledge and information on the performance of such materials in an sCO_2 environment. Therefore, a thorough understanding of the alloy systems that are targeted for use in sCO_2 applications is necessary, from their corrosion performance and their workability into heat-exchanger parts to the conception of custom-designed alloys. In this work, commercially available, candidate

alloys were investigated for their corrosion behavior under sCO_2 conditions, and the influences on the microstructure analyzed. The results were compared for different exposure times, and with other environments, in order to understand the particular effect of sCO_2. Next, the hot-working behavior of selected Ni-based superalloys was analyzed, where the deformation conditions during the fabrication process were mimicked. This aided in outlining safe and efficient working zones for materials to be formed. Lastly, development of novel alloy systems for sCO_2 use was pursued, where the design criteria were based on the high temperature strength and corrosion performance of the most promising commercially available alloys. Optimization of the alloy was performed through thermodynamic modeling, heat-treatment and characterization, allowing the final composition to be cast and hot-rolled. Mechanical testing results suggested very promising properties which compare well with other commercially available alloy systems.

Characterization and Development of Ni-based Superalloys for Supercritical Carbon Dioxide Applications.

by

Benjamin M. Adam

A DISSERTATION

submitted to

Oregon State University

in partial fulfillment of
the requirements for the
degree of

Doctor of Philosophy

Presented May 11, 2018
Commencement June 2018

Doctor of Philosophy dissertation of Benjamin M. Adam presented on May 11, 2018.

APPROVED:

Major Professor, representing Material Science

Head of the School of Mechanical, Industrial and Manufacturing Engineering

---

Dean of the Graduate School

I understand that my dissertation will become part of the permanent collection of Oregon State University libraries. My signature below authorizes release of my dissertation to any reader upon request.

Benjamin M. Adam, Author

ACKNOWLEDGEMENTS

I would like to first express my sincere gratitude and appreciation to my advisor, Dr. Julie Tucker, who guided me with lots of patience and encouragement along a very exciting pathway. Further, I would like to thank Dr. Líney Árnadóttir[d] for her time and willingness to troubleshoot and to provide valuable suggestions. Thanks also to my committee members, Dr. Melissa Santala and Dr. Donghua Xu, who both gave me very useful help and critical advise when it was much needed.

I am greatly indebted to my supervisors Dr. Graham Tewksbury and Dr. William Wood at Portland State University, for enabling this opportunity, supporting me financially, academically and with the time and space flexibility I needed. Dr. Paul Jablonski from NETL in Albany has also been a tremendous help with technical questions and understanding the basics of alloy development. I would like to thank Robert (Bob) Turpin, for his tireless efforts in working on the melting equipment, and valuable advice on all things alloymaking. I am very grateful to Dr. George Young for useful insight and correction during proofreading of the hot deformation work.

Furthermore, I would also like to thank all the other graduate students in the Nuclear Materials group at OSU for their help, critical input and making this a very enjoyable journey.

I would like to especially thank my parents, though far away, have supported me always, and in the end, allowed me to get to this point in the first place.

Last but not least, I am deeply grateful to my wife Jamie, who put up with countless late nights, but continued to give me encouragement, mental and moral

fortitude, all the way to the end. And, of course, to my daughter Pauline, who may not have known yet why her father always had to work late. I am dedicating this thesis to both of you, with love.

TABLE OF CONTENTS

Page

TABLE OF CONTENTS (continued)

Page

LIST OF FIGURES

Figure Page

LIST OF FIGURES (continued)

LIST OF FIGURES (continued)

LIST OF FIGURES (continued)

LIST OF TABLES

LIST OF TABLES (continued)

Table Page

Chapter 1: Introduction

Power generation systems are vastly complex and specific to the different sources of energy, such as coal, gas, nuclear or solar energy. In each case, the goal is to transfer the heat generated, as efficiently as possible, to a carrier medium, which in turn delivers it to power-generating turbines. Traditionally, these cycles have either been the steam Rankine or Brayton cycles, operating at temperatures around 300 ℃. Basic thermodynamics indicate that increasing temperatures will result in an increase in conversion efficiency and fuel-saving. Recently, the supercritical CO_2 (sCO_2) Brayton cycle has been identified as a promising candidate cycle for such a high temperature heat conversion process. In comparison with traditional steam cycles, it operates at temperatures of 550 ℃ - 800 ℃ and pressures of 20-30 MPa. Due to its low critical point for entering the supercritical state, sCO_2 can be utilized during the entire cycle, without enthalpy losses due to phase changes, improving its thermal efficiency. Further advantages and drivers of this technology are are the reduced system size and complexity. In turn, CO_2 emissions can be significantly lowered, overall leading to significant economic and environmental advantages. Employed in a sodium-cooled fast reactor, it also removes the danger of potential catastrophic reaction between liquid sodium and water steam.

However, an increase in temperature will also lead to exponentially faster corrosion processes and other material degradation phenomena, such as reduced creep

life and allowable ultimate stress limits. The effect of exposure in air and steam at high temperatures for heat-resistant austenitic steels and Ni/NiFe- or Co-based alloys is well documented. However, there is sparse comparable data for exposure in sCO_2. This presents a particular challenge since the effects from the supercritical fluid and temperature could potentially involve excessive oxidation and breakaway corrosion, oxide spallation and internal carburization, as well as creep-rupture, and stress-corrosion cracking phenomena. All of these phenomena can severely affect the viability of the sCO_2 cycle and/or reduced the lifetime and integrity of components and parts involved in the heat exchanger systems.

The knowledge gap in materials performance therefore demands the formation of an encompassing database of exposure results and material behavior under sCO_2 conditions, determining the characteristics of suitable candidate materials for optimal use in sCO_2. It also necessitates a more fundamental understanding of the surface processes, primarily oxidation and carburization taking place when materials are being exposed to this particular environment. This involves knowledge of atomic scale interactions, such as molecular dissociation and activation barriers as well as migration of atoms and species into the base-metal, while taking the effects of various alloying elements into account. Insight gained from these fundamental studies can help determine the viability of existing alloys and lay the basis for the development of specifically designed alloy combinations to meet the material needs.

Based on the factors and motivation outlined above, the objectives of this work can be stated, as follows. The chapters associated with the respective objectives are mentioned as well.

The first objective was to evaluate the corrosion performance of commercial alloys, this is presented in chapters 2 and 3. For this, commercially available target alloys, selected based on their established performance in comparable high temperature oxidation conditions, were exposed by utilizing the unique, custom-designed sCO_2 autoclave, present in OSUs Nuclear Materials and Metallurgy Laboratory. Subsequently, the corrosion behavior of the materials, as well as their microstructures and the chemical makeup of their scales and base-metals, were characterized. The goal is to build comprehensive, unbiased and verifiable datasets, consisting of microstructural, corrosion and mechanical characterization, together with the exposure results from partner institutions.

The second objective was to investigate the mechanical properties at elevated temperatures of selected commercial alloys, which is presented in chapter 4. The approach used was thermal-mechanical testing at various temperatures and strain rates, the results represented an important part in ensuring the final mechanical properties were met. The data obtained here informed the hot workability of the model alloys, which is used in designing hot-processing maps that allow for safe hot-working at minimal stress and prevention of cracking. This work was performed using isothermal hot-compression testing, which allow for studying the influence of strain rate, strain and temperature on the deformation behavior.

The third objective was the development of new alloys for sCO_2-applications, this is presented in chapter 5. The model alloys are developed based on the metallurgical features necessary to satisfy the sCO_2 needs, these being both high temperature tensile strength and creep-rupture strength, and superior corrosion resistance. The capabil-

ity to manufacture and fabricate alloys from pure starter material to final wrought product ensures control of all metallurgical parameters and structure-property relationships that can influence corrosion behavior.

Chapter 2: Effects of corrosion in supercritical CO_2 on the microstructural evolution in 800H alloy

Benjamin Adam[a,b], Lucas Teeter[a], Jacob Mahaffey[c], Mark Anderson[c], Líney Árnadóttir[d], and Julie D. Tucker[a]

[a]Department of Mechanical, Industrial and Manufacturing Engineering, Oregon State University, Corvallis, Oregon 97331

[b]Department of Mechanical and Materials Engineering, Portland State University, Portland, Oregon, 97201

[c]Engineering Physics, Department of Engineering, University of Wisconsin-Madison, Madison, Wisconsin

[d]School of Chemical, Biological and Environmental Engineering, Oregon State University, Corvallis, Oregon 97331

Accepted with revisions to Oxidation of Metals on 12/5/2017

This study investigates corrosion of Fe-Ni-based alloy 800H, that were exposed to supercritical CO_2 (sCO_2), ambient air, and argon gas at pressures up to 20 MPa, at 650 ℃ and 750 ℃ for up to 1000 hrs. This alloy and other comparable metal alloys are expected to be used in sCO_2 heat exchanger cycles as proposed in the DOE Advanced Ultra-Supercritical (A-USC) program. Alloy 800H is considered for this application,

because it meets the high temperature strength and creep rupture requirements and is a lower cost alternative to other Ni-based alloys. The oxidation performance and microstructural changes due to exposure in sCO_2 have been evaluated and compared with exposures in air and Ar. The 800H alloy showed similar oxide scale thicknesses in sCO_2 as in air. A recrystallized zone was observed beneath the oxide formed in air and sCO_2. No such zone was observed after exposure to Ar, suggesting this recrystallization was associated with the oxidation process and not simply an effect of surface finishing. A wider recrystallized zone was observed underneath the oxide formed in sCO_2 than in air. The effect of air and sCO_2 on internal oxidation and carburization was investigated as well, showing that air led to more internal oxidation but less internal carburization than sCO_2. It was concluded that the carbon species provided by the sCO_2 atmosphere in conjunction with the increased grain boundary density in the recrystallized zone allowed for more ingress of carbon into the base-metal, which resulted in a higher densities of carbides beneath the oxide scale.

KEYWORDS

Alloy 800H; oxidation; carburization; supercritical CO2; recrystallization

2.1 Introduction

Recent developments in heat exchanger technology have led to the conception of Brayton cycles designed for using supercritical CO_2 (sCO_2) as the working fluid in current and future energy systems. This fluid offers higher thermal efficiency due to its thermophysical properties and the lack of entropy losses from phase changes during the expansion/compression cycles [1]. It also allows for reduction in machinery size, which adds to the thermal efficiency gains [2, 3]. This in turn defines the requirements for the materials to be used in this environmenthigh-temperature structural stability, strength, and corrosion resistance. For longer exposure times, where creep rupture strength and oxidation resistance are key, the choice usually falls on Fe-Ni or Ni-based superalloys. These alloys show superior oxidation resistance over Fe-based alloys, both austenitic and ferritic [4, 5]. Corrosion effects of metals in sCO_2 may differ from those known to occur in air or steam, and may also include carburization phenomena, all of which is the subject of current research [4, 6–10].

Incoloy 800H was designed in the 1950s as a lower Ni-content superalloy to serve the power and energy industry, and has seen significant use in the subsequent decades. It shows moderately high creep rupture strength and high temperature corrosion properties and strength [11]. In recent times, 800H has been selected as one of the candidate materials for the Gen IV nuclear reactor initiative [12] due to its combination of a cost-efficient matrix along with a high amount of alloyed Cr to withstand the exposure conditions in service. Its direct application makes it a competitive alloy to Haynes 230 and 617 for heat exchanger systems, such as tubes, helical coils, and

semi-circular channels [2]. While 800H has been extensively studied in high temperature and hot corrosion environments, such as reheater tubes and furnace components [11], its performance during service exposure in sCO_2 environments is still relatively unknown. For this study, 800H samples were exposed to sCO_2 and then analyzed for their microstructural changes, oxide growth, morphology, and effects of carburization. To evaluate the effect of heat-treatment only, as a reference state, 800H samples were annealed in pure argon gas. In order to compare the effects of different oxidizing environments, samples were also exposed to air following the same time-temperature cycle.

2.2 Methodology

A 12.7 mm thick plate of 800H was acquired from Inco Alloys International, Huntington, WV, in descaled and annealed condition; the chemical specification is listed in Table 1. Coupons of as-received commercially available 800H material were cut into coupons of dimensions 25.4 mm x 25.4 mm x 3 mm (W x L x H). The coupons were ground to a 600 grit finish. Exposure took place in research grade sCO_2 (99.999%) at 20 MPa at 650 ℃ and 750 ℃ for times between 200 and 1000 hrs at the University of Wisconsin-Madison. Additional coupons, used as reference samples, were exposed to air and argon at ambient pressure, at 650 ℃ for 200 and 600 hrs at Oregon State University. The exposures in air were performed in a Leco open tube furnace in ambient pressure and still air. The samples were placed in an alumina boat for easy transfer. Temperature was controlled by a type-K shielded thermocouple, centered in the tube.

Exposures in argon were performed by encapsulation, of an as-received coupon, in glass and vacuum-sealed. Pure zirconium metal was used as an oxygen getter during the heat-treatment. Incremental weight change analysis was performed on all samples after exposure at each time interval. Glancing-angle XRD measurements on the surfaces of the exposed samples were performed using a Rigaku Ultima IV with a 3kW Cu Kα source, to study the oxide structures and electron microscopy was then used to image the surface oxide films. Afterwards, the coupons and their oxide films were protected from mechanical abrasion and wear by applying a two-step coating process of gold-sputter coating, followed by electrodeposition of copper. Samples were then hot-mounted conductively and polished to a 0.04 μm finish using colloidal silica. Cross-sectional characterization of the oxide film and the base-metal underneath was performed using SEM-EDS, -EBSD using a 20kV Zeiss Sigma FEG-SEM as well as TEM-EDS, using a 200kV FEI Tecnai F20 STEM and FEI Titan 80-200 STEM. Results were optimized and beam-calibrated against a Cu-standard, achieving a $\pm$ 1-2 wt-% spectrum accuracy. TEM thin film liftouts were performed using a FEI Strata DB237. TEM image acquisition was performed using bright-field TEM and High-Angle Annular Dark Field scanning TEM. Electron backscatter diffraction (EBSD) acquisition was performed with 8x8 binning at 15kV and a step size of 50 nm, with indexing using a general HKL fcc pattern for austenitic metals.

Table 2.1: Alloy composition of 800H as received from Inco alloys International and nominal composition [11].

[wt-%]	Ni	Cr	Fe	C	Al	Ti	Si	Cu	S
Actual	33.17	19.63	44.89	0.06	0.46	0.53	0.29	0.2	≤ 0.001
Nominal	30.0-35.0	19.0-23.0	39.5-min.	0.05-0.10	0.15-0.60	0.15-0.60	1.00 max.	0.75 max.	0.015 max.

2.3 Results

The phases present in the temperature range of exposure were predicted by modeling in ThermoCalc ® 2015a with the TCFe database and are shown in Figure 2.1. It is noteworthy, that no Cr-carbide phases are predicted, solely the high-temperature TiC phase is stable, at a mass fraction of 0.03 over the entire temperature range. Further, both σ-phase and αCr are predicted, with the αCr phase stable below 600 ℃ and the σ-phase between 575 ℃ and 675 ℃.The high-Cr bcc-type αCr phase is commonly found in high Cr Ni-base alloys and stainless steels, often associated with brittleness and reduced mechanical properties [13].

The XRD results for the sCO_2 exposed samples and the as-received (AR) reference sample, along with identified matches found in the International Centre for Diffraction Data (ICDD) for γ-austenite (PDF. 00-031-0619), Fe_3O_4 / magnetite (PDF. 00-001-1111), Fe_2O_3 / hematite (PDF. 01-085-0599) and Cr_2O_3 / chromia (PDF. 00-001-1294) are presented in Figure 2.2. In general, there is good agreement between all peaks of the as-received and the exposed samples experimentally determined and predicted. For the as-received sample, only the austenite reflections are identified positively, with the major peaks at 43.47°, 50.67°, 74.68°, and minor at 90.67°. For both the 200 and

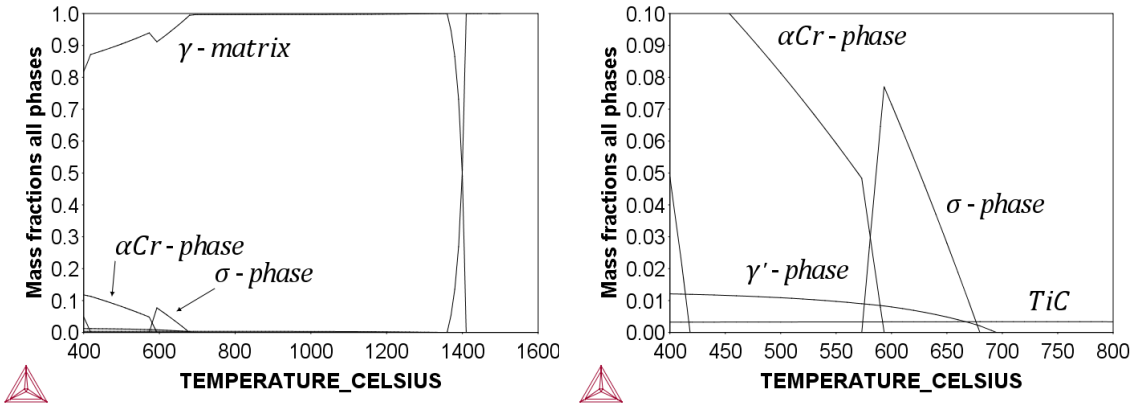

(a) (b)

Figure 2.1: Equilibrium phase diagrams of 800H (actual composition) modeled with ThermoCalc ®.

600 hrs exposed samples, multiple additional peaks were observed and identified as oxide phases. For the 200 hrs sample, mainly Fe_3O_4 was found with its major peaks at 35.45 °, 57.17 ° and 62.73°. Cr_2O_3 and Fe_2O_3 were present as well, however, they were more difficult to clearly separate. Cr_2O_3 was identified by its lower order, high angle peak at 96 ° - albeit sharing its location with a peak for the austenite phase - since it has higher intensity than expected for the austenite phase alone, based on the relative peak intensities for austenite. All other peaks observed are collocated and are positively identified for either both Fe_2O_3 and Fe_3O_4, or one of them, making clear identification difficult. The overall amount of Cr_2O_3 is relatively small in comparison with the other oxide phases. Fe_2O_3 phase does not become distinct until the 600 hrs exposure sample, where its major peaks at 33.14 ° and 35.61 ° can be identified. This is partially due to the decrease in intensity of both Fe_3O_4 and Cr_2O_3, as indicated by their smaller main peaks. An interesting point to note, is that an increase in the

intensity for an austenite peak at 90.67 ° is visible, but not for the main peak at 43.47 °, changing the expected ratio between them. This was not fully explained at this point and may require additional investigation.

When comparing the findings from the weight change analysis in Figure 2.3 it is apparent that the samples exposed in sCO_2 at 750 ℃ showed roughly four times more weight gain than samples exposed at 650 ℃. At the same time, the samples at 750 ℃ also showed a much steeper relative mass gain rate. The confidence intervals were comparable between both temperatures.

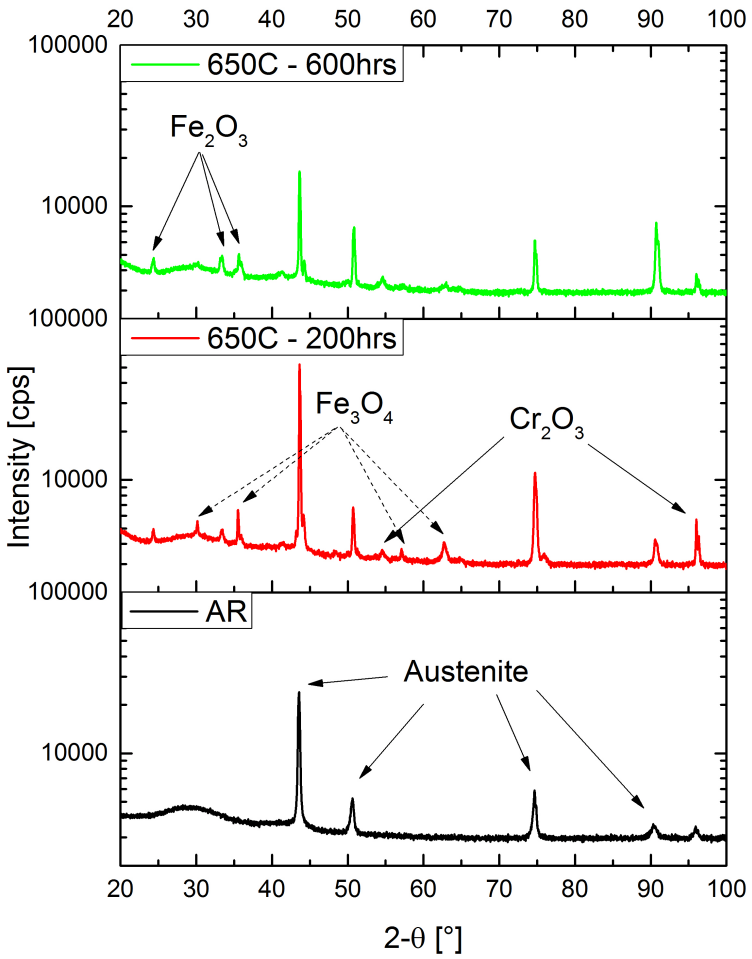

Figure 2.2: XRD results for $20° < \theta < 90°$ using grazing angle method for 800H coupon surfaces exposed at 650 ℃ in sCO_2 for 200 and 600 hrs. A reference spectrum for the as-received sample surface (AR) is included for comparison

SEM characterization of the 800H surface showed various types of oxide morphologies present for different exposure times, seen in Figure 2.4. At lower magnifications, both surfaces appear covered with a thin film as well as single or clustered oxide nod-

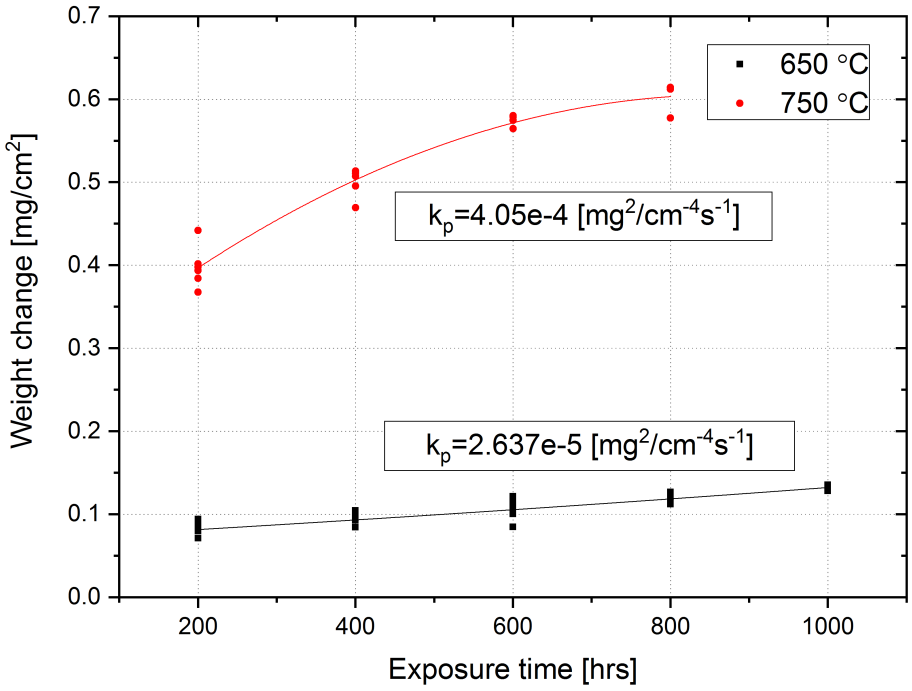

Figure 2.3: Weight change for exposed 800H at 650 ℃ and 750 ℃ in sCO_2.

ules. The oxide phases size and distribution at 200 h exposure show large clusters, which also tend to overlap. They generally have a faceted appearance, with sharp edges and plane faces. At 600 h exposure, the oxides appear to be less densely populated and form individual islands, while their appearance is less faceted and more irregular, showing no specific shape anymore. The cross-sectional analysis of the samples exposed in sCO_2 for 200 and 600 h is shown in Figure 2.5. Here the backscatter detector was operated in its inverted mode, allowing the amplification of the signal coming from the scale, which otherwise appear darker, to appear brighter. In general, the oxide scale was continuous and adherent at all locations that were inspected. Due to the selective oxidation of Cr that occurred during exposure, a Cr-depleted region

forms underneath the main oxide scale. The oxide thickness was constant at around 0.5 µm, and did not vary significantly with exposure time. Localized acceleration of the oxidation reaction by faster diffusion pathways, local mechanical failure or other imperfections can lead to deeper penetration of the oxide into the substrate, termed oxide pegs or protrusions. The samples exposed for 600 hrs showed significantly more oxide protrusions or oxide pegs, growing from the scale into the base-metal. Further, presence of a layer of recrystallized (RX) grains underneath the oxide was found, in both 200 h and 600 h exposed samples.

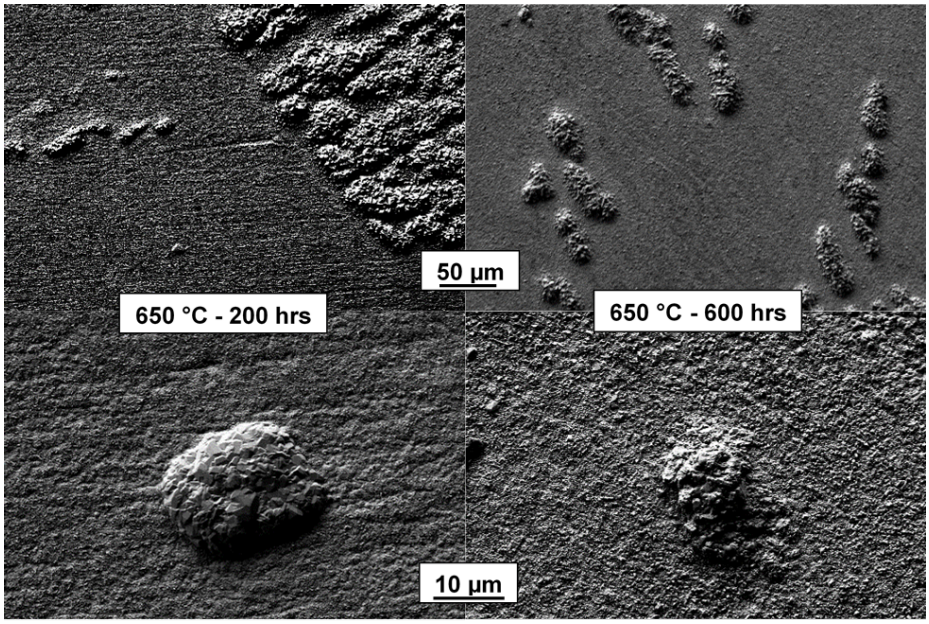

Figure 2.4: Oxide morphologies on surfaces of 800H exposed in sCO_2 at 650 ℃ for 200 and 600 hrs imaged with SEM.

Figure 2.5a and b are representative EDX linescans profiling the scale and the underlying base-metal. The EDX results show that the Cr depletion extends up to

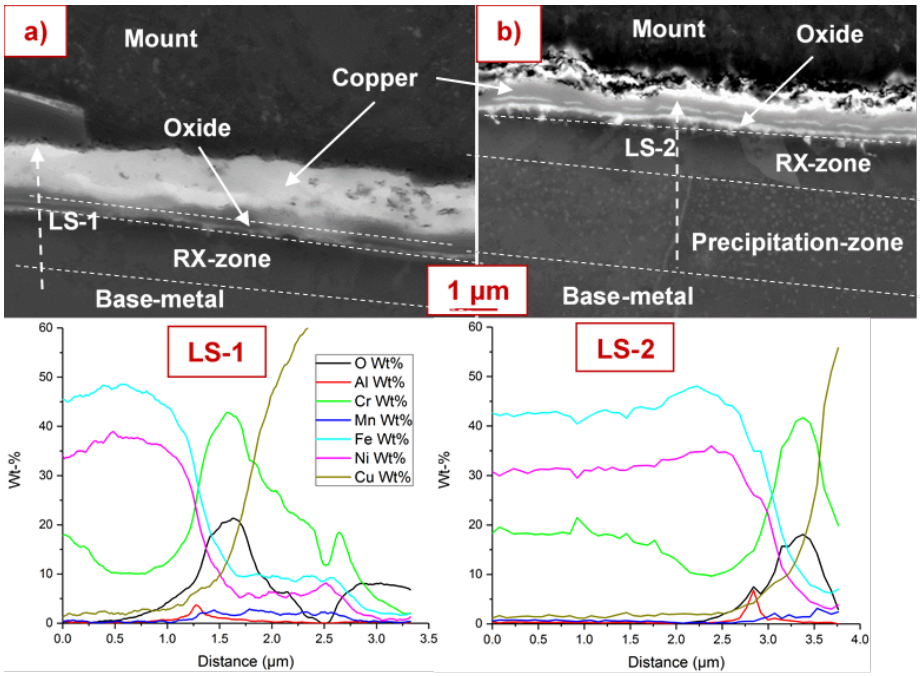

Figure 2.5: a) 800H exposed at 650 ℃ for 200 hrs and b) at 600 hrs, with EDS linescan locations indicated; note that the inverted contrast for the backscattered detector is resulting in the oxide scale to appear brighter than the matrix.

1.5 µm beneath the main scale for both exposure times. Similarly, the enrichment of Ni and Fe in the zone underneath the oxide phase did not change with time, indicating little influence by the prolonged exposure. It is noteworthy, that much of the Cr-depletion zone is collocated with the RX zone, as seen in the EDX-linescans and their corresponding location markers in Figure 2.5a,b. The oxide scales that developed for both exposure times appeared to be a mixture of an inner and outer layer. The scale composition appears to be Cr_2O_3, while there are traces of Fe and Ni present as well. Additionally, there are indications of an inner Al_2O_3 layer in between the main oxide scale and the substrate, seen in both Figure 2.5 and Figure

2.6. This Al-oxide phase has also been identified to be the makeup of the oxide pegs and protrusions beneath the main scale.

The oxide scale and the underlying matrix were characterized using TEM cross-sections and EDS chemical profiles, as seen in Figure 2.6 for 800H exposed at 750 ℃ for 600 hrs. The profiles clearly show the Cr_2O_3 layer, here without any indications of Fe or Ni participation, however Mn was found to be present in the main oxide. Mn was not found to be present to any significant degree in the base-alloy. It is believed to be a contamination from other metallic samples, which were exposed at the same time in the autoclave. Noteworthy was the finding of an internal precipitation of Al_2O_3, lining what is thought to be the grain boundary of a newly formed grain. This suggests a continued growth of this phase as compared with the lower temperature and shorter exposure time runs.

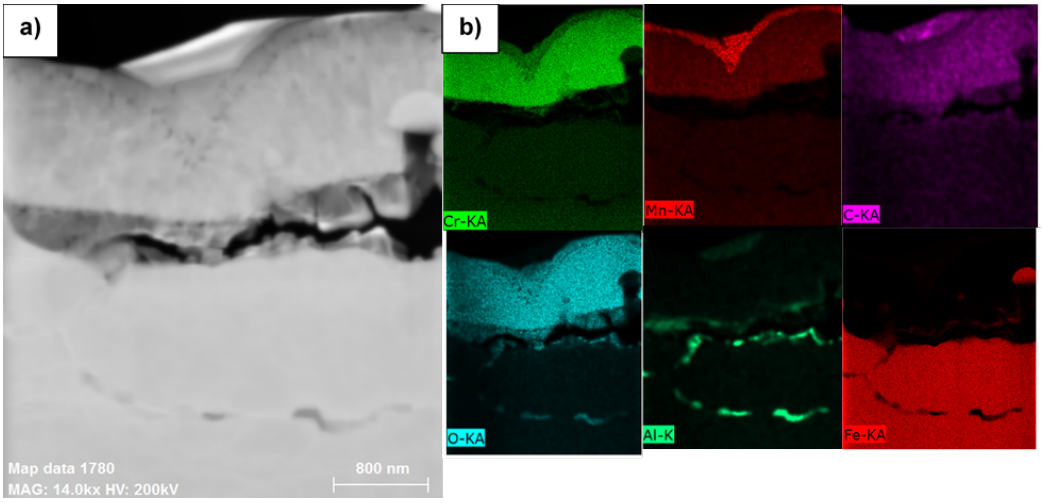

Figure 2.6: a) STEM overview of oxide scale and underlying base metal matrix for 800H exposed for 600 hrs at 750 ℃ and b) corresponding EDS maps for the same region.

Characterization of exposures done in argon at 650 ℃ for 600 hrs showed no visible oxidation products on the surface, and, the SEM-EDX linescans of the cross-section did not show any corrosion products. Further, the argon-exposed sample did not show any signs of recrystallization or sub-size grain formation as was seen for 800H samples exposed to sCO_2, when investigating multiple randomly chosen location along the surface. The subsurface microstructure showed negligible grain boundary precipitation of carbide phases and an absence of any internal oxide. The results for the argon-exposed samples are not presented herein.

The oxidation experiments of 800H in air at 650 ℃for 200 h yielded a generally oxidized sample with a visually adherent oxide film. A mixed Cr-Ni-Fe-oxide scale, as also found in the sCO_2 exposed samples, was identified in the cross-sectional analysis, shown in Figure 2.7. Additionally, the presence of a uniform distribution of internal oxides and carbides was confirmed underneath the scale. When compared with the sCO_2-exposed sample, at the 200 h time interval, the air-exposed sample showed more oxide pegs, but a thinner oxide film, at around 350 nm. At the 600 h exposure time in air, see Figure 2.7b, the material had developed a similar scale thickness as seen after 600 h in sCO_2. At the same time, there was a noticeable increase in breakaway oxidation sites, where large-scale oxide growth inwards had taken place, when compared to the 200 hrs test. This was assumed due to presence of wider and deeper oxide protrusions beneath the metal/oxide interface, as seen in Figure 2.7b in the left and right top corner.

Beneath the recrystallized zone, a region with a significant number of secondary phases was found. Analysis of the secondary phases was performed in the matrix

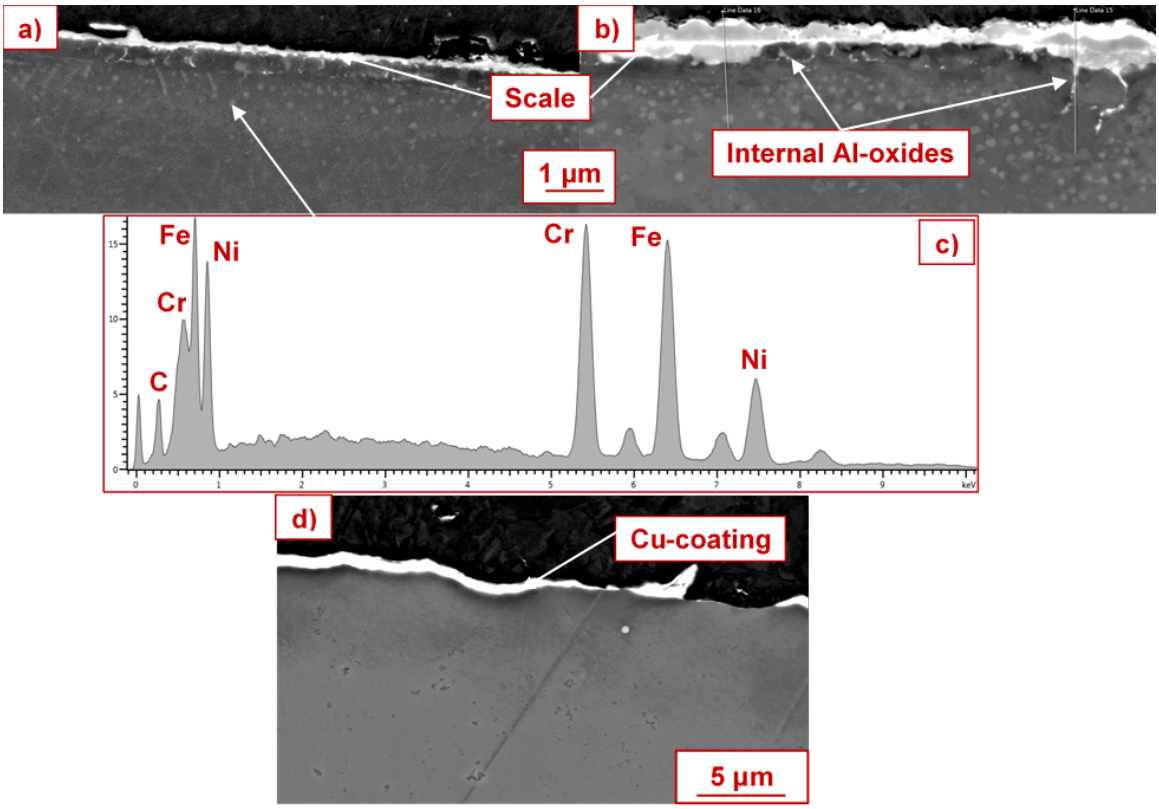

Figure 2.7: Cross-sections of 800H exposed to air for at 650 ℃ at a) 200 hrs and b) 600hrs, showing scale growth and internal oxidation.

below the Cr-depleted zone and along the grain boundaries. A broad zone, of a few μm, with a high density of phases was observed for both exposure times at 650 ℃ in sCO_2, see Figure 2.5, where these phases, by their contrast in BSE, seem lighter than the surrounding matrix. EDS spot scans suggested a relatively higher presence of C and Cr in these phases than in the surrounding matrix. Secondary phases were found along and within grain boundaries, both close to the surface and farther away, as seen in Figure 2.8 and EDX spot scan results in Table 2.2. While EDX

results were not quantitative in terms of the C levels, they indicate the presence of a Cr-enriched carbide phase, presumed to be $M_{23}C_6$, at the grain boundaries as well as intragranularly underneath the recrystallized zone. There was no further carbide precipitation of this magnitude, either inter- and intragranularly, found within the matrix beyond the precipitation zone at the surface. The only other carbide phase found were sparsely distributed MC,N type primary carbo-nitrides, mostly (Ti,Nb)(C,N), formed during solidification, see Figure 2.8d. In addition, there were signs of characteristic σ-phase precipitation from the grain boundaries, seen in Figure 2.8b, which was predicted to be present in the temperature range between 550 ℃ and 700 ℃, from Figure 2.1. The depths of carbide attack changed between the 200 and 600 h exposure in sCO_2, from $\sim 1.5\mu m$ to $\sim 2\mu m$, respectively, as evident from Figure 2.5. The chemical compositions of the carbides seen in the 200 h test were comparable to the ones shown in Table 2.2 and observed for the 600 h exposure test.

In the case of the air-exposure, the samples showed a similar microstructure, with a recrystallized zone beneath the oxide layer, followed by a zone of higher density of secondary phases. The composition of the phases found in the air-exposed samples was comparable to the ones found in the sCO_2 samples, identified as carbides, as seen in Table 2.2. The widths of the carbide zones were found to be $\sim 1\mu m$ for 200 h and $\sim 1\mu m$ for 600 h exposure, thus half the width of the carbide zone in the 200 h sCO_2 samples. The matrix beneath the precipitation zone showed the same microstructure as found beneath the precipitation zone in sCO_2 samples, with no change with longer exposure time. The presence of both the grain boundary carbides and the σ-phases could not be confirmed for the air-exposed samples.

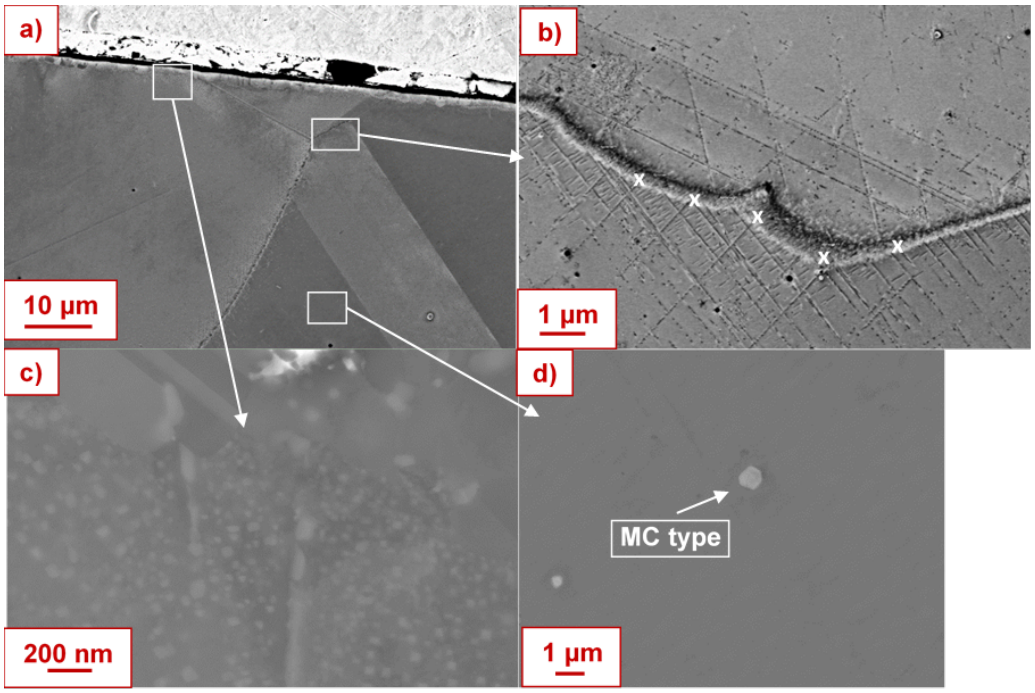

Figure 2.8: a) BSE image of 800H exposed for 600 hrs at 650 ℃in sCO_2 and a close-up of selected grain boundary in b) showing carbide precipitation on grain boundary with EDX spot scans indicated by an x. c) Close-up of the precipitation zone and d) intragranular carbides in the matrix beneath the precipitation zone.

The recrystallization layer underneath the oxide was studied using EBSD, shown for all samples exposers in Figure 2.9. The image quality map used, showed well the quality of the pattern collected for the purposes of indexing and resolution. Both samples exposed in sCO_2 show a continuous layer of 1-2 μm large grains, which, based on previous EDX results, suggested a zone of matrix grains with lower Cr content. Comparison of these findings with the as-received samples showed neither a Cr-depletion zone nor a recrystallized zone, as was expected, since no thermal and oxidizing exposure had taken place. Exposure in air also resulted in a zone of

Table 2.2: Composition based on EDX spot scans, in sCO_2 and air exposed samples at 650 ℃; Compositions are presented in wt% and normalized; error is ± 1$wt\%$

Spectrum Label	C	Si	Ti	Cr	Mn	Fe	Ni
Matrix - sCO_2	3.35	0.29	0.47	19.58	0.82	43.21	31.74
Matrix - air	3.37	0.3	0.4	20.19	0.85	44.02	32.59
Recrystallized zone - sCO_2	5.42	0.21		8.35		48.86	37
Carbides precipitation zone - sCO_2 [1]	7.71		0.66	18.94		41.57	30.34
Carbides precipitation zone - air [2]	3.68	0.2	0.32	17.35		44.83	33.25
Grain boundary carbides - sCO_2 [3]	6.28	0.14	0.27	36.6	0.83	35.49	20.4

([1]Fig. 8.c; [2]Fig.7; [3]Fig. 8b)

recrystallized grains beneath the oxide scale, although the width of the recrystallized zone is significantly smaller than in the comparable exposure times for sCO_2, see Table 2.3. It should be noted, that the lack of continuous layer of new grains in Figure 2.9d for the 600 hrs air-exposed sample is representative for the entire sample. Therefore, the significant decrease in recrystallization needs to be taken into account.

Table 2.3: Comparison of scale and recrystallization zone widths between sCO_2 and air exposed samples.

	200 hrs air	600 hrs air	200 hrs sCO_2	600 hrs sCO_2
Scale [nm]	350 ± 80	460 ± 150	400 ± 60	420 ± 43
Recrystallized / Cr-depleted zone [nm]	550 ± 80	790 ± 170	800 ± 70	970 ± 130

Kernel average misorientation map (KAM) of the acquired patterns showed higher relative intensities for the region of the recrystallized grains than the interface region below the recrystallized zone in the sCO_2 sample than for the air-exposed samples. Within the group of sCO_2 samples, shown in Figure 2.10a, b, the misorientation maps indicate an accumulation of local strain in both the grain boundaries of the

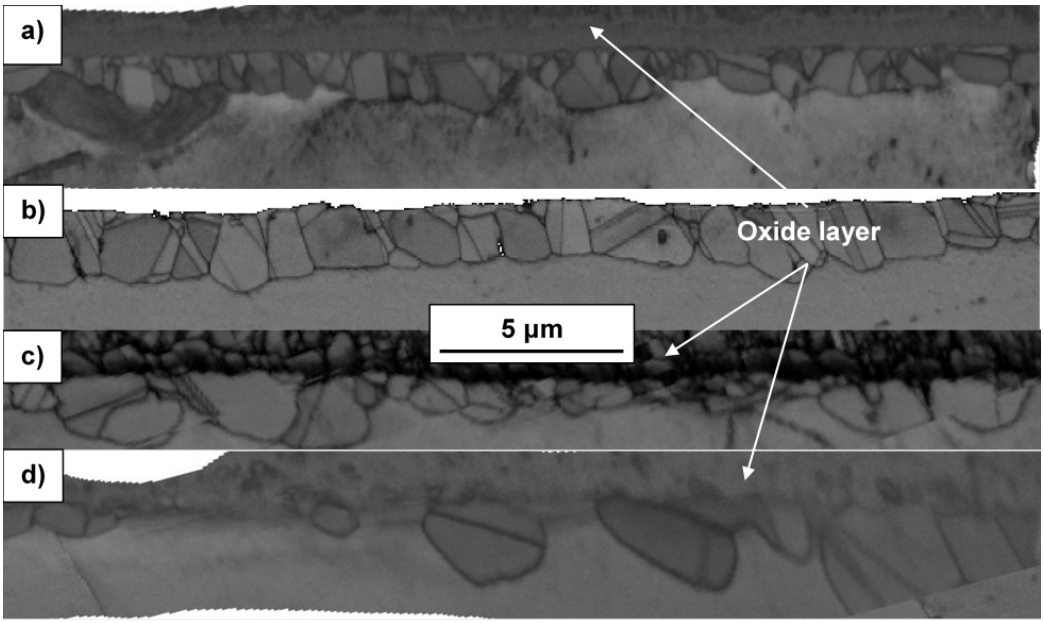

Figure 2.9: Comparison of EBSD image quality maps of surface cross-sections of 800H at 650 ℃ in a) sCO_2 - 200 hrs, b) sCO_2 - 600 hrs, c) air - 200 hrs and d) air - 600 hrs.

recrystallized zone and the adjacent interface region of the base-metal grain. When comparing both exposure times of the sCO_2 samples, the region beneath the RX zone shows a noticeable decrease in local strain with increase in time. The effect becomes more noticeable when considering the histogram of misorientation angles for both samples, see Figure 2.10c. It is readily visible that the distribution of strain changes from wider spread with a higher number density at relatively larger strain values to a narrower distribution at smaller misorientation angle at 600 hrs. The highest number density decreased from $\theta =$ 0.35 to 0.2, for 200 hrs and 600 hrs, respectively. The grain orientation spread function is commonly employed tool for estimating the fraction of recrystallized grains with EBSD patterns [14, 15] by measuring the angular deviations for all pixels within a grain from the grain mean orientation and then

plotting the average of the deviations for each grain. For the sCO_2 exposed samples, a histogram showing the grain orientation spread can be seen in Figure 2.10d. For both exposure times, the spread is similar and extends to relatively large angles beyond 30° and appears rather randomly distributed, despite the low number of occurrences per bin. Due to the lower number of recrystallized grains detected for the air-exposed samples, no statistically relevant information could be extracted to gain detailed assessment of their recrystallization behavior.

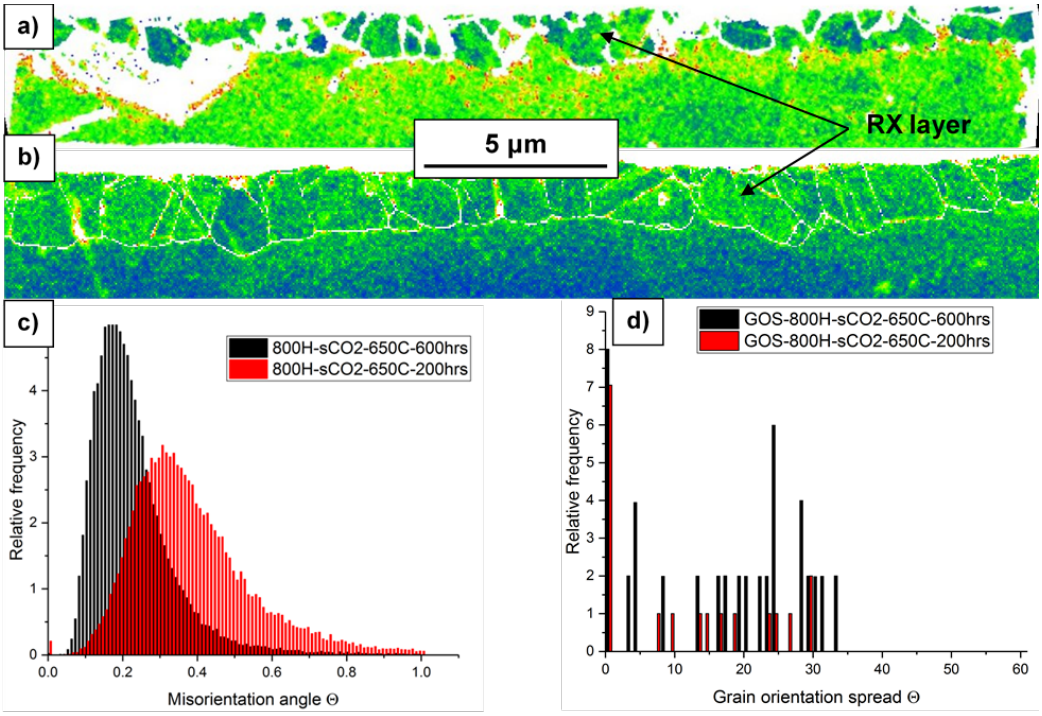

Figure 2.10: EBSD KAM maps of 800H exposed at 650 ℃ in sCO_2 at a) 200 hrs and b) 600 hrs, using 3x3 filter, max. misorientation of 1°, c) histogram of misorientation of angles and d) the grain orientation spread.

2.4 Discussion

When comparing the results from the XRD measurements with the surface SEM images, a noticeable trend with increasing sCO_2 exposure time is the decrease in peak intensity for Cr_2O_3. However, more pronounced peaks could be confirmed for Fe_2O_3 and Fe_3O_4 in the XRD results in Figure 2.2, which indicated another growing oxide layer, which has faster growth kinetics at these temperatures. In particular, the order of appearance of both Fe-oxide phases, first Fe_3O_4 then Fe_2O_3, as time progressed, is in congruence with expected kinetics and has been shown previously [16, 17]. SEM images of the sample surface oxides in Figure 2.4 show nodules and rapidly grown areas of Fe-oxides, but neither the qualitative oxide volume increase assumed from these SEM results nor the weight change results indicated an increase in the mass change over time, when the Fe-oxides became more pronounced. It is possible that some of these Fe-oxides have dissolved or became separated from the material during the exposure, leading to a lower total net weight and reduced weight gain. The cross-sectional microanalysis also confirms the earlier finding of an outermost Fe-oxide-rich scale, that transitions to a mixed Fe-Cr-Ni spinel-oxide and Cr-oxide, closer to the base-metal. Both these findings and the Cr-depletion zone are in general agreement with studies on sCO_2 exposure of 800H and similar Fe-base alloys rich in Ni and Cr [18–20]. The occurrence of internal oxidation of aluminum can be explained by grain boundaries being paths of faster diffusion. These would allow oxygen to travel farther into the base-metal, while aluminum from within the matrix diffuses rapidly to form oxides at these locations [21].

The occurrence of a recrystallized zone in the sCO_2 samples was considered noteworthy as it has not been described earlier in alloy 800H [10, 19, 20], however it was recently observed in another Ni alloy exposed to high temperature sCO_2 [22]. Comparison with the reference sample exposed in argon suggested that the mechanical damage introduced by grinding and polishing was not the primary reason for formation of the recrystallized zone. TThe air exposure also resulted in a recrystallized zone, suggesting that oxidation and/or the scale formation associated with it, is a driving factor of recrystallized zone formation, this has been shown by a recent study [**?**]. While the recrystallized zone in the air-exposed samples was thinner and less dense than for sCO_2, its existence has also been reported elsewhere for other similarly alloyed materials [23–25]. Besides the more continuous layers of recrystallized zone for the sCO_2 exposed samples, the existence of localized strain fields within and beneath this zone could also contribute to the growth.

Reasons for the existence of this layer were discussed. Localized strain fields may induce recrystallization, and such strain fields can be exerted by growing oxide scales [24, 26]. It is known that epitaxial growth stress from growing scales and their adhesion to the underlying base-metal can lead to tensile stress [27]. It is plausible that dislocations are generated to accommodate these stresses, which may create locally different dislocation densities, thus allowing nucleation of recrystallized grains. Another possible explanation for the presence of the recrystallized zone is the migration of vacancies and diffusion of Cr atoms, leading to kinetic and thermodynamic instabilities that allow for recrystallization to occur. Cr diffusion is assumed to take place as a result of Cr depletion, and, combined with its faster diffusion in the matrix than

Ni, a net flux of vacancies towards the metal/oxide interface results. The contraction of the lattice locally, may leave the matrix in a state of stress, as well as generate dislocations to accommodate these. This effect could be another possible source for the onset of recrystallization. Accumulation of vacancies at this interface may lead then to formation of voids. Oleksak et al. have showed the presence of such after exposure to sCO_2, for short incubation times (Oleksak, Carney, Holcomb, Doan, In press). While Oleksak did no report presence of recrystallization at these early times, Al_2O_3 was found at the metal/oxide interface, similar to the findings of Al_2O_3 at the metal/oxides interfaces, analyzed in this study. It is possible then, that Al_2O_3 and voids at the interface may serve as nucleation sites for the onset of recrystallization, upon continued exposure.

The increased grain boundary density, caused by the recrystallized zone, could result in a higher volume fraction of faster diffusion pathways. These can be especially important for the transport of carbon or oxygen species deeper into the matrix. Nguyen et al. also commented on the potential effect of higher grain boundary density, which allows for oxygen, or other species, diffusion along the grain boundaries [28–30]. Internal carburization was evident by the internal carbides found in the sCO_2 exposed samples, which were less pronounced after exposure to air. The increase in the amount of carbides with increase in time, for sCO_2 but not air exposure, suggests a continuous supply of carbon to form the carbide phases. Thus, it seemed that the effect of a larger recrystallized zone in the sCO_2 samples further aided the carburizing potential of free carbon atoms, which are present at the oxide surface, by providing fast transport paths.

2.5 Conclusions

Corrosion studies of alloy 800H have been carried out in sCO_2, air and argon a 650 ℃ and 750 ℃ for up to 1000 h at 20 MPa, and the alloys characterized with electron microscopy, x-ray diffraction and weight change measurements. Comparison between the oxide scales based on sCO_2 and air exposure showed no significant difference in scale thickness. It appears though that sCO_2 has a more pronounced influence on the underlying base-metal microstructure, especially in terms of internal carburization and presence of a recrystallized zone. This zone was widest after sCO_2 exposure, and since it was collocated with the chromium depletion zone beneath the scale, the sCO_2 exposed samples also showed the widest depletion zone. The cause for existence of the recrystallized zone was discussed. While it was not ruled out that mechanical damage from sample preparation may play a role, the formation of the oxide scale and the stress associated with it was believed to be the main contributor. Finally, the higher density of grain-boundaries, serving as fast-diffusion pathways, could explain the internal carburization present in all oxidized samples. The higher amount found in the sCO_2-exposed than in the air-exposed samples might then be related to the higher availability of monatomic carbon at the oxide-gas interface.

2.6 Bibliography

[1] Y. Ahn, S. J. Bae, M. Kim, S. K. Cho, S. Baik, J. I. Lee, and J. E. Cha, "Review of supercritical CO2 power cycle technology and current status of research and development," *Nuclear Engineering and Technology*, vol. 47, no. 6, pp. 647–661, 2015. [Online]. Available: http://linkinghub.elsevier.com/retrieve/pii/S1738573315001606 2.1

[2] A. Kruizenga, H. Li, M. Anderson, and M. Corradini, "Supercritical Carbon Dioxide Heat Transfer in Horizontal Semicircular Channels," *Journal of Heat Transfer*, vol. 134, no. 8, p. 081802, 2012. 2.1

[3] G. R. Holcomb, C. Carney, J. A. Hawk, Ö. N. Doan, K. Rozman, and M. H. Anderson, "Materials Performance in Supercritical CO2 in Comparison with Atmospheric Pressure CO2 and Supercritical Steam," *The 5th International Symposium - Supercritical CO2 Power Cycles*, 2016. 2.1

[4] B. Pint, R. Brese, and J. Keiser, "Effect of pressure on supercritical CO 2 compatibility of structural alloys at 750 C," *Materials and Corrosion*, vol. 68, no. 2, pp. 151–158, feb 2017. [Online]. Available: http://doi.wiley.com/10.1002/maco.201508783 2.1

[5] V. Firouzdor, K. Sridharan, G. Cao, M. Anderson, and T. R. Allen, "Corrosion of a stainless steel and nickel-based alloys in high temperature supercritical carbon dioxide environment," *Corrosion Science*, vol. 69, pp. 281–291, 2013. [Online]. Available: http://dx.doi.org/10.1016/j.corsci.2012.11.041 2.1

[6] R. P. Oleksak, J. P. Baltrus, J. Nakano, A. Nakano, G. R. Holcomb, and Ö. N. Doan, "Mechanistic insights into the oxidation behavior of Ni alloys in high-temperature CO 2," *Corrosion Science*, no. June, 2017. [Online]. Available: http://linkinghub.elsevier.com/retrieve/pii/S0010938X16308393 2.1

[7] G. R. Holcomb, J. Tylczak, C. Carney, and Ö. N. Doan, "High Materials Performance in Supercritical CO 2 in Comparison with Atmospheric Pressure CO 2 and Supercritical Steam Acknowledgement & Disclaimer," 2017.

[8] J. Mahaffey, D. Adam, A. Brittan, M. Anderson, and K. Sridharan, "Corrosion of Alloy Haynes 230 in High Temperature Supercritical Carbon Dioxide with Oxygen Impurity Additions," *Oxidation of Metals*, vol. 86, no. 5-6, pp. 567–580, 2016.

[9] J. Shingledecker, R. Purgert, and P. Rawls, "Current Status of the U.S. Doe/CDO A-USC Materials Technology Research and Development Program," in *7th International Conference on Advances in Materials Technology for Fossil Power Plants*, 2013, pp. 41–52.

[10] H. J. Lee, H. Kim, S. H. Kim, and C. Jang, "Corrosion and carburization behavior of chromia-forming heat resistant alloys in a high-temperature supercritical-carbon dioxide environment," *Corrosion Science*, vol. 99, pp. 227–239, 2015. [Online]. Available: http://dx.doi.org/10.1016/j.corsci.2015.07.007 2.1, 2.4

[11] Special Metals, "INCOLOY alloy 800H & 800HT," Tech. Rep., 2004. (document), 2.1, 2.1

[12] W. Ren and R. Swindeman, "Status of Alloy 800H in Considerations for the Gen IV Nuclear Energy Systems," *Journal of Pressure Vessel Technology*, vol. 136, no. 5, p. 054001, 2014. 2.1

[13] J. Dong, Z. Bi, N. Wang, X. Xie, and Z. Wang, "Structure Control of a New-Type High-Cr Superalloy," *Superalloys 2008 (Eleventh International Symposium)*, pp. 41–50, 2008. 2.3

[14] F. J. Humphreys, "Grain and subgrain characterisation by electron backscatter diffraction," *Journal of Materials Science*, vol. 36, no. 16, pp. 3833–3854, 2001. 2.3

[15] S. I. Wright, M. M. Nowell, and D. P. Field, "A review of strain analysis using electron backscatter diffraction." pp. 316–329, 2011. 2.3

[16] N. Birks, G. H. Meier, and F. S. Pettit, *Introduction to the High Temperature Oxidation of Metals*, 2006. [Online]. Available: http://www.cambridge.org/gb/knowledge/isbn/item1110694/?site{_}locale=en{_}GB 2.4

[17] R. Kane, "High-Temperature Gaseous Corrosion," in *ASM Handbook, Vol 13A, Corrosion: Fundamentals, Testing, and Protection,*. Materials Park, OH: ASM International, 2003, p. 577. 2.4

[18] L. Tan, T. R. Allen, and Y. Yang, "Corrosion behavior of alloy 800H (Fe-21Cr-32Ni) in supercritical water," *Corrosion Science*, vol. 53, no. 2, pp. 703–711, 2011. [Online]. Available: http://dx.doi.org/10.1016/j.corsci.2010.10.021 2.4

[19] L. Tan, M. Anderson, D. Taylor, and T. R. Allen, "Corrosion of austenitic and ferritic-martensitic steels exposed to supercritical carbon dioxide," *Corrosion Science*, vol. 53, no. 10, pp. 3273–3280, 2011. 2.4

[20] F. Rouillard, F. Charton, and G. Moine, "Corrosion behaviour of different metallic materials in supercritical CO2 at 550C and 250 bars," *SCCO2 Power Cycle Symposium 2009*, vol. 67, no. 9, pp. 1–27, 2009. [Online]. Available: http://www.onepetro.org/mslib/servlet/onepetropreview?id=NACE-10195{&}soc=NACE{&}speAppNameCookie=ONEPETRO 2.4

[21] E. A. Polman, T. Fransen, and P. J. Gellings, "Oxidation kinetics of chromium and morphological phenomena," *Oxidation of Metals*, vol. 32, no. 5/6, pp. 433–447, 1989. 2.4

[22] R. P. Oleksak, C. Carney, G. R. Holcomb, and Ö. N. Doan, "Structural Evolution of a Ni Alloy Surface During High-Temperature Oxidation," *Oxidation of Metals*, 2017. 2.4

[23] S. Cissé, L. Laffont, B. Tanguy, M. C. Lafont, and E. Andrieu, "Effect of surface preparation on the corrosion of austenitic stainless steel 304L in high temperature steam and simulated PWR primary water," *Corrosion Science*, vol. 56, pp. 209–216, 2012. 2.4

[24] S. Bruemmer, M. Olszta, M. Toloczko, and L. Thomas, "Linking Grain Boundary Microstructure to Stress Corrosion Cracking of Cold-Rolled Alloy 690 in Pressurized Water Reactor Primary Water," *CORROSION*, vol. 69, no. 10, pp. 953–963, oct 2013. [Online]. Available: http://corrosionjournal.org/doi/10.5006/0808 2.4

[25] W. Li, X. Huang, J. Li, O. T. Woo, R. Sanchez, and C. D. Bibby, "Effect of Pressures on the Corrosion Behaviours of Materials at 625C," *Jom*, vol. 69, no. 2, pp. 207–216, 2017. 2.4

[26] S. Cruchley, M. P. Taylor, H. E. Evans, P. Bowen, M. . Hardy, and S. Stekovic, "Microstructural Characterisation of High Temperature Oxidation of Nickel Base Superalloy Rriooo and the Effect of Shot-Peening," *Superalloys 2012 : 12th international Symposium on superalloys*, pp. 751–758, 2012. 2.4

[27] G. Wood, J. Stringer, and H. Id, "The adhesion of growing oxide scales to the substrate," *Journal de Physique IV Colloque*, vol. 3, no. C9, 1993. [Online]. Available: https://hal.archives-ouvertes.fr/jpa-00252334 2.4

[28] T. Nguyen, J. Zhang, and D. Young, "Effect of Mn on corrosion of Fe-Cr and Fe-Cr-Ni alloys in dry CO<inf>2</inf> at 650 C," *Australasian Corrosion Association Annual Conference: Corrosion and Prevention 2015, ACA 2015*, vol. 112, pp. 110–127, 2015. 2.4

[29] L. Tan, X. Ren, K. Sridharan, and T. R. Allen, "Effect of shot-peening on the oxidation of alloy 800H exposed to supercritical water and cyclic oxidation," *Corrosion Science*, vol. 50, no. 7, pp. 2040–2046, 2008.

[30] S. Sarrade, D. Féron, F. Rouillard, S. Perrin, R. Robin, J. C. Ruiz, and H. A. Turc, "Overview on corrosion in supercritical fluids," *Journal of Supercritical Fluids*, vol. 120, pp. 335–344, 2017. [Online]. Available: http://dx.doi.org/10.1016/j.supflu.2016.07.022 2.4

Chapter 3: Characterization of Ni-based alloys IN625 and HR120 at 550 ℃ in sCO_2

3.1 Introduction

Growing interest in supercritical carbon dioxide (sCO_2) cycles is driving the need for corrosion data on candidate plant materials. The sCO_2 Brayton cycle [1, 2] is being considered for power conversion systems including solar, fossil and nuclear heat sources. Multiple organizations have developed test facilities to address the knowledge gap in corrosion data in high temperature, high pressure sCO_2 environments [3–6]. In the past, there has been no formal test program among multiple organizations to validate the consistency of data or to make use of the different facilities to develop a consistent collaborative data generation plan. The goal of this recent collaboration effort is the provision of essential information for the development of the sCO_2 power cycle by presenting comparable and reproducible results. The round robin team selected five different alloys, based on criteria such as existing research and characterization, unit price based on alloying composition, and the applicable mechanical and corrosion properties. These alloys are two Ni- and Fe-Ni-based superalloys, Inconel IN625 and Haynes HR120, one austenitic stainless steel, SS316L, and one heat-resistant alloy steel, Gr91.

This work presents preliminary microstructural results from a first cycle of expo-

sure testing, at 550 ℃ and up to 1000 h, in comparison with results from samples in as-received condition, performed at Oregon State University. Optical and electron micrographs for the microstructures of alloys Gr91 and SS316L are presented elsewhere and are not included in this work [7].

3.2 Methodology

The as-received (AR) chemical compositions of the selected alloys are provided in Table 3.1. Samples were sectioned and machined from initial plate material, into 16 mm^2 coupons, with thickness between 1.1 and 3.2 mm. Additionally, a 4mm hole was drilled in one corner of the coupons, allowing them to be hung in the autoclave. As-received samples were polished to a 600 grit surface finish, before exposure. An extra sample of each alloy was prepared for as-received characterization to serve as a baseline of comparison for the exposed coupons.

Table 3.1: Chemical composition of studied alloys, in wt-%

Alloy	Fe	Cr	Ni	Co	Al	Mn	Mo
Gr91	89.27	8.23	0.13	0.018	0.01	0.45	0.93
SS316L	68.29	16.84	9.93	0.214	0.002	1.58	1.98
HR120	34.48	24.94	37.44	0.248	0.069	0.8	0.47
IN625	3.66	21.17	61.65	0.178	0.204	0.28	8.7

Alloy	Nb	Cu	Ti	Si	V	W
Gr91	0.063	0.091	0.003	0.279	0.196	0.141
SS316L	0.009	0.492	0.01	0.36	0.079	0.065
HR120	0.561	0.065	0.015	0.483	0.036	0.078
IN625	3.422	0.159	0.21	0.168	0.002	0.111

All samples were tested at 20 MPa in a target environment of 99.999% pure CO_2

(research grade) at a temperature of 550 ℃. The CO_2 flow rates were set to refresh the test chamber at a minimum of every two hours. Six specimens of each alloy were initially loaded into the autoclave. Samples were then exposed for a total of 1000 h in 500 h increments. After each increment, all samples were removed for mass change measurements, at least one sample from each alloy was kept for additional characterization and the remainder were returned to an autoclave for additional exposure. All samples were weighed and dimensioned prior to any sCO_2 exposure. After each exposure increment, samples were weighed again to detect changes in mass due to corrosion product growth or spallation. One sample was kept for further characterization after each exposure. Other samples were returned to the autoclave for additional exposure. Sample surfaces were characterized by x-ray diffraction (XRD) for phase identification of corrosion products and scanning electron microscopy (SEM) were used to identify pitting or spallation of the corrosion layer. After surface characterization, samples were sputter-coated with gold to provide an electrically conductive surface for subsequent electrodeposition with copper. This was intended to protect the oxide scale in its original condition during the mounting, grinding and polishing steps. Afterwards, all samples were prepared according to standard metallographic preparation techniques, to a final surface finish of 0.04 μm with colloidal silica. Cross-sections were examined for the thickness and chemical composition of the corrosion layer via Transmission Electron Microscopy (TEM) and energy dispersive spectroscopy (EDS). For TEM analysis, the respective samples were extracted from the coupons using standard FIB-liftouts techniques, and welded onto Omnigrid sample holders. Analysis and imaging was done with a FEI Tecnai F20 at 200 kV, using both bright-field

and scanning-TEM techniques. The grain size on as-received and exposed samples was determined using Electron Backscatter Diffraction (EBSD) technique, on polished cross-sections. The acquisition was done with a Zeiss Sigma FEG-SEM and an Oxford Instruments EBSD detector at 15 kV. The mass change of each sample and the oxide thickness for one representative sample per alloy were recorded after each exposure.

3.3 Results and Discussion

The AR samples have been characterized by XRD in Bragg-Brentano condition, and EBSD for grain size analysis and microstructural assessment. The XRD results are presented in Figure 3.1. All austenitic alloys, IN625, SS316L and HR120, show peaks corresponding with austenite peak angles and ratios. However, the IN625 alloy has a slight deviation in location and increased intensity relative to the other austenitic alloys, but aligns best with the standard peaks for austenite. This is likely due to the increased Ni levels, maximizing the austenite stability and approximating the lattice parameter for pure austenite, i.e., pure Ni for example. The ferritic alloy, Gr91, shows good agreement with the standard peaks for α-ferrite, as expected for its mainly ferritic matrix.

EBSD allowed for capturing a large number of grains, and thus can provide grain size analysis with high statistical significance. All maps are presented as inverse pole figure (IPF) maps along the x-axis, which is defined to be the rolling direction. Since the change in microstructure of the individual base metals are of primary concern for

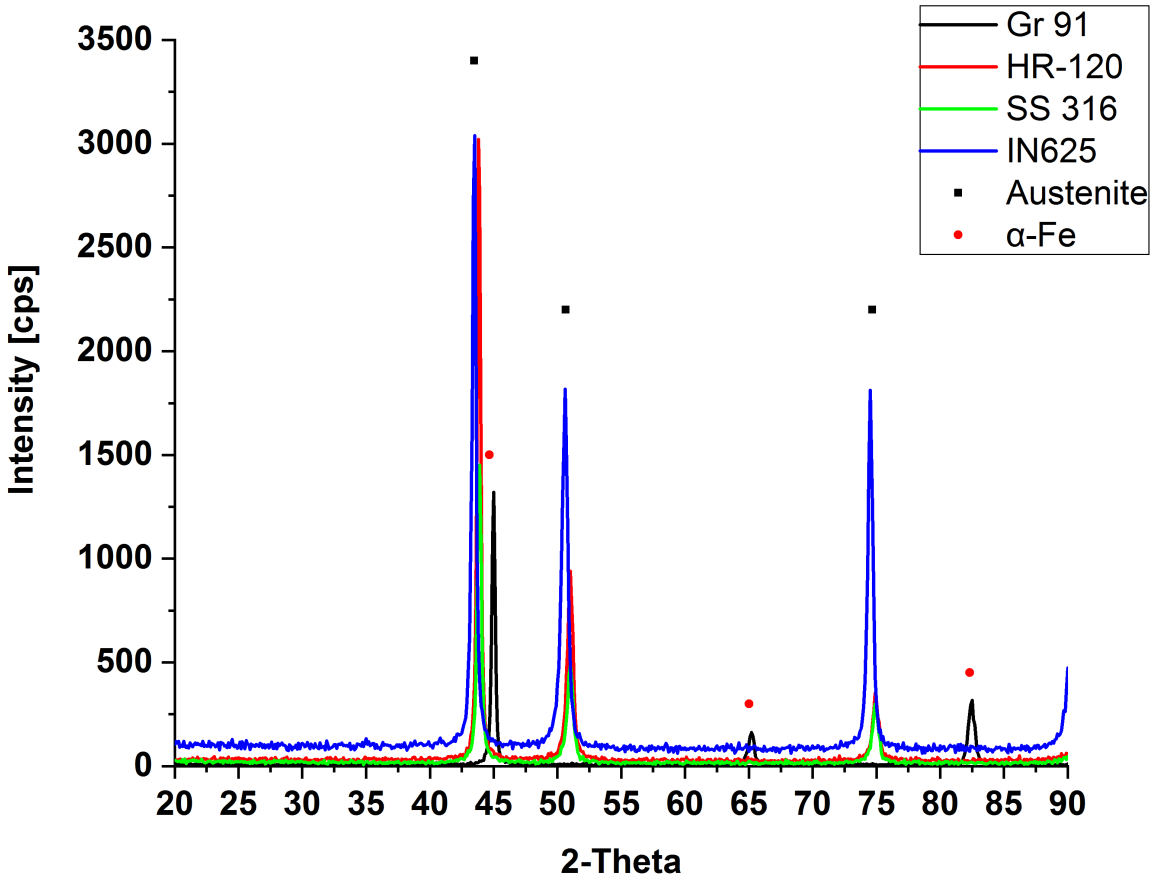

Figure 3.1: Wide angle X-ray spectra for all five test alloys in the as received condition, superimposed with peak markers for γ-austenite and α-ferrite, at a step size of 0.1 ° and dwell time 0.1s

subsequent exposure tests, grain size analysis of the cross sections of the AR samples was performed to establish a reference point. The results are then compared with the equivalent findings from the exposed samples.

Figure 3.2 shows the microstructures before and after exposure testing for all alloys. The AR materials show that alloy Gr91 has a much finer microstructure and was thus imaged at a higher magnification in order to adequately showcase the

grain structure. The matrix showed a mostly acicular ferrite grain structure, with an average grain size of 2 μm. All other alloys had a solely austenitic, uniform and equiaxed matrix, with varying average grain sizes, owing to the different standard heat-treatments. Statistical data for the grain size analysis is presented in Table 3.2 for both AR and exposed conditions.

In comparison, there is relatively little change in the average grain size, i.e., grain coarsening did not significantly occur. Effects of recrystallization can generally be ruled out, as the temperatures required for recrystallization are well beyond the testing temperature of 550 ℃. However, for alloy Gr91, the testing temperature was within the range of recrystallization for general steels. It should be noted, that while the average grain size for HR120 showed a decrease after exposure, the difference fell well within the reported standard deviation, which itself remained constant in comparison with the as-received case.

Table 3.2: Grain size analysis statistics for as-received and sCO_2-exposed samples

Alloy	Gr91	HR120	SS316L	IN625
As-received, avg. [μm]	2.00	44.19	11.72	9.54
SD [μm]	1.23	29.83	6.67	5.52
sCO_2-1000 h-550 ℃, avg. [μm]	2.15	39.57	11.46	8.39
SD [μm]	1.20	27.67	6.77	5.28

Cross-sectional analyis using TEM was performed on alloys HR120 and IN625, as both exhibited oxide-scale microstructures, that were below the resolution of both optical and scanning electron microscopes. It should be noted, that for the EDS linescan plots, the Ni-signal was removed from the plot to allow for better resolution

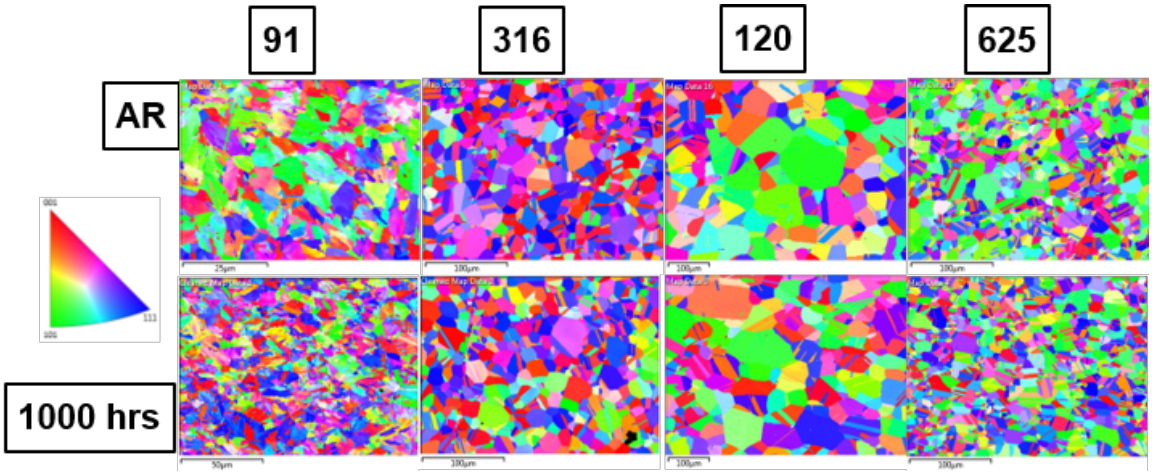

Figure 3.2: Comparison of base-metal microstructures using EBSD IPF-X maps, for grain size analysis of AR and samples exposed in sCO_2 for 1000 h and 550 ℃.

of the other elements.

For IN625, the general material surface is presented in Figure 3.3, showing a cross-section of an as-exposed sample. Locations of EDX linescan that was performed is indicated as well as the boundaries of the identified microstructurally distinguishable zones. The material shows a continuous and uniformly thick oxide scale, with an average thickness of approximately 250 nm. According to the result from the EDX-linescan, which traversed across the surface of the oxide to the base-metal, the oxide film appears to be a Cr-oxide, with fluctuations in Cr content. The data shows, that in Cr-deficient areas, the former Cr sites are replaced with Si atoms, thus leading to the formation of either a duplex layer of chromia and silica or a spinel phase with $(Cr,Si)_3O_4$. It is known that silicon enhances the formation of a Cr_2O_3-layer by increasing the diffusion coefficient of chromium, and at the same time forms the much more thermodynamically stable silica oxide, which is usually found underneath

[8, 9]. Scales formed in sCO_2 tend to exhibit an inward growth characteristic, thus the outermost part of the scale, if mechanically unharmed, presents the first oxidation event [10].

Thus, it is assumed, that initially formed silica particles may either have formed only unconnected oxide particles or an imperfect, permeable scale. In either case oxygen may have then diffused past the silica into the base-metal and allowed chromium to be oxidized. The reported base-metal values for silicon were low, 0.17 wt-%, thus it is not surprising to see even lower values in the scale-surrounding matrix. It is further known, that the diffusion coefficient of silicon in nickel is considerably lower than that of chromium in nickel [11]. Therefore, after long exposure times, when the scale growth is in its steady-state of the parabolic growth curve [12], some silica is formed, again beneath the scale, as seen in Figure 3.4.

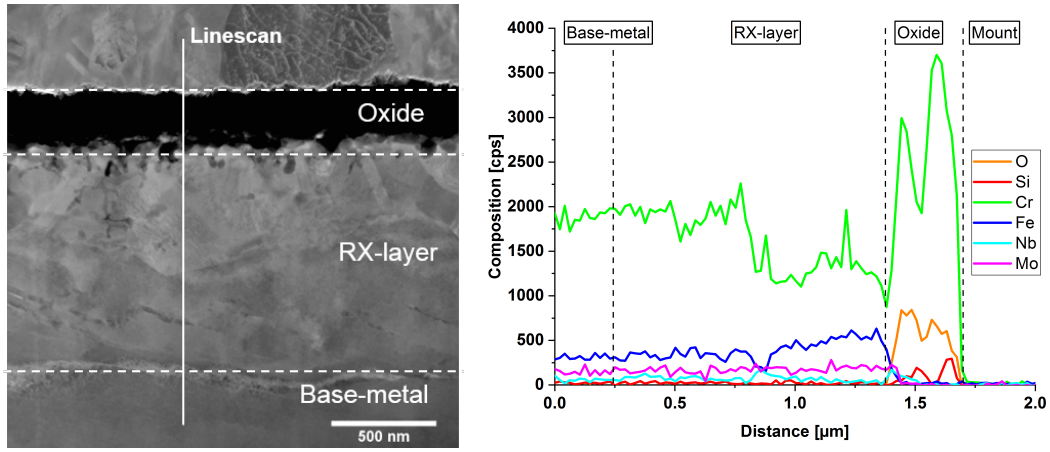

(a) (b)

Figure 3.3: a) Scanning TEM cross-section view of IN625 after exposure for 1000 h at 550 ℃ in sCO_2 with b) results of the indicated EDX-linescan.

Below the scale a zone of reduced Cr content, relative to the AR matrix composition, was found. This zone extended for approximately 0.5 μm into the material. This Cr-depletion zone was associated with the preferential and selected oxidation of Cr and the resulting kinetic equilibrium between Cr-cations entering the oxide and Cr from the surrounding matrix diffusing back. Of interest is the appearance of a zone of recrystallized grains, which partially overlaps with the Cr-depletion zone, but extends further into the base-metal, to a total depth of approximately 1 μm, see Figure 3.3. It was suggested that the presence of the RX-zone is linked to the locally lower Cr-content, i.e. chemically induced decrease in activation energy and critical temperature for the onset of recrystallization.

In Figure 3.4 the presence of internal oxidation beneath the oxide scale is shown. The darker spots in the matrix were positively identified as Cr_2O_3 grains. Other apparent spots were investigated as well for their composition, EDX spot scane 3 to 6 in Figure 3.4. However, apart from the higher Cr level, it was apparent that their composition is largely the same as the surrounding matrix and the average base-metal composition. It should be noted that spectra 3 and 6 also showed very low levels of Al and O.

Carbon levels in the RX-zone and scale regions were analyzed for any elevated values. While there are some reported cases for Ni-based systems, they are mostly related to Fe-Ni-based systems, where the presence of Fe allows for increased mobility, see studies by Lee et al. [13–15].

The cross-sectional overview of the scale and the underlying matrix for alloy HR120 is presented in Figure 3.5. The oxide scale thickness after the 1000 h ex-

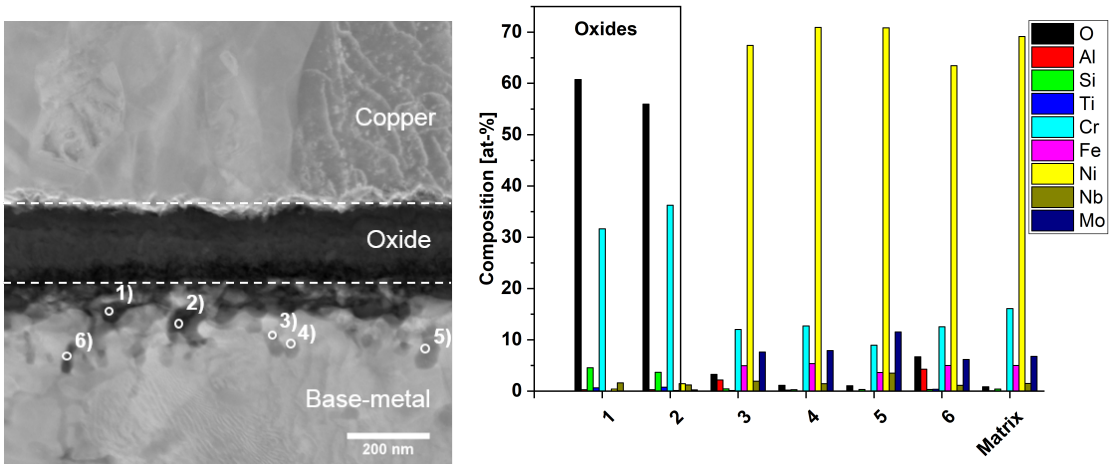

(a) (b)

Figure 3.4: a) STEM image of IN625 after exposure for 1000 h at 550 ℃ in sCO_2 showing oxide scale and internal oxidation, with b) results of indicated EDX-spot scans.

posure at 550 ℃ in sCO_2 showed a uniform scale, similar to IN625, with comparable average thickness of 200 nm. Also, the presence of a subsurface RX layer was confirmed, which showed a comparable width of 1.1 μm. However, unlike IN625, HR120 exhibited an additional layer beneath the oxide scale, termed sub-layer, which was uniform in appearance and width, at approximately 120 nm. Interestingly, this layer was not part of the oxide film, as it showed no oxygen presence, but showed a similar chemical makeup as the underlying base-metal, that is, a strong Cr-depletion and Fe/Ni-enrichment. The sub-layer was bordered on both interfaces by a thin, continuous layer of SiO_2, indicated by arrows in the EDS-linescan. It was assumed that existence of the innermost silica layer can be attributed to two effects. Firstly, the very low local Cr-activity, limiting any formation of Cr-oxides within the layer, and secondly, the high affinity of Si for the oxygen, which diffused though the oxide scale

into the base-metal. Therefore, even though silica shows much slower formation kinetics than chromia, in absence of available chromium, silicon has sufficient time to form such a continuous layer [16]. It is assumed that both silica layers are effectively limiting the diffusion of both chromium and oxygen species to and from the sub-layer, preserving its current state. Longer exposure times will show the further evolution of this layer. The oxide scale does shows a presence of silicon, similar to IN625, where the assumption is also that the topmost layer of the oxide represents an early stage of the oxidation process.

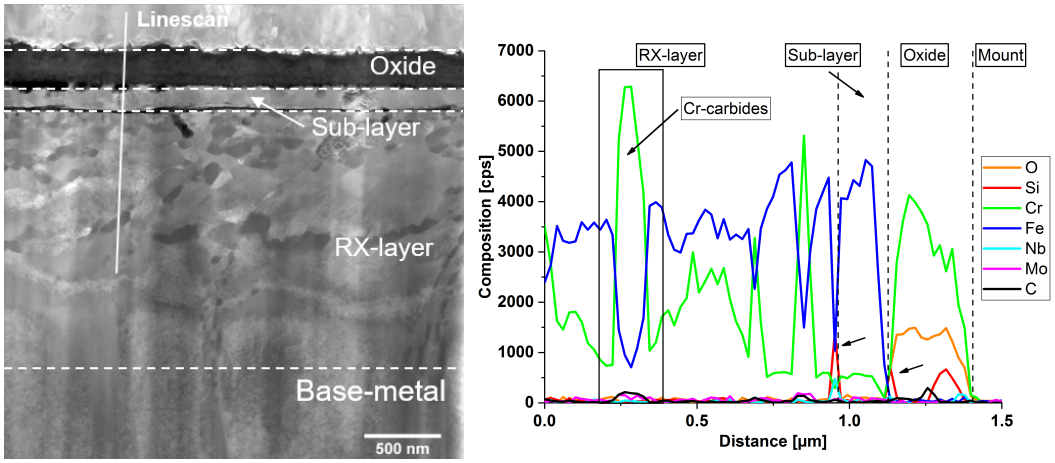

(a) (b)

Figure 3.5: a) STEM image of HR120 after exposure for 1000 h at 550 ℃ in sCO_2 showing overview of oxide scale and underlying matrix, with b) results of indicated EDX-linescan.

Internal carbides were positively identified in HR120, as seen in the EDX-linescan result in Figure 3.5, in contrast to IN625. The only other element that showed an increase in intensity was chromium, which suggested the presence of Cr-carbides,

likely the $Cr_{23}C_6$-type, being the most stable carbide phase. While the linescan clearly showed the presence, the size distribution was not directly clear from the STEM image, by contrast. Therefore, EDX mapping of the entire subsurface area was performed, seen in Figure 3.6. The maps show again clearly the presence of Cr-rich carbide phases underneath the scale and sub-layer, while no presence of internal oxides was found at all. Further, Cr-depletion zones were also visible around the carbides, where in turn Fe and Ni replaced its sites. The strong presence of carbides near the surface suggests internal carburization, stemming from CO_2 ingress through scale and dissocation at the oxide/metal-interface [17]. It has been shown that internal carburization during sCO_2-exposure is more pronounced in alloys with higher Fe/Ni-ratios [13], such as Fe-Ni-based alloys. In such alloys, an increased solubility and diffusivity for chromium and carbon is found [13, 18]. Further, iron shows a higher solubility in the $M_{23}C_6$-type carbide than nickel does.

3.4 Conclusion

The effects of sCO_2-exposure on the microstructural evolution of the ferritic steel Gr91, the stainless 316L and two Ni-based superalloys IN625 and HR120 have been studied. An EBSD comparison between the as-received condition and after sCO_2 exposure for 500 hrs at 550 ℃ showed that the bulk microstructure was unaffected. It was suggested that this was due to the thermal stability of the alloys and their high respective recrystallization temperature. Both the surface and oxide interface microstuctures of the Ni-based superalloys were examined using TEM and EDS. Both

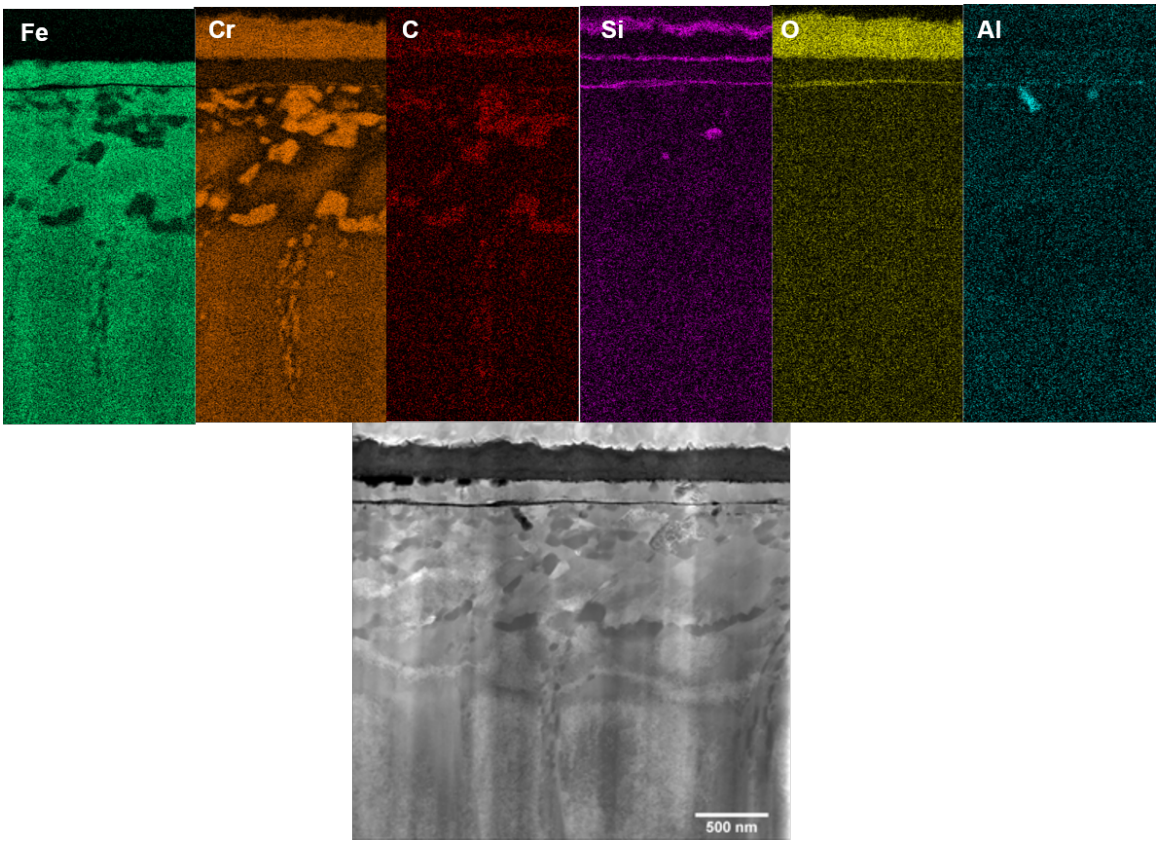

Figure 3.6: STEM-EDX elemental maps for HR120 after exposure for 1000 h at 550 ℃ in sCO_2 showing the presence of Cr-carbides in the base-metal.

showed a comparable, uniform scale of 200-250 nm thickness, primarily consisting of chromia. Presence of silica was also found in both layers towards the gas/oxide interface, assumed to be early stage of oxidation, following chromia inward growth. While the silicon content in IN625 was too low to also form a continuous silica layer at the scale/metal interface, HR120 exhibited such a layer as the base-metal composition had roughly three times as much silicon as IN625. Further, HR120 showed a layer of chromium-depleted base-metal beneath the oxide that was separated from the base-

metal by another layer of silica. It was assumed that the top oxide layers still allowed for a limited oxygen permeability to the base-metal, through the sub-layer, due to its low chromium presence. There was no internal oxidation in the HR120 alloy, in constrast to IN625, which showed some internal oxide precipitates beneath the scale. However, the presence of internal carburization was found in HR120. This suggests higher affinity of high Fe-containing alloys for carbide formation in comparison with Ni-based alloys with negligible Fe-content.

3.5 Bibliography

[1] Y. Kato, T. Nitawaki, and Y. Muto, "Medium temperature carbon dioxide gas turbine reactor," *Nuclear Engineering and Design*, vol. 230, no. 1-3, pp. 195–207, 2004. 3.1

[2] C. Oh, T. Lillo, W. Windes, T. Totemeier, and R. Moore, "Development of a supercritical carbon dioxide Brayton cycle: improving PBR efficiency and testing material compatibility," INL, Tech. Rep., 2006. 3.1

[3] V. Firouzdor, K. Sridharan, G. Cao, M. Anderson, and T. R. Allen, "Corrosion of a stainless steel and nickel-based alloys in high temperature supercritical carbon dioxide environment," *Corrosion Science*, vol. 69, pp. 281–291, 2013. [Online]. Available: http://dx.doi.org/10.1016/j.corsci.2012.11.041 3.1

[4] J. P. Gibbs, "Corrosion of Various Engineering Alloys in Supercritical Carbon Dioxide," Ph.D. dissertation, MASSACHUSETTS INSTITUTE OF TECHNOLOGY, 2010.

[5] F. Rouillard, F. Charton, and G. Moine, "Corrosion behaviour of different metallic materials in supercritical CO2 at 550C and 250 bars," *SCCO2 Power Cycle Symposium 2009*, vol. 67, no. 9, pp. 1–27, 2009. [Online]. Available: http://www.onepetro.org/mslib/servlet/onepetropreview?id=NACE-10195{&}soc=NACE{&}speAppNameCookie=ONEPETRO

[6] H. J. Lee, H. Kim, and C. Jang, "Compatibility of Candidate Structural Materials in High-Temperature S-CO2 Environment," *The 4th International Symposium - Supercritical CO2 Power Cycles*, pp. 1–9, 2014. 3.1

[7] J. D. Tucker, B. Adam, M. Anderson, G. R. Holcomb, H. Saari, L. Teeter, J. Mahaffey, Ö. Doan, C. Jang, and S. Kung, "Supercritical CO2 Round Robin Test Program," in *The 6th International Supercritical CO2 Power Cycles Symposium*. Pittsburgh, PA: SWRI, San Antonio, TX, 2018. [Online]. Available: http://sco2symposium.com/www2/sco2/papers2018/materials/146{_}Paper.pdf 3.1

[8] B. Li and B. Gleeson, "Effects of silicon on the oxidation behavior of Ni-base chromia-forming alloys," *Oxidation of Metals*, vol. 65, no. 1-2, pp. 101–122, 2006. 3.3

[9] B. Ahmad and P. Fox, "STEM Analysis of the Transient Oxidation of a Ni 20Cr Alloy at High Temperature," *Oxidation of Metals*, vol. 52, pp. 113–138, 1999. 3.3

[10] T. D. Nguyen, J. Q. Zhang, and D. J. Young, "Microstructures of chromia scales grown in CO2," *Materials at High Temperatures*, vol. 32, no. 1-2, pp. 16–21, 2015. 3.3

[11] M. Dunlevy, "An Exploration of the Effect of Temperature on Different Alloys in a Supercritical Carbon Dioxide Environment," Ph.D. dissertation, MIT, 2009. 3.3

[12] N. Birks, G. H. Meier, and F. S. Pettit, *Introduction to the High Temperature Oxidation of Metals*, 2006. [Online]. Available: http://www.cambridge.org/gb/knowledge/isbn/item1110694/?site{_}locale=en{_}GB 3.3

[13] H. J. Lee, H. Kim, S. H. Kim, and C. Jang, "Corrosion and carburization behavior of chromia-forming heat resistant alloys in a high-temperature supercritical-carbon dioxide environment," *Corrosion Science*, vol. 99, pp. 227–239, 2015. [Online]. Available: http://dx.doi.org/10.1016/j.corsci.2015.07.007 3.3, 3.3

[14] H. J. Lee, G. O. Subramanian, S. H. Kim, and C. Jang, "Effect of pressure on the corrosion and carburization behavior of chromia-forming heat-resistant alloys in high-temperature carbon dioxide environments," *Corrosion Science*, vol. 111, pp. 649–658, 2016. [Online]. Available: http://dx.doi.org/10.1016/j.corsci.2016.06.004

[15] R. I. Olivares, D. J. Young, P. Marvig, and W. Stein, "Alloys SS316 and Hastelloy-C276 in Supercritical CO2at High Temperature," *Oxidation of Metals*, vol. 84, no. 5-6, pp. 585–606, 2015. 3.3

[16] D. J. D. J. Young, *High temperature oxidation and corrosion of metals*, 1st ed. Elsevier, 2008. 3.3

[17] F. Rouillard and T. Furukawa, "Corrosion of 9-12Cr ferritic-martensitic steels in high-temperature CO2," *Corrosion Science*, vol. 105, pp. 120–132, 2015. [Online]. Available: http://dx.doi.org/10.1016/j.corsci.2016.01.009 3.3

[18] J. A. Colwell and R. A. Rapp, "Reactions of Fe-Cr and Ni-Cr alloys in CO/CO2 gases at 850 and 950 C," *Metallurgical Transactions A*, vol. 17, no. 6, pp. 1065–1074, 1986. 3.3

Chapter 4: Investigation of the hot-working behavior of advanced Ni-based superalloys

Benjamin Adam[a,b], Julie D. Tucker[a]

[a]Department of Mechanical, Industrial and Manufacturing Engineering, Oregon State University, Corvallis, Oregon 97331

[b]Department of Mechanical and Materials Engineering, Portland State University, Portland, Oregon, 97201

Submitted to Material Science and Engineering A on 5/1/2018

Three Ni-based superalloys, Haynes 214, Haynes 230 and Inconel 740H, have been analyzed for their mechanical behavior during into heat-exchanger components. These alloys and other comparable alloys are expected to be used in sCO_2 heat exchanger cycles as proposed for example in the DOE Advanced Ultra-Supercritical (A-USC) program, due to their unique combination of mechanical, corrosion and creep properties. However, these alloys are difficult to form, specifically for sCO_2 components, such as header pipes and manifolds, and therefore the optimal forming conditions need to defined. Hot-deformation test were then conducted in a thermal-mechanical testing system Gleeble 3500, at temperatures and strain rates expected during industrial conditions, which . The effect of using as-received material on the deformation

behavior was analyzed, to simulate actual microstructural conditions more accurately. The flow-stress curves for all three alloys showed the occurrence of dynamic recrystallization with some signs of dynamic recovery for the slowest strain rates and higher temperatures for all alloys. The activation energies for plastic flow were 246, 302 and 217 kJ/mol, for Haynes 214, Haynes 230 and Inconel 740H, respectively. The difference to other reported values in the literature was suggested to be an effect of the fine initial grain-size and omission of additional heat-treatment. Systematical errors during linear regression analysis in the constitutive equations were discussed. Hot-processing maps were generated for all alloys and suggest specific domains for optimal workability under the tested conditions. For Haynes 214, that is $\dot{\varepsilon} \leq 0.1/\text{s}$ and $\text{T} \geq 1050$ °C. For Haynes 230, it is $1050\ ^\circ\text{C} \leq \text{T} \leq 1150\ ^\circ\text{C}$ and $0.01/\text{s} \leq \dot{\varepsilon} \leq 0.5/\text{s}$. For Inconel 740H, it is $1010\ ^\circ\text{C} \leq \text{T} \leq 1075\ ^\circ\text{C}$ and $0.1/\text{s} \leq \dot{\varepsilon} \leq 0.1/\text{s}$.

4.1 Introduction

The advent of supercritical CO_2 (sCO_2) has marked a major change in the heat-exchanger technology for future power plants and the upgrade of current ones. Currently, such processes are either employing the gas-Brayton or the steam-Rankine cycle, both of which have drawbacks, limiting their overall efficiency [1]. The sCO_2 Brayton-cycle is advantageous due to is combination of beneficial thermo-physical properties, smaller turbomachinery size and higher thermal efficiency [2–4]. This process allows for turbine inlet temperatures of up to 750 °C 800 °C, resulting in efficiencies beyond 50%, as proposed by the US Department of Energy, as well as in the coal or solar power industries [5–9]. Based on these conditions, only Ni-based superalloys are considered, which form protective oxide films, such as chromia or alumina, [10]. Currently, the focus of research on material performance in sCO_2 environments has been on the corrosion for limited time exposures of up to 3000 hrs [3–5]. Beyond that, the requirements for long-term use in heat-exchanger systems have been defined, where a creep-rupture strength of 100 MPa at 100,000 h service time is desired, and that ASME BP&V code acceptability is ensured [6, 11, 12]. Only Inconel 740H and Haynes 282 have met this requirement so far, while Inconel 740H has been the only ASME-code certified alloy so far, and Haynes 282 is currently a candidate for future code-certification [2, 7, 13–17]. But other alloys, which are more established in the power industry, such as Haynes 214, Haynes 230, Inconel 617 and Inconel 625, have also shown acceptable corrosion performance in initial tests, and exhibit creep properties that are similar [5, 8, 9, 18]. Additionally, any of the potential alloys,

for use in sCO_2-systems, will have to be easily manufactured into the complex and intricately designs of current heat-exchangers. This requires precise information and knowledge of the workability of Ni-based alloys as the candidate material [19]. Further, the final microstructure-property relationships are affected by the workability of the material through the interaction of the deformation temperature, strain and strain rate, employed during the hot-working process.

During hot-working of Ni-based superalloys and other austenitic alloys, the governing metallurgical phenomenon is usually thought to be dynamic recrystallization (DRX), which counteracts the strain hardening from the mechanical working of the material [20–22]. Here, the stored dislocation density is reduced by the formation of new DRX grains, the increase of high-angle grain boundaries (HAGB) and increase of density of special boundaries. There are also other processes occurring during hot deformation, which are altering the microstructure dynamically, such as creep or adiabatic heating through lattice friction [20, 23]. All of these metallurgical processes of work hardening and softening are temperature-dependent and can thus be represented as a function of both temperature and other processing conditions. In early works, Raj et al. developed deformation maps that provided guidance on safe regions for processing, while avoiding areas prone to cracking or failure otherwise [24, 25]. Further advances in continuum mechanics and constitutive relationships between various parameters have led to the concept of Dynamic Materials Modeling (DMM), introduced by Prasad et al. [26–28]. Here, the concept is that the total amount of energy absorbed by the material during plastic deformation can be split up into power dissipation into plastic flow, G, and into metallurgical phenomena, J,

such as dynamic restoration, void formation, internal cracking or dissolution of secondary phases. J can thus be understood as framework to capture dynamic events based on thermodynamic and mechanistic models [28, 29].

As such, P can be defined as Eq. 4.1

$$P = G + J = \bar{\sigma}\dot{\bar{\varepsilon}} \tag{4.1}$$

Where $\bar{\sigma}$ is the instantaneous flow stress, and $\dot{\epsilon}$ the instantaneous strain rate. As J represents the energy transferred into metallurgical phenomena, it is parameter of interest, and can then be defined, for a given strain and temperature in Eq. 4.2

$$J = \int_0^{\bar{\sigma}} \dot{\bar{\varepsilon}} d\bar{\sigma} = \frac{\bar{\sigma}\dot{\bar{\varepsilon}} m}{m+1} \tag{4.2}$$

Here, m stands for the strain rate sensitivity, which is generally defined by the strain-rate dependence of the flow-stress in the constitutive equations. For a value of m=1 in an ideal case of total power dissipation, Eq. 4.2 can be simplified to J_{max} and be defined as Eq. 4.3

$$J_{max} = \frac{\bar{\sigma}\dot{\bar{\varepsilon}}}{2} \tag{4.3}$$

With this, the dimensionless parameter for the efficiency of power dissipation, η, can be defined in Eq. 4.4.

$$\eta = \frac{J}{J_{max}} = \frac{2m}{m+1} \tag{4.4}$$

This value can then be plotted in power dissipation or processing maps, for a constant strain over temperature and strain rate. DMM is a commonly used approach to model the processing conditions for Ni-based alloys [30–36]. However, there has been limited research conducted in the recent years on the promising alloys for sCO_2 exposure, see for example Liu et al. for Haynes 230, or Wang et al. for Inconel 740H [37, 38]. Some limited research has been done in generally studying the manufacturing process to a finished heat-exchanger module, such as steam header or pipe for 740H [39, 40]. Due to the complexity in shapes of heat-exchangers, the material will be subjected to large strains during forging into final shapes [19, 41].

Therefore, in this study, the hot deformation behavior will be studied using hot-compression testing in order to understand mechanical response in isothermal forging conditions. Hot-processing maps and power dissipation maps will be used as tools to assess the formability of the selected alloys. Further, constitutive relationships between the variables influencing the flow stress behavior are evaluated and compared between the alloys. This directly links the strain rate, flow stress and temperature through the use of the Zener-Holloman parameter. This will ultimately aid in the the understanding of how the alloys respond microstructurally to hot deformation, as a function of dynamic recrystallization and processing conditions. In this work only the flow-stress data, the constitutive modeling and the hot-processing maps are being considered. In a forthcoming work, the post-recrystallization microstructures will be analyzed, where the property-microstructure relationships will be analyzed.

4.2 Experimental methods

All alloys used in this study were acquired from commercial vendors, with chemical compositions of the respective alloys given in Table 4.1. It should be noted that all alloys were tested in their as-received, solution-annealed state, including the precipitation-hardenable alloy 740H. This was determined to be more useful as any forming and forging processes would be conducted on as-hot-rolled or as-cogged material.

Table 4.1: Chemical composition of studied alloys, in wt-%

Alloy	Ni	Cr	W	Mo	Fe	Co	Al	Ti	Nb	C
Haynes 214	*	16.64	0.03	0.1	3.94	0.05	4.25	–	–	0.04
Haynes 230	*	22	14	2	3	5	0.3	–	–	0.1
Inconel 740H	*	24.5	–	0.1	–	20	1.35	1.35	1.5	0.03

(* denotes balancing element)

Samples were cut and machined using wire electric discharge machining (EDM) from as-received plates into final samples size of 8 mm x 12 mm (diameter x height). Hot deformation experiments were carried out by isothermal compression testing in a Gleeble 3500 ®. The testing was performed at temperatures between 1000 ℃ and 1200 ℃ in 50 ℃ increments, and strain rates of 0.01/s, 0.1/s and 1/s. All the tests were run to a true strain of 0.7. The chamber atmosphere was controlled by evacuating to 1×10^{-2} mTorr and subsequent backfilling with research-grade argon gas. The heating rate used was 2.5 ℃/s, after which samples were soaked at the test temperature for 30 s, to ensure thermal equilibrium, before compression, during which the temperature was maintained. In order to maintain proper interface lubrication

between the tungsten-carbide cobalt anvils and the samples, 0.125 mm thick graphite foil was used. After the deformation was done, samples remained in the chamber and cooled naturally by heat conduction through the anvils and heat convection through the gas. Using recorded data from attached thermocouples, the cooling rate was determined to be around 60 ℃ for the first few hundred degrees, when cooling from the highest temperature of 1200 ℃. Adiabatic heating corrections have been carried out in order to correct for the effect of heat, due to internal friction, on the flow stress curve. Various correction methods are proposed in the literature, including studies involving numerical solutions using FEM-simulations of hot-compression tests [42] and complex iterative approaches [43]. However, the more commonly used approach is shown in Eq. 4.5 [44, 45].

$$\Delta T = \frac{\eta\alpha \int_0^{\epsilon} \sigma \, d\varepsilon}{\rho C_p} \tag{4.5}$$

Here, σ and ε are the stress and strain values recorded from the compression tests. α corresponds to the amount of deformation energy transformed into heat, which is usually assumed to be 0.95-0.98, while η stands for the adiabatic correction factor. η is assumed to change between $\eta = 0$ for strain rates $\leq 10^{-3}s^{-1}$ and $\eta = 1$ for strain rates $\geq 10^{1}s^{-1}$. The integral $\int \sigma d\epsilon$ represents the area underneath the uncorrected stress-strain curve, ρ is the material density of 8.05 g/cm^3 for Inconel 740H and Haynes 214, and 8.97 g/cm^3 for Haynes 230. C_p is the temperature-dependent heat capacity in J/(kg C), which is defined using a linear fit on the reported specific heat values for the corresponding temperature range from the manufacturer's datasheet

[46–48].

Eq.4.5 is generally correcting for the amount of heat transferred to the dies during adiabatic heating. In this study the values for η have been defined for each strain rate, based upon comparable values from the literature, i.e. for strain rate of 0.01/s a value of 0.1, for 0.1/s a value of 0.5, and for 1.0/s a value of 0.9 [42, 49, 50]. The flow stress can then be corrected by Eq.4.6 [25, 51].

$$\Delta\sigma = \Delta T(\frac{\partial\sigma}{\partial T}) \tag{4.6}$$

Whereby $\partial\sigma/\partial T$ is obtained by plotting the uncorrected flow stress values at low true strain values (here: $\varepsilon = 0.02$) against the temperature, and calculating the first derivative of a linear regression to the curve.

4.3 Results and Discussion

4.3.1 Flow stress analysis

The flow-stress curves generated by the Gleeble for all three alloys are presented in Figure 4.1, after correction for adiabatic heating was applied. In general, all alloys follow the trend of increasing flow stress with a decrease in temperature and increase in strain rate. At the lower strain rates of 0.01/s and 0.1/s, a specific sequence of fast strain-hardening, followed by attaining the peak stress and subsequent strain-softening, was observed for all alloys. The single peak is usually associated

with the occurrence and onset of DRX [21, 52, 53]. As apparent by the oscillations in the flow-stress curve at lower to medium temperatures at low strain rates, the stress-strain-curves can also show multiple peaks. This can be related to a low Zener-Hollomon-parameter, Z, or low flow-stress conditions, that allow for a rather complete recrystallization event during one cycle, a cycle being the time it takes the material to build up dislocation density due to physical deformation [21, 52]. At higher flow-stress conditions, higher Z values or faster strain rates, the individual recrystallization cycles start to overlap, which gradually forms a single peak. Of further importance is, that the peak strain starts to increase and attain a plateau of near steady-state stress, as the strain rate increases from 0.1/s to 1.0/s, with decreasing temperature, which also has been observed elsewhere [54]. This suggests the metallurgical behavior changing from DRX to a more Dynamic Recovery (DRV)-related mechanism. Here, the dislocations are stored in subgrains, that show an increase in average misorientation during continued deformation, until a recrystallized microstructure is obtained [45, 53]. When comparing the different alloys, it was noticed that Haynes 214 showed lower flow-stress values, by a factor of 2, than the other two alloys, during at all conditions. Interestingly, Haynes 214 did not show the same effect of DRV that both other alloys exhibited, yet continued to present a flow-stress behavior similar to the other alloys, for the lower strain rates. In general, the alloys can be grouped by the intensity of the DRX occurrence, from most intense for Haynes 230 to least for Haynes 214. Inconel 740H did even exhibit signs of continued strain hardening at lower temperatures at a strain rate of 1/s, which may be a false interpretation, due to fitting error introduced during adiabatic correction.

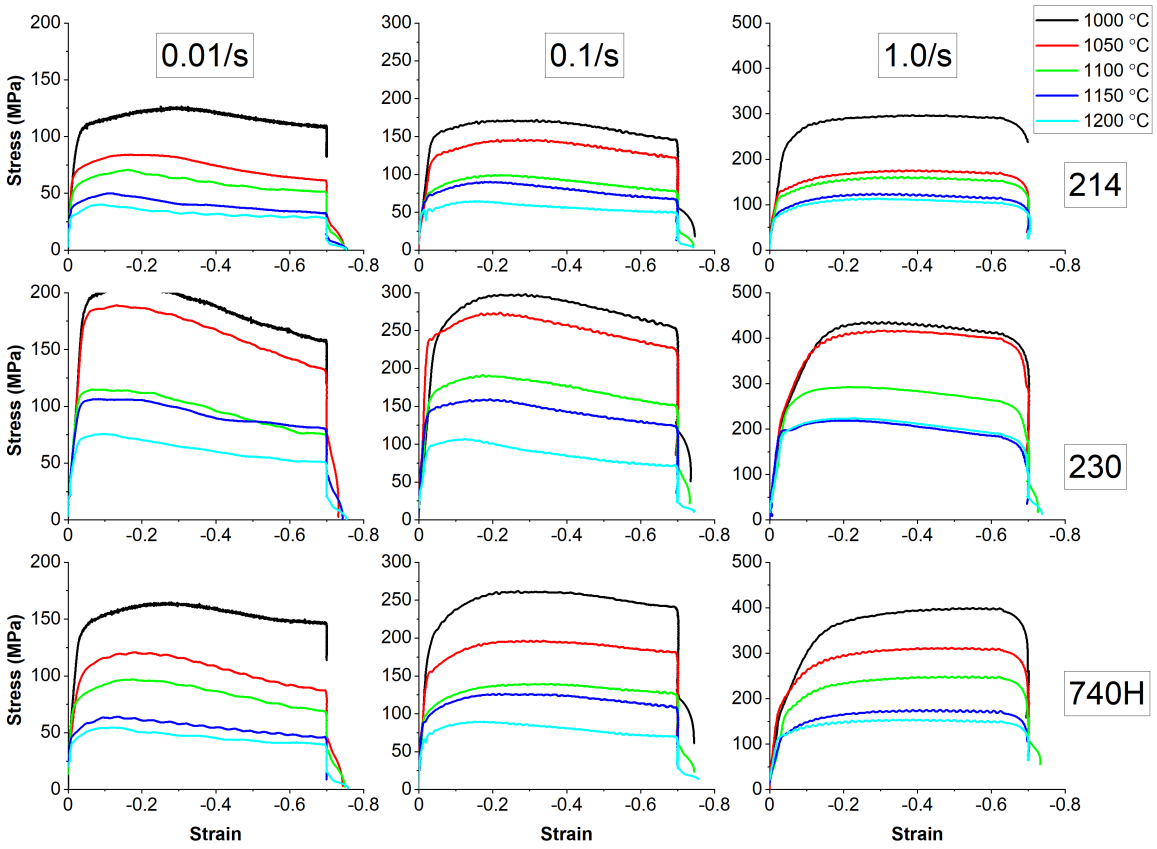

Figure 4.1: Corrected flow stress curves for all alloys, at different strain rates and temperatures.

Analysis of the strain-rate dependence of the steady-state flow-stress at $\epsilon_T = 0.5$ was performed and is shown in Figure 4.2. It can be seen that all alloys follow linear relationships for their flow-stress behavior, where the slope of the linear fit gives the strain-rate sensitivity parameter, m. It appears that m is generally linearly increasing with the temperature for all alloys.

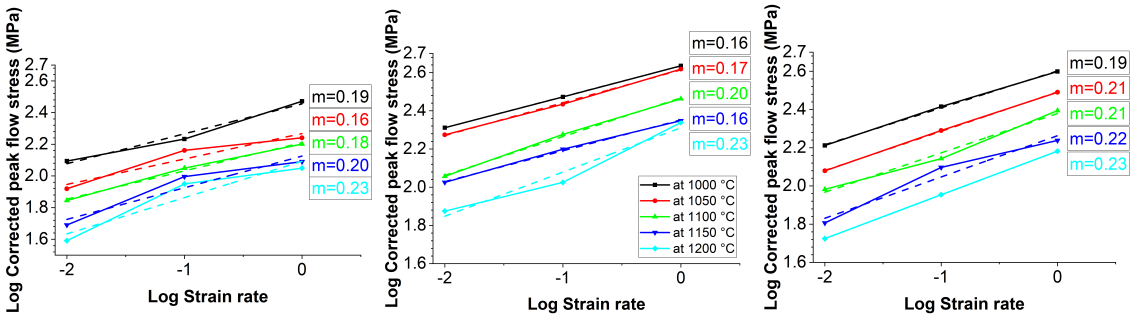

(a) Haynes 214 (b) Haynes 230 (c) Inconel 740H

Figure 4.2: Strain rate sensitivities for all studied alloys

Comparison of the flow-stress results with the as-received microstructures of all materials allows further understanding of the flow behavior. In general, all alloys show a uniform and equiaxed, austenitic matrix, in Figure 4.3. The as-received grain sizes of Inconel 740H, Haynes 230 and Haynes 214 were $82 \pm 38\ \mu m$, $51 \pm 28\ \mu m$ and $80 \pm 36\ \mu m$, respectively.

Both Inconel 740H and Haynes 214 have a wide range of grain sizes, however not bimodal in nature, with similar mean grain sizes. Haynes 230 shows in constrast a much smaller average grain size than the other two alloys. However, the influence of the omitted heat-treatment on the grain size for all alloys is evident. For Haynes 230, the grain size is reported at 70 μm by various researchers, after an additional solutionizing at 1230 ℃ [37, 55, 56]. No comparable grain size data was found for Haynes 214. For Inconel 740H, literature data suggests as-received grain sizes around 90-100 μm, after a solution heat-treatment of 1170 ℃ [57, 58] [57, 58]. That means, for all alloys, the grain size in the as-received condition is considerably smaller than otherwise found in the literature.

Both Haynes 214 and Haynes 230 also show a considerable amount of secondary phases in their matrix, while Inconel 740H does not show any. For Haynes 214, the chemical composition suggests the possible formation of γ'-phases, which is assumed to be the phase found in the as-received microstructure in 4.3a. Generally, the γ'-phase confers strength at elevated temperature, thus is expected to increase the flow stress. Therefore, exposures at or above the γ'-prime dissolution temperature, may lead to a decrease in flow stress, as indeed observed in Figure 4.1.

For Haynes 230, the microstructure shows precipitates both intra- and intergranularly, these are primarily assumed to be tungsten-rich M_6C-type carbides, based on composition and related research [37, 59]. Also, a $M_{23}C_6$-type carbide and the μ-phase are thermodynamically stable to form and have been seen. It is assumed that these phases may increase flow stress or prevent a decrease flowstress through grain boundary pinning and precipitation hardening. However, above 1050 ℃ the thermal stability range of the $M_{23}C_6$-phase and the μ-phase are decreasing, leading to a net decrease in flow-stress, as seen in Figure 4.1.

As Inconcel 740H did not show any precipitates, the flow stress is assumed to be only affected by grain growth of the matrix grains.

4.3.2 Constitutive modeling

In general, constitutive equations applied to hot-deformation are evaluating the relationships between temperature, strain rate and strain and are used to describe generally hot processing behavior [44, 60–62]. A generalized form of such a constitutive

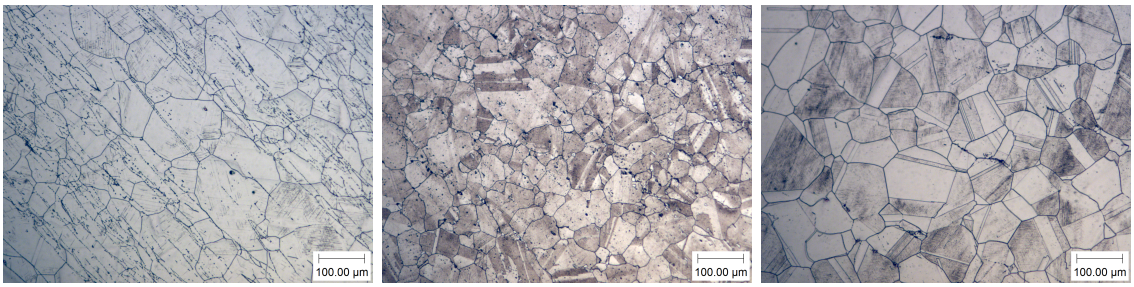

(a) Haynes 214 (b) Haynes 230 (c) Inconel 740H

Figure 4.3: Base-metal microstructures of as-received material of all studied alloys, acetic glyceregia etch.

equation could be written as Eq.4.7.

$$\bar{\sigma} = f(\bar{\varepsilon}, \dot{\bar{\varepsilon}}, T) \tag{4.7}$$

With $\bar{\sigma}$, $\bar{\varepsilon}$, $\dot{\bar{\varepsilon}}$ and T being the true flow stress, the true flow strain, the true flow strain rate and deformation temperature. In this work, $\bar{\sigma}$ will be chosen as the peak stress, as the steady-state stress is only rarely reached in higher strain rate cases [54], as was the case in this study as well. One of the earliest works on constitutive equations, that brings all three variables together is by Sellars and Tegart, as well as more recently by McQueen and Ryan [44, 63], Eq. 4.8

$$\dot{\bar{\varepsilon}} = A[sinh\ (\alpha\bar{\sigma})]^{n'} e^{-\frac{Q}{RT}} \tag{4.8}$$

In here A, α, n' are material constants and Q is the apparent activation energy in kJ/mol needed to activate plastic flow, while R is the universal gas constant, here as 8.314 J/(K mol). Furthermore, the right, exponential part of the equation can be

displayed as the well-known Zener-Holloman equation, Eq. 4.9 and 4.10

$$Z = \dot{\bar{\varepsilon}}\ e^{\frac{Q}{RT}} \tag{4.9}$$

$$Z = A[sinh\ (\alpha\bar{\sigma})]^{n'} \tag{4.10}$$

Eq. 4.9 incorporates both T and ε, which allow a more convenient description of the relationships between flow stress and strain rate [64]. Eq.4.8 uses a hyperbolic sine approach, which is the generally applicable equation for describing the entire flow stress curve. But for certain ranges of the parameter $\alpha\bar{\sigma}$, the equation can be simplified [44, 65, 66]. If $\alpha\sigma < 0.8$, a power law relationship can be used to instead of the hyperbole in Eq. 4.8, in Eq. 4.11

$$\dot{\varepsilon} = A_1\bar{\sigma}^{n'}e^{-\frac{Q}{RT}} \tag{4.11}$$

For $\alpha\sigma > 1.2$, an exponential function can be used instead, Eq.4.12

$$\dot{\varepsilon} = A_2e^{\bar{\sigma}\beta}e^{-\frac{Q}{RT}} \tag{4.12}$$

The unknown parameters in Eq. 4.8, A, α, and n', can thus be determined by using the simplified relationships in Eq. 4.11 and Eq. 4.12 along with the approximation that $\alpha = \beta/n'$. Both equations can be solved for n' and β by applying the natural logarithm and partially differentiating after the stress. This way, one obtains Eq.

4.13 and 4.14.

$$\left(\frac{\partial\ ln\ \dot{\varepsilon}}{\partial\ ln\ \sigma_p}\right)_T = n_1 \tag{4.13}$$

$$\left(\frac{\partial\ ln\ \dot{\varepsilon}}{\partial \sigma_p}\right)_T = \beta \tag{4.14}$$

Therefore, plotting the ln $\dot{\varepsilon}$ against ln σ_p, and ln $\dot{\varepsilon}$ against σ_p, respectively, and performing a linear regression fit, gives the values for n_1 and β. The mean values for each parameter are calculated and then a value for α can be derived for all alloys.

The exponent n', the activation energy Q and the Zener-Holloman parameter Z can all be solved following similar linear regressions, found elsewhere described in more detail [65].

The relationships between the flow-stress and the temperature for all alloys are shown in Figure 4.4a, 4.4b and 4.4c.

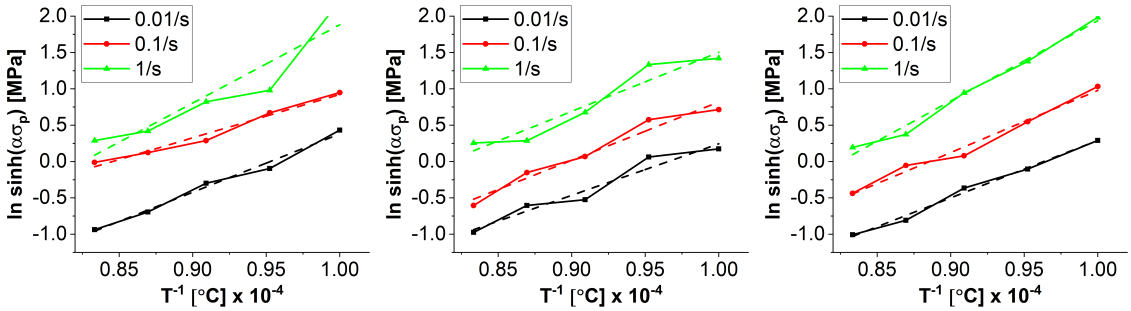

(a) Haynes 214 (b) Haynes 230 (c) Inconel 740H

Figure 4.4: Flow-stress dependence on deformation conditions

Table 4.2: Material parameters determined by constitutive equations for studied alloys

Alloy	Q, avg.[kJ mol^{-1}]	Q, SD [kJ mol^{-1}]	n'	α [MPa^{-1}]	A [s^{-1}]
Haynes 214	246	58	3.58	0.00981	1.85 x 10^{10}
Haynes 230	302	44	3.96	0.00493	1.46 x 10^{13}
Inconel 740H	217	13	3.37	0.00675	9.62 x 10^{8}

All material parameters for all alloys are shown in Table 4.2. With the values in Table 4.2, the relation in Eq.4.8 can be solved and defined for the three alloys, see for Haynes 214 in Eq.4.15, for Haynes 230 in Eq.4.16 and for Inconel 740H in Eq.4.17.

$$\dot{\varepsilon} = 1.85\ x\ 10^{10}[sinh(0.00981\sigma_p)]^{3.58}\ exp\left(\frac{-245663}{RT}\right) \tag{4.15}$$

$$\dot{\varepsilon} = 1.46\ x\ 10^{13}[sinh(0.00493\sigma_p)]^{3.96}\ exp\left(\frac{-301972}{RT}\right) \tag{4.16}$$

$$\dot{\varepsilon} = 9.62\ x\ 10^{8}[sinh(0.00675\sigma_p)]^{3.37}\ exp\left(\frac{-216773}{RT}\right) \tag{4.17}$$

In general, the activation energy ranges reported for Ni-based superalloys can stretch between 300 to 1500 kJ/mol [67–69]. For the tested alloys the values of Q are fairly low, as compared with values reported by other researchers [38, 55, 65, 70]. When comparing the values for Haynes 230, the activation energy of 302 kJ/mol is considerably lower than reported by Liu et al. at 425 and 404 kJ/mol, respectively [37]. However, the standard deviation is considerable, as the mean activation energy accounts for the entire range of tested strain rates. In this study, the standard devi-

ation is 44 kJ/mol for strain rates between 0.01/s and 1.0/s, while Liu et al. shows 70 kJ/mol for strain rates between 0.001/s and 10/s. The solution treatment temperature used was 1230 ℃ for 2 h. For Inconel 740H, Wang et al. reported in two different studies average values of 357 and 374 kJ/mol for the activation energy, for two comparable strain rate ranges between 0.01/s and 30/s. The solution treatment temperature used in this case, was 1170 ℃ for 30 min. No standard deviation was reported in either study, however it is unlikely that it would include the reported value of 217 kJ/mol.

It is assumed that the deviations in activation energy are due to the omission of a dedicated solution heat-treatment before the deformation testing. As noted previously in the discussion of the as-received microstructures, an additional, initial heat-treatment resulted in the dissolution of secondary, strengthening phases. It is plausible that the flow-stress decrease due to the selective dissolution during compression for the alloys in this study affected the activation energy reported. It was noted that the presence of secondary phases [36, 70] can increase the flow-stress and decrease softening mechanisms, which also affects the related parameters, such as n' and Q. An additional solution treatment can then also lead to a severely increased grain size through dissolution of grain-boundary-pinning secondary phases in general, that would otherwise affect the deformation behavior [71]. It is useful to understand how other metallurgical factors are influencing the activation energy. For example, in a comprehensive study, Bi et al. determined the contribution of various alloying elements to Q [67]. The influence of the alloying additions on the deformation activation energy can be understood by the presence of elements with different atomic sizes

than the matrix, creating stress fields around them [20, 72]. These regions then create hindrances for dislocation movemements during plastic deformation, thus increasing the necessary deformation activation energy to bypass or cut them [55].

Other factors that are influencing the activation energy are other phases, for example in two-phase systems [60]. Here, large differences between the energies were reported, for the two-phase alloy versus the phases taken by themselves. This phenomenon can be utilized to describe deviations for γ'-forming alloys, such as Inconel 740H. In fact, Monajati et al. found for UDIMET720, a γ'-forming Ni-based superalloy, a correlation between the γ'-fraction and the activation energy [73]. When mapping Q over temperature and strain-rate sensitivity m, the results showed that once the fraction of the strengthening phase increases, below its dissolution temperature, much higher values of Q are necessary to activate massive plastic flow.

Further, the influence of strain that a workpeice is subjected to, during deformation, shows a direct correlation with the activation energy, studied by both Deghan et al. and Bruni et al. [68, 74]. Generally, trends appear to be directly influenced by the underlying stacking fault energy (SFE) for the respective material, which in turn governs the work softening mechanism, either DRV or DRX. The SFE tends to be lower in materials that are showing a higher ratio of fcc-stabilizing to bcc-stabilizing elements, making the occurrence of DRX more prevalent than DRV in most Ni-based alloys [52]. While Q was shown to increase with strain in general [68, 75], other studies also found an inverse relationship [74]. This is assumed to be partially due to the energy necessary to move grain boundaries being larger under DRX conditions than DRV conditions. Then, it is likely, that materials with an earlier onset of DRX,

and related higher density of mobile grain boundaries, tend to require less energy to continue deformation, than materials that experienced more DRV in the beginning. In addition, it was mentioned that the initial grain size may play yet another role, as the critical dislocation density for DRX activation may be reached sooner for finer grains than coarser ones [54, 70]. It should also be noted that no consistent trend could be observed between strain rate and activation energy. This is reflected by research other studies on this topic. While some showed a trend of decreasing activation energy with increasing strain rate, others, including this study, did show no trend at all [37, 76].

4.3.3 Hot-processing maps

In order to successfully define optimum processing windows for the alloys to be manufactured into their final shapes, investigation of the formability at different temperature/strain rate conditions is useful. The hot processing maps for all alloys can be seen in Figure 4.5, for two selected strain levels, the strain at peak stress and $\varepsilon = 0.5$, corresponding to industrially interesting strain ranges. For Haynes 214, it is apparent that both higher temperatures and lower strain rates are beneficial if flow instabilities should be avoided. According to Prasad's studies, the beneficial regime that allows for operating between $30 - 50\%$ efficiency, is associated with DRX, which implies low flow-stress and work softening, also high ductility [26]. Further, when comparing the different strains, it is noticeable that Haynes 214 shows a fairly constant profile, with little difference in general appearance of the processing maps. Changes in dissipation

efficiency when altering deformation conditions are becoming slightly more sluggish for the higher strain condition. This alloy can be considered of having many domains of optimum workability with not clearly defined boundaries. But generally, temperatures above 1050 °C and strain rates slower than 0.1/s are within the optimum range [26, 77].

Haynes 230 also shows a relatively small dependence of the general hot processing behavior on the strain levels, only the efficiency levels differ. It was noticeable that this alloy showed very sluggish kinetics, with large areas of iso-efficiency contours, see Figure 4.6b. However, in general agreement with studies by Liu et al. on Haynes 230 [37, 55], a domain between 1050 °C and 1150 °C, and strain rates of 0.01/s and 0.5/s. There is a second domain, that is present at the highest temperature range between 1150 °C and 1200 °C, above a strain rate of 0.1/s. Here, the power dissipation efficiency is very sensitive to the deformation conditions, and attains peak values of almost 60%. This may associated with fast dissolution kinetics of secondary phases, likely carbides, that previously had pinned grain boundaries and provided nucleation sites for DRX, and now allow grain growth and coarsening to take place [37, 69, 78]. For Inconel 740H, two distinct domains could be found, which both increased in area with increasing strain. One is at a lower temperature range between 1025 °C and 1075 °C and one is a higher temperature range between 1125 °C and 1175 °C, see Figure 4.7a. Both are extending for strain rates between 0.01/s and 0.1/s. Both domains could be associated with oscillations in the flow stress at the slowest strain rate end. However, at the higher strain rate end, the higher temperature domain did still show remnants of oscillation in the flow-stress curve, in contrast to the lower temperature

one. This process was associated with cyclic recrystallization, as mentioned above, which involves grain coarsening in addition to DRX events [21]. In general agreement with similar findings by Wang et al. for 740H, the higher temperature domain may be related to dissolution of γ'-phases [54].

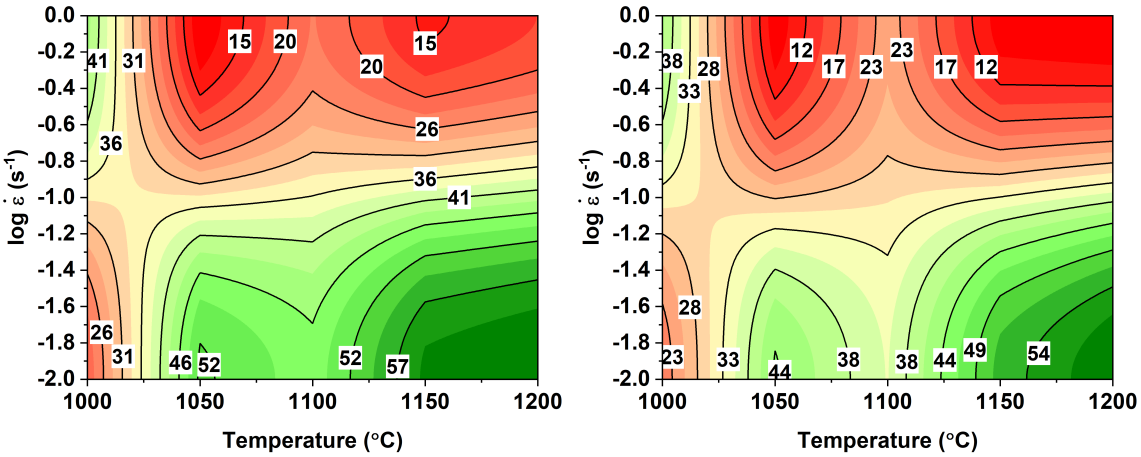

(a) True strain of 0.5

(b) True peak strain

Figure 4.5: Hot-processing maps for Haynes 214 at two selected true strain values.

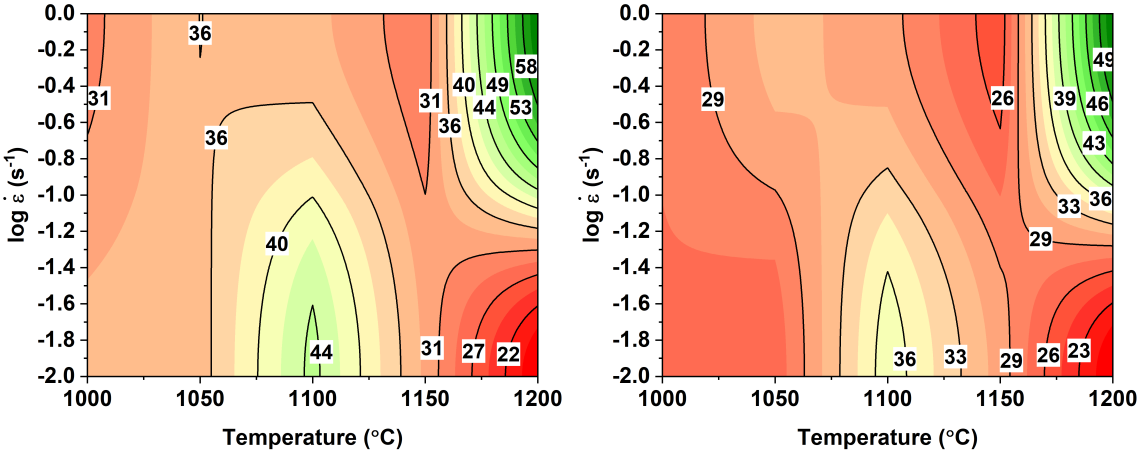

(a) True strain of 0.5 (b) True peak strain

Figure 4.6: Hot-processing maps for Haynes 230 at two selected true strain values.

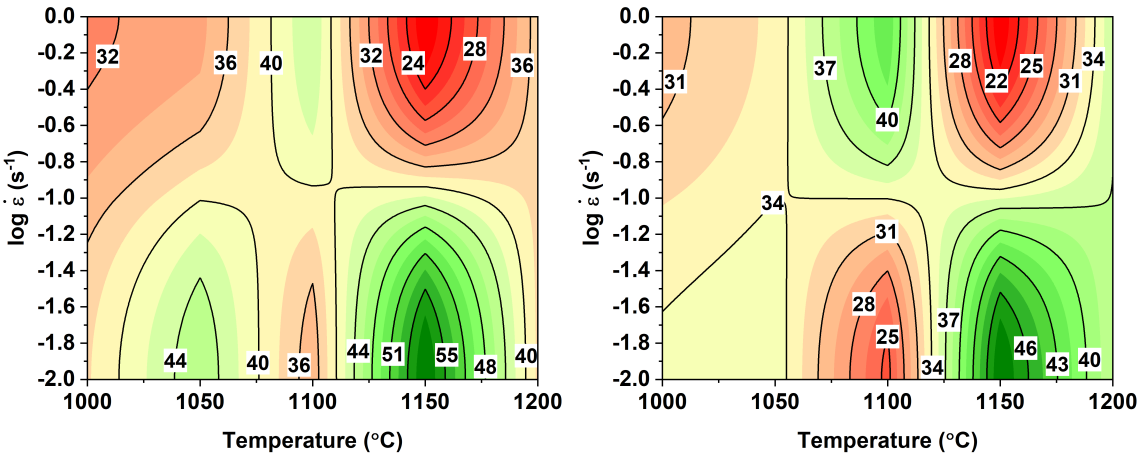

(a) True strain of 0.5 (b) True peak strain

Figure 4.7: Hot-processing maps for Inconel 740H at two selected true strain values.

4.4 Conclusions

The hot-processing behavior of three Ni-based superalloys suggested for use in sCO_2 applications was investigated. Thermo-mechanical testing was carried out in a Gleeble 3500 machine on as-received, non-heat-treated samples. Relationships between the parameters governing the hot-workability were analyzed, and general constitutive equations linking all parameters were formulated. Presence of DRX, with initial work hardening and occurrence of a single peak in the flow-stress, were found in all alloys under all conditions, while at lower strain rates and higher temperatures, signs of DRV were found. The stress levels, for the different temperature-strain rate combinations, were within the ranges reported for the same alloys by other researchers. It was found that all alloys showed values for the apparent activation energies of deformation that were substantially lower than the ones found in the literature for similar Ni-based superalloys. The reasons were assumed to be a combination of different factors. On the one hand, the initial microstructure, both in terms of the grain size and the secondary phases present, and on the other hand the spatial variations in the alloying concentrations in the matrix. It was also determined that the standard procedures used in the constitutive equations may induce certain errors through linear regression and averaging steps, which need to be taken into consideration when performing comparisons. The hot-processing maps for Haynes 214 suggest general good workability for a wide range of conditions, at $\dot{\varepsilon} \leq 0.1/s$ and $T \geq 1050$ °C. Haynes 230 showed slow kinetics of the deformation conditions for most of the testing range. Generally, the optimum operating range is 1050 °C $\leq T \leq$ 1150 °C and $0.01/s \leq \dot{\varepsilon} \leq 0.5/s$. For

Inconel 740H it was determined that the optimum processing range should be below the γ'-dissolution temperature, in order to obtain a fine-grained structure. Therefore, it was suggested to use 1010 °C $\leq T \leq$ 1075 °C and $0.01/s \leq \dot{\varepsilon} \leq 0.1/s$.

4.5 Acknowledgements

The authors would like to thank Dr. George Young at Dominion Engineering in Reston, VA for the valuable help in proofreading and the technical discussions about this paper.

4.6 Bibliography

[1] G. E. Rochau, J. J. Pasch, B. Cycle, P. Investigator, G. Cannon, M. Carlson, D. Fleming, R. Sharpe, and M. Wilson, "Supercritical CO2 Brayton Cycles," Sandia National Labs, Tech. Rep., 2014. 4.1

[2] C. Oh, T. Lillo, W. Windes, T. Totemeier, and R. Moore, "Development of a supercritical carbon dioxide Brayton cycle: improving PBR efficiency and testing material compatibility," INL, Tech. Rep., 2006. 4.1

[3] R. G. Brese, J. R. Keiser, and B. A. Pint, "Effect of Thermal Cycling on Compatibility in CO2 for Concentrated Solar Power Applications," *Oxidation of Metals*, vol. 87, no. 5-6, pp. 631–642, 2017. [Online]. Available: http://link.springer.com/10.1007/s11085-017-9762-0 4.1

[4] G. R. Holcomb, C. Carney, J. A. Hawk, Ö. N. Doan, K. Rozman, and M. H. Anderson, "Materials Performance in Supercritical CO2 in Comparison with Atmospheric Pressure CO2 and Supercritical Steam," *The 5th International Symposium - Supercritical CO2 Power Cycles*, 2016. 4.1

[5] B. A. Pint, K. A. Unocic, R. G. Brese, and J. R. Keiser, "Characterization of chromia scales formed in supercritical carbon dioxide," *Materials at High Temperatures*, no. October, pp. 1–11, 2017. 4.1

[6] R. Viswanathan, R. Purgert, and U. Rao, "Materials technology for advanced coal power plants," *Advanced materials & processes*, vol. 162, no. 8, pp. 73–76, 2004. [Online]. Available: https://www.phase-trans.msm.cam.ac.uk/2005/LINK/188.pdf 4.1

[7] J. Shingledecker, R. Purgert, and P. Rawls, "Current Status of the U.S. Doe/CDO A-USC Materials Technology Research and Development Program," in *7th International Conference on Advances in Materials Technology for Fossil Power Plants*, 2013, pp. 41–52. 4.1

[8] B. Pint, R. Brese, and J. Keiser, "Effect of pressure on supercritical CO 2 compatibility of structural alloys at 750 C," *Materials and Corrosion*, vol. 68, no. 2, pp. 151–158, feb 2017. [Online]. Available: http://doi.wiley.com/10.1002/maco.201508783 4.1

[9] R. Purgert, "Materials for Advanced Ultra- supercritical Steam Turbines - Advanced Ultra-supercritical Component Demonstration," Tech. Rep., 2016. 4.1

[10] V. Firouzdor, K. Sridharan, G. Cao, M. Anderson, and T. R. Allen, "Corrosion of a stainless steel and nickel-based alloys in high temperature supercritical carbon dioxide environment," *Corrosion Science*, vol. 69, pp. 281–291, 2013. [Online]. Available: http://dx.doi.org/10.1016/j.corsci.2012.11.041 4.1

[11] J. Phillips and J. Shingledecker, "US Department of Energy and Ohio Coal Development Office Advanced Ultra-Supercritical Materials Project for Boilers and Steam Turbines," Tech. Rep. March 2011, 2011. 4.1

[12] X. Xie, Y. Wu, C. Chi, and M. Zhang, "Superalloys for Advanced Ultra-Super-Critical Fossil Power Plant Application," in *Superalloys*, 1st ed., Mahmood Aliofkhazraei, Ed. InTech, nov 2015, ch. 3, p. 26. [Online]. Available: http://www.intechopen.com/books/superalloys/superalloys-for-advanced-ultra-super-critical-fossil-power-plant-application 4.1

[13] N. D. Evans, P. J. Maziasz, R. W. Swindeman, and G. D. Smith, "Microstructure and phase stability in INCONEL alloy 740 during creep," *Scripta Materialia*, vol. 51, no. 6, pp. 503–507, 2004. 4.1

[14] S. Zhao, F. Lin, R. Fu, C. Chi, and X. Xie, "Microstructure evolution and precipitates stability in 740H during creep," in *Advances in Material Technology for Fossil Power Plants*, 2013.

[15] A. Brittan, J. Mahaffey, M. Anderson, and K. Sridharan, "Mechanical and Corrosion Performance of the Weld of 740H and 282," in *The 6th International Symposium - Supercritical CO2 Power Cycles*, 2018.

[16] J. A. Hawk, T. Chen, J. S. Sears, Y. Wen, P. D. Jablonski, C. Miller, V. Cedro, K. Schrems, B. Romanosky, D. Alman, and P. Turner, "Creep Optimization in Haynes 282 Through Gamma Prime Coarsening Control : Preliminary Results," NETL, Tech. Rep., 2016.

[17] C. J. Boehlert and S. C. Longanbach, "A comparison of the microstructure and creep behavior of cold rolled HAYNES® 230 alloy and HAYNES® 282 alloy," *Materials Science and Engineering A*, vol. 528, no. 15, pp. 4888–4898, 2011. 4.1

[18] H. J. Lee, G. O. Subramanian, S. H. Kim, and C. Jang, "Effect of pressure on the corrosion and carburization behavior of chromia-forming heat-resistant alloys in high-temperature carbon dioxide environments," *Corrosion Science*, vol. 111, pp. 649–658, 2016. [Online]. Available: http://dx.doi.org/10.1016/j.corsci.2016.06.004 4.1

[19] M. Carlson, A. Kruizenga, C. Schalansky, and D. Fleming, "SANDIA PROGRESS ON ADVANCED HEAT EXCHANGERS FOR SCO2 BRAYTON CYCLES," in *The 4th International Symposium - Supercritical CO2 Power Cycles*, Pittsburgh, 2014, pp. 1–10. 4.1, 4.1

[20] G. Gottstein, *Physical Foundations of Materials Science*. Springer Berlin Heidelberg, 2004. [Online]. Available: https://books.google.com/books?id=qPIRngEACAAJ 4.1, 4.3.2

[21] T. Sakai and J. Jonas, "Dynamic recrystallization: Mechanical and microstructural considerations," *Acta Metallurgica*, vol. 32, no. 2, pp. 189–209, feb 1984. [Online]. Available: https://www.sciencedirect.com/science/article/pii/000161608490049X 4.3.1, 4.3.3

[22] A. Laasraoui and J. J. Jonas, "Prediction of steel flow stresses at high temperatures and strain rates," *Metallurgical Transactions A*, vol. 22, no. 7, pp. 1545–1558, jul 1991. 4.1

[23] T. Sakai, A. Belyakov, R. Kaibyshev, H. Miura, and J. J. Jonas, "Dynamic and post-dynamic recrystallization under hot, cold and severe plastic deformation conditions," *Progress in Materials Science*, vol. 60, no. 1, pp. 130–207, 2014. [Online]. Available: http://dx.doi.org/10.1016/j.pmatsci.2013.09.002 4.1

[24] R. Raj, "Development of a Processing Map for Use in Warm-Forming and Hot-Forming Processes," *Metallurgical Transactions A*, vol. 12, no. 6, pp. 1089–1097, 1981. 4.1

[25] H. L. Gegel, J. C. Malas, S. M. Doraivelu, and V. Shende, "Volume 14: Forming and Forging," in *ASM Handbook Vol. 14: Forming and Forging*, S. L. Semiatin, Ed. ASM International, 2004, vol. 14. 4.1, 4.2

[26] Y. V. Prasad, H. L. Gegel, S. M. Doraivelu, J. C. Malas, J. T. Morgan, K. A. Lark, and D. R. Barker, "Modeling of dynamic material behavior in hot deformation: Forging of Ti-6242," *Metallurgical Transactions A*, vol. 15, no. 10, pp. 1883–1892, 1984. 4.1, 4.3.3

[27] Y. Prasad and S. Sasidhara, *Hot Working Guide: A Compendium of Processing Maps*, 1st ed. Materials Park, OH: ASM International, 1997. [Online]. Available: https://books.google.com/books?id=orphpC0hEYoC

[28] Y. V. Prasad, "Processing maps: A status report," *Journal of Materials Engineering and Performance*, vol. 22, no. 10, pp. 2867–2874, 2013. 4.1

[29] S. V. Murty and B. N. Rao, "On the dynamic material model for the hot deformation of materials," *Journal of Materials Science Letters*, vol. 18, no. 21, pp. 1757–1758, 1999. 4.1

[30] D. Cai, L. Xiong, W. Liu, G. Sun, and M. Yao, "Characterization of hot deformation behavior of a Ni-base superalloy using processing map," *Materials and Design*, vol. 30, no. 3, pp. 921–925, 2009. 4.1

[31] Q. Guo, D. Li, S. Guo, H. Peng, and J. Hu, "The effect of deformation temperature on the microstructure evolution of Inconel 625 superalloy," *Journal of Nuclear Materials*, vol. 414, no. 3, pp. 440–450, 2011. [Online]. Available: http://dx.doi.org/10.1016/j.jnucmat.2011.05.029

[32] Y. C. Lin, D. X. Wen, J. Deng, G. Liu, and J. Chen, "Constitutive models for high-temperature flow behaviors of a Ni-based superalloy," *Materials and Design*, vol. 59, pp. 115–123, 2014. [Online]. Available: http://dx.doi.org/10.1016/j.matdes.2014.02.041

[33] Y. Wang, Q. Pan, Y. Song, C. Li, and Z. Li, "Hot deformation and processing maps of X-750 nickel-based superalloy," *Materials and Design*, vol. 51, pp. 154–160, 2013. [Online]. Available: http://dx.doi.org/10.1016/j.matdes.2013.03.081

[34] D. X. Wen, Y. C. Lin, H. B. Li, X. M. Chen, J. Deng, and L. T. Li, "Hot deformation behavior and processing map of a typical Ni-based superalloy," *Materials Science and Engineering A*, vol. 591, pp. 183–192, 2014. [Online]. Available: http://dx.doi.org/10.1016/j.msea.2013.09.049

[35] H. Zhang, K. Zhang, Z. Lu, C. Zhao, and X. Yang, "Hot deformation behavior and processing map of a γ'-hardened nickel-based superalloy," *Materials Science and Engineering A*, vol. 604, pp. 1–8, 2014. [Online]. Available: http://dx.doi.org/10.1016/j.msea.2014.03.015

[36] Q. Zuo, F. Liu, L. Wang, C. Chen, and Z. Zhang, "Prediction of hot deformation behavior in Ni-based alloy considering the effect of initial microstructure," *Progress in Natural Science: Materials International*, vol. 25, no. 1, pp. 66–77, 2015. 4.1, 4.3.2

[37] Y. Liu, R. Hu, J. Li, H. Kou, H. Li, H. Chang, and H. Fu, "Characterization of hot deformation behavior of Haynes 230 by using processing maps," *Journal of Materials Processing Technology*, vol. 209, no. 8, pp. 4020–4026, 2009. 4.1, 4.3.1, 4.3.2, 4.3.3

[38] M. Wang, W. Wang, Z. Liu, C. Sun, and L. Qian, "Hot workability integrating processing and activation energy maps of Inconel 740 superalloy," *Materials Today Communications*, vol. 14, no. December 2017, pp. 188–198, 2018. [Online]. Available: http://linkinghub.elsevier.com/retrieve/pii/S2352492817303264 4.1, 4.3.2

[39] J. J. D. Barbadillo, R. D. Gollihue, and B. A. Baker, "Nickel-Base Superalloys for Advanced Power Systems An Alloy Producer's Perspective John," *4th International Symposium - Supercritical CO2 Power Cycles*, pp. 1–15, 2014. [Online]. Available: http://www.swri.org/4org/d18/sCO2/papers2014/materials/03-deBarbadillo.pdf 4.1

[40] R. Viswanathan, J. F. Henry, J. Tanzosh, G. Stanko, J. Shingledecker, B. Vitalis, and R. Purgert, "U.S. Program on materials technology for ultra-supercritical coal power plants," *Journal of Materials Engineering and Performance*, vol. 22, no. 10, pp. 2904–2915, 2013. 4.1

[41] J. J. D. Barbadillo, R. D. Gollihue, and B. A. Baker, "Nickel-Base Superalloys for Advanced Power Systems An Alloy Producer's Perspective John," *4th International Symposium - Supercritical CO2 Power Cycles*, pp. 1–15,

2014. [Online]. Available: http://www.swri.org/4org/d18/sCO2/papers2014/materials/03-deBarbadillo.pdf 4.1

[42] R. L. Goetz and S. L. Semiatin, "The adiabatic correction factor for deformation heating during the uniaxial compression test," *Journal of Materials Engineering and Performance*, vol. 10, no. 6, pp. 710–717, 2001. 4.2, 4.2

[43] J. Castellanos, I. Rieiro, M. Carsí, J. Muñoz, M. El Mehtedi, and O. A. Ruano, "Analysis of adiabatic heating and its influence on the Garofalo equation parameters of a high nitrogen steel," *Materials Science and Engineering A*, vol. 517, no. 1-2, pp. 191–196, 2009. 4.2

[44] J. C. Zhao, M. Larsen, and V. Ravikumar, "Phase precipitation and time-temperature-transformation diagram of Hastelloy X," *Materials Science and Engineering A*, vol. 293, no. 1, pp. 112–119, 2000. 4.2, 4.3.2, 4.3.2, 4.3.2

[45] S. L. Semiatin and T. Altan, "MEASUREMENT AND INTERPRETATION OF FLOW STRESS DATA FOR THE SIMULATION OF METAL- FORMING PROCESSES," AIR FORCE RESEARCH LABORATORY MATERIALS AND MANUFACTURING DIRECTORATE, WRIGHT-PATTERSON AIR FORCE BASE, OH, Tech. Rep., 2010. 4.2, 4.3.1

[46] I. Haynes International, "HAYNES 230 alloy," Tech. Rep. 4.2

[47] ——, "Haynes 214 alloy," Tech. Rep. 765, 2010.

[48] Special Metals Corporation, "Inconel Alloy 740H," Tech. Rep., 2017. [Online]. Available: http://www.specialmetals.com/assets/smc/documents/alloys/inconel/inconel-alloy-740-h.pdf 4.2

[49] Y. Ma, F. Zhao, J. He, and J. Wang, "Correction of Flow Stress for Hot Compression of INCO718 Alloy," in *International Conference on Manufacturing Science and Engineering (ICMSE 2015)*, 2015, pp. 1431–1436. 4.2

[50] S. I. Oh, S. L. Semiatin, and J. J. Jonas, "An analysis of the isothermal hot compression test," *Metallurgical Transactions A*, vol. 23, no. 3, pp. 963–975, 1992. 4.2

[51] C. Devadas, D. Baragar, G. Ruddle, I. V. Samarasekera, and E. B. Hawbolt, "The thermal and metallurgical state of steel strip during hot rolling: Part II. Factors influencing rolling loads," *Metallurgical Transactions A*, vol. 22, no. 2, pp. 321–333, 1991. 4.2

[52] F. J. Humphreys, "Grain and subgrain characterisation by electron backscatter diffraction," *Journal of Materials Science*, vol. 36, no. 16, pp. 3833–3854, 2001. 4.3.1, 4.3.2

[53] T. Sakai, "Dynamic recrystallization microstructures under hot working conditions," *Journal of Materials Processing Technology*, vol. 53, no. 1-2, pp. 349–361, 1995. [Online]. Available: http://www.sciencedirect.com/science/article/pii/092401369501992N 4.3.1

[54] J. Wang, J. Dong, M. Zhang, and X. Xie, "Hot working characteristics of nickel-base superalloy 740H during compression," *Materials Science and Engineering A*, vol. 566, pp. 61–70, 2013. [Online]. Available: http://dx.doi.org/10.1016/j.msea.2012.12.077 4.3.1, 4.3.2, 4.3.2, 4.3.3

[55] Y. Liu, R. Hu, J. Li, H. Kou, H. Li, H. Chang, and H. Fu, "Deformation characteristics of as-received Haynes230 nickel base superalloy," *Materials Science and Engineering A*, vol. 497, no. 1-2, pp. 283–289, 2008. 4.3.1, 4.3.2, 4.3.3

[56] K. Mo, "Microstructural evolution and mechanical behavior in Ni-based alloys for very high temperature reactor," Ph.D. dissertation, 2011. 4.3.1

[57] J. P. Shingledecker, N. D. Evans, and G. M. Pharr, "Influences of composition and grain size on creep-rupture behavior of Inconel®alloy 740," *Materials Science and Engineering A*, vol. 578, pp. 277–286, 2013. [Online]. Available: http://dx.doi.org/10.1016/j.msea.2013.04.087 4.3.1

[58] Y. GUO, T. jiang LI, C. xia WANG, S. fang HOU, and B. han WANG, "Microstructure and phase precipitate behavior of Inconel 740H during aging," *Transactions of Nonferrous Metals Society of China (English Edition)*, vol. 26, no. 6, pp. 1598–1606, 2016. [Online]. Available: http://dx.doi.org/10.1016/S1003-6326(16)64266-8 4.3.1

[59] H. Tawancy, D. Klarstrom, and M. Rothman, "Development of a New Nickel-Base Superalloy," *JOM*, vol. 36, no. 9, pp. 58–62, 1983. 4.3.1

[60] L. Briottet, J. J. Jonas, and F. Montheillet, "A mechanical interpretation of the activation energy of high temperature deformation in two phase materials," *Acta Materialia*, vol. 44, no. 4, pp. 1665–1672, 1996. 4.3.2, 4.3.2

[61] H. J. McQueen and N. D. Ryan, "Constitutive analysis in hot working," *Materials Science and Engineering A*, vol. 322, no. 1-2, pp. 43–63, 2002.

[62] A. D. A. D. Rollett, G. S. Rohrer, and F. J. Humphreys, *Recrystallization and related annealing phenomena.* 4.3.2

[63] C. M. Sellars and W. J. M. Tegart, "Hot Workability," *International Metallurgical Reviews*, vol. 17, no. 1, pp. 1–24, 1972. [Online]. Available: http://www.tandfonline.com/doi/full/10.1179/imtlr.1972.17.1.1 4.3.2

[64] S. F. Medina and C. A. Hernandez, "General expression of the Zener-Hollomon parameter as a function of the chemical composition of low alloy and microalloyed steels," *Acta Materialia*, vol. 44, no. 1, pp. 137–148, 1996. 4.3.2

[65] S. S. Kumar, T. Raghu, P. P. Bhattacharjee, G. Appa Rao, and U. Borah, "Constitutive modeling for predicting peak stress characteristics during hot deformation of hot isostatically processed nickel-base superalloy," *Journal of Materials Science*, vol. 50, no. 19, pp. 6444–6456, 2015. 4.3.2, 4.3.2, 4.3.2

[66] H. Y. Li, Y. Liu, X. C. Lu, and X. J. Su, "Constitutive modeling for hot deformation behavior of ZA27 alloy," *Journal of Materials Science*, vol. 47, no. 14, pp. 5411–5418, 2012. 4.3.2

[67] Z. Bi, M. Zhang, J. Dong, K. Luo, and J. Wang, "A new prediction model of steady state stress based on the influence of the chemical composition for nickel-base superalloys," *Materials Science and Engineering A*, vol. 527, no. 16-17, pp. 4373–4382, 2010. [Online]. Available: http://dx.doi.org/10.1016/j.msea.2010.03.075 4.3.2

[68] C. Bruni, A. Forcellese, and F. Gabrielli, "Hot workability and models for flow stress of NIMONIC 115 Ni-base superalloy," *Journal of Materials Processing Technology*, vol. 125-126, pp. 242–247, 2002. 4.3.2

[69] S. C. Medeiros, W. G. Frazier, and Y. V. R. K. Prasad, "Hot deformation mechanisms in a powder metallurgy nickel-base superalloy IN 625," *Metallurgical and Materials Transactions A*, vol. 31, no. 9, pp. 2317–2325, 2000. 4.3.2, 4.3.3

[70] Y. Wu, M. Zhang, X. Xie, J. Dong, F. Lin, and S. Zhao, "Hot deformation characteristics and processing map analysis of a new designed nickel-based alloy for 700C A-USC power plant," *Journal of Alloys and Compounds*, vol. 656, pp. 119–131, 2016. [Online]. Available: http://dx.doi.org/10.1016/j.jallcom.2015.09.219 4.3.2

[71] M. Aghaie-Khafri and N. Golarzi, "Dynamic and metadynamic recrystallization of Hastelloy X superalloy," *Journal of Materials Science*, vol. 43, no. 10, pp. 3717–3724, 2008. 4.3.2

[72] M. Frommert and G. Gottstein, "Mechanical behavior and microstructure evolution during steady-state dynamic recrystallization in the austenitic steel 800H," *Materials Science and Engineering A*, vol. 506, no. 1-2, pp. 101–110, 2009. 4.3.2

[73] H. Monajati, M. Jahazi, S. Yue, and A. K. Taheri, "Deformation characteristics of isothermally forged UDIMET 720 nickel-base superalloy," *Metallurgical and Materials Transactions A*, vol. 36A, no. 4, pp. 895–905, 2005. 4.3.2

[74] H. Dehghan, S. M. Abbasi, A. Momeni, and A. Karimi Taheri, "On the constitutive modeling and microstructural evolution of hot compressed A286 iron-base superalloy," *Journal of Alloys and Compounds*, vol. 564, pp. 13–19, 2013. [Online]. Available: http://dx.doi.org/10.1016/j.jallcom.2013.01.156 4.3.2

[75] A. J. Brand, K. Karhausen, and R. Kopp, "Microstructural simulation of nickel base alloy Inconel 718 in production of turbine discs," *Materials Science and Technology*, vol. 12, no. 11, pp. 963–969, nov 1996. [Online]. Available: http://www.tandfonline.com/doi/full/10.1179/mst.1996.12.11.963 4.3.2

[76] A. R. Mashreghi, H. Monajatizadeh, M. Jahazi, and S. Yue, "High temperature deformation of nickel base superalloy Udimet 520," *Mater. Sci. Technol.*, vol. 20, no. 2, pp. 161–166, 2004. [Online]. Available: http://www.tandfonline.com/doi/full/10.1179/026708304225010343 4.3.2

[77] S. C. Medeiros, Y. V. Prasad, W. G. Frazier, and R. Srinivasan, "Microstructural modeling of metadynamic recrystallization in hot working of IN 718 superalloy," *Materials Science and Engineering A*, vol. 293, no. 1, pp. 198–207, 2000. 4.3.3

[78] L. Z. He, Q. Zheng, X. F. Sun, G. C. Hou, H. R. Guan, and Z. Q. Hu, "M23C6 precipitation behavior in a Ni-base superalloy M963," *Journal of Materials Science*, vol. 40, no. 11, pp. 2959–2964, 2005. 4.3.3

Chapter 5: Alloy development

DISCLAIMER:

This chapter presents excerpts from reports and work performed for an industrial sponsor. Therefore, all content within this chapter is considered proprietary and not for public distribution or further unauthorized use.

5.1 Abstract

The goal of the two-year alloy development effort was to design and fabricate one or more alloys specifically tailored to meet the requirements of the exponentially growing energy sector and its related market needs for sCO_2. In order to outline the state-of-the-art, a thorough literature study reviewed the general high temperature corrosion resistant alloys and advances made in the supercritical carbon dioxide (sCO_2) field. Various strengthening mechanisms, common to Ni-based alloys, have been identified, and the ones that met the sCO_2 requirements, were selected for the alloy development. Based on this, compositions for model alloys were established and first small batches were cast. Design and manufacturing of master alloys proceeded with larger batches and subsequent hot rolling. Integral to heat-treating, and to successfully obtain the desired final microstructures, were the homogenization and solution heat-treatments,

which were derived from thermodynamic and kinetic modeling. The results from thermo-mechanical testing, at various temperatures and strain rates, were an important part in ensuring that the final mechanical properties were met. Heat-treated and rolled alloy specimens were exposed to aging treatments in air, in order to study the microstructural response of the alloy. Subsequent characterization results were also used in the validation of simulated results for the precipitation behavior during aging. Finally, promising candidate alloys for the exposure in sCO_2 were successfully identified, based on extensive computational modeling, microstructural characterization, and thermo-mechanical testing. The model alloy selected, YGR01A, showed sufficient mechanical properties and corrosion resistance in preliminary studies. A reproducible alloy-manufacturing pathway was presented, which also focused on the scalability for commercial production.

5.2 Introduction

The material design approach was based on the metallurgical side of the most promising, commercially available Ni-based alloys, Haynes 214, Haynes 230 and Inconel 740H, their nominal composition is shown in Table 5.1. These alloys were selected based on their combination of high temperature strength and corrosion resistance, their room temperature yield strength, high temperature creep properties and age hardenability. Both alloying additions and thermo-mechanical processing, which are crucial steps in generating these properties, are considered in the design process for the novel alloys. Optimization is achieved by comparison and validation of designs

against existing physical metallurgy concepts for materials in high-temperature applications in corrosive environments.

Table 5.1: Nominal chemical composition of base alloys for alloy development, in wt-%

Alloy	Ni	Cr	Co	Mo	W	Nb	Ti	Al	Fe	C
Haynes 214	*	16						4.5	3.5	0.05
Haynes 230	*	22	5	2	14			0.3	3	0.1
Inconel 740H	*	25	20	0.5		2	1.8	0.9	0.7	0.03

Alloy	B	N	Y	Ta	Hf	La	Zr	Mn	Si
Haynes 214	0.01		0.01				0.02	0.2	0.1
Haynes 230	0.015					0.02		0.5	0.4
Inconel 740H								0.3	0.5

In order to provide a general introduction into Ni-based alloys and other alloys used for high temperature applications, an extensive review of the current state of research was performed. This focused on the basic metallurgy and the microstructural aspects of superalloys, while specific emphasis was put on alloys 214, Haynes 230 and Inconel 740H, which will be covered more in the following section. The literature review was then expanded into high temperature oxidation and its effects on superalloys, reviewing the thermodynamic-kinetic and microstructural processes and phenomena that are taking place at these conditions. The review of available concepts and designs allowed for the conception of 12 initially proposed model alloys. In an overview chart in Figure 5.1 the fundamental principles that guided the alloy design are presented, targeted for each alloy group.

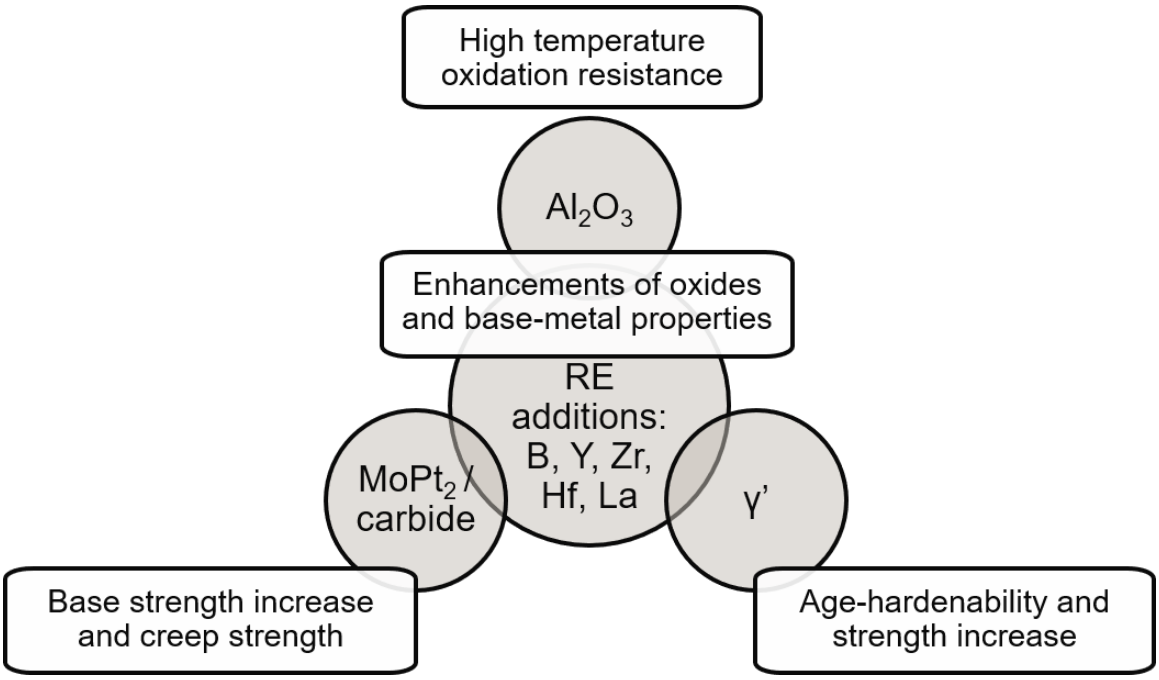

Figure 5.1: Schematic graph of alloy design principles.

5.3 General background on Haynes 230, Haynes 214 and Inconel 740H

Generally, when analyzing the property-microstructure relationships between established alloy systems for use in high-temperature environments under oxidizing and long-term exposure, only few can be considered. From comparison with other existing, commercially available alloys, studied for sCO_2 exposure, alloys Inconel 740H, Haynes 230 and Haynes 214 are amongst the best-performing [1]. The individual advantages of these alloys are outlined in the following paragraph. Inconel 740H gains its strength through age-hardenability by γ'-formation, good base-metal strength through the high

Co-content and creep rupture stability [2–4]. The advantages of Haynes 214 are its ability to form a protective Al_2O_3-scale for better high temperature stability and its creep resistance through the absence of any coarsening precipitates [5–7]. In Haynes 230, strength is inferred both by solid solution strengthening through alloying with W, Co and Mo, and by the formation of carbides, that prevent creep and grain growth [8, 9]. The advantages of these three alloys for high temperature use, over other commercially available alloys, can be seen by the maximum allowable stress in the ASME boiler and vessel code, in Figure 5.2, and in Figure 5.3, for the creep rupture strength for extended service times and temperatures.

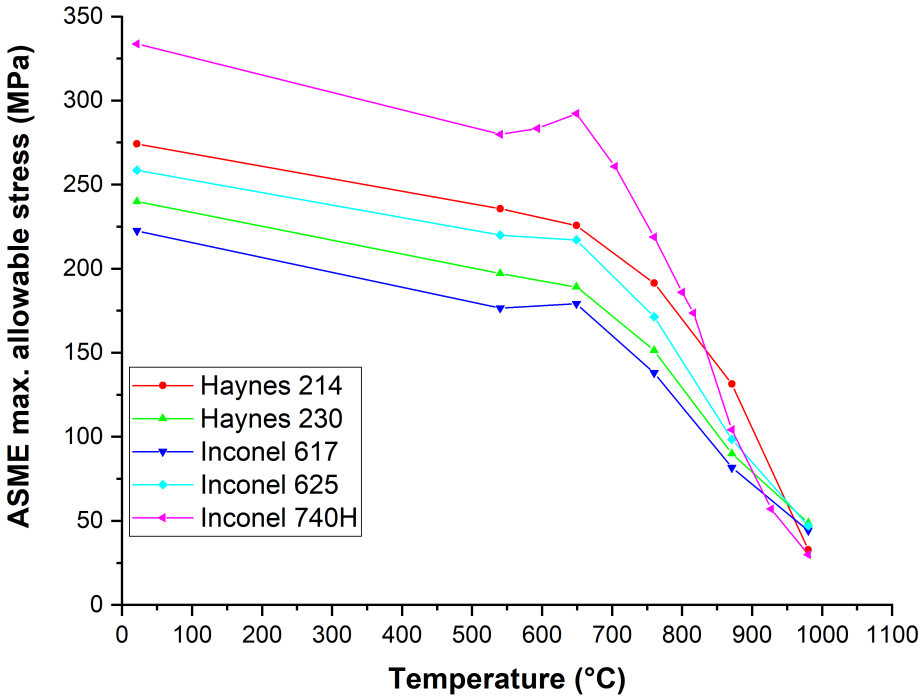

Figure 5.2: ASME boiler and vessel code approved materials with maximum allowable stress over process temperature.

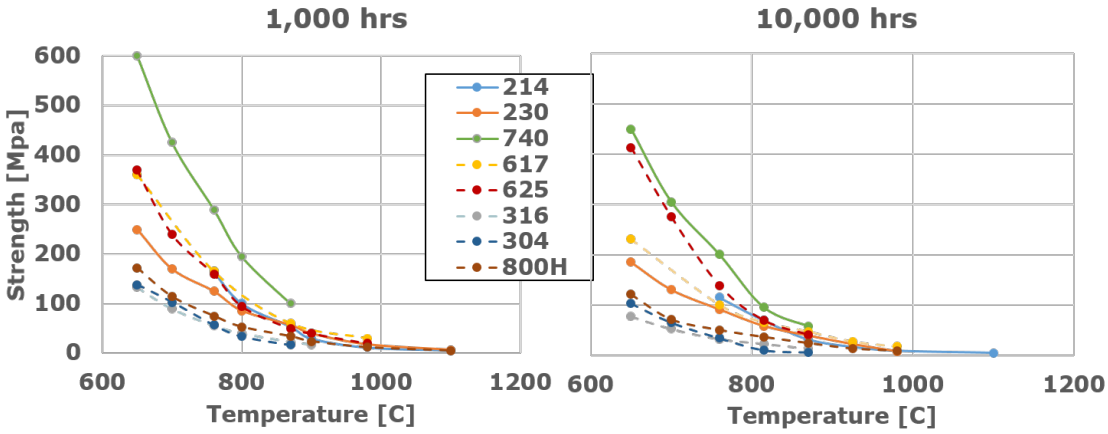

Figure 5.3: General creep rupture strength data for ASME boiler and vessel code approved materials.

There are several points that are important to mention when investigating the Ni-base alloys Haynes 214, Haynes 230 and Inconel 740H and their advantageous features. Haynes 214 is most prominently designed with regards to its ability to form the continuous Al_2O_3-scale, as mentioned previously [6]. Beyond that, as evident from an early developmental paper, traditional strengthening phases such as γ' are not desired due to a loss of ductility associated with it [7]. Therefore, Haynes 214 is designated as a non-heat-treatable alloy. While it shows an increase in tensile strength due to γ'-precipitation, during exposure in the γ'-stability range, the elongation is reduced by 50% [7, 10]. Due to these considerations, precipitation of γ' is controlled by elevated iron levels, which resulted in a decrease of the γ'-solvus temperature.

The main strengthening mechanism in Haynes 230 is normally only solid-solution strengthening, however it was found that it showed a large number of secondary phases during aging and elevated temperature exposure, which resulted in increased

strength at minimal loss to ductility [9, 11]. A range of different carbides were positively identified during general aging treatments [12]. In addition to carbides, the presence of a Pt_2Mo-type phase was confirmed, which has been linked to improved creep and strength properties in such alloys as Haynes 230, as well as Hastelloy X and Hastelloy C276 [11, 13–16]. From computational calculations, it was inferred that a stoichiometry of $Ni_2(Cr_{1-x}Mo_x)$ was most stable, with $x \leq 0.33$, avoiding the unstable and mechanically soft phase $Ni_2(Cr_{0.5}Mo_{0.5})$ [16]. Other phases which were predicted by thermodynamic modeling, such as μ-phase, σ-phase and M_23C_6, were also found, and also linked to the Ni_2(Cr,Mo)-phase, where the latter acts as a higher temperature transition phase [17, 18]. It should be noted, that despite reducing the elongation after precipitation during overaging, the μ, σ and M_23C_6 phases did not appear to have the same degree of detrimental effect on mechanical properties as observed in other alloys [19, 20].

The γ'-phase strengthened alloy Inconel 740H exhibits additional strengthening through the presence of carbide phases, similar to Haynes 230 [2–4]. The thermodynamically predicted σ-phase was not found in aging experiments by various researchers, raising the question of the mechanisms of its existence, and its thermodynamic stability range [3, 21]. Also, it was noted that the despite some coarsening of γ', Inconel 740H showed good creep-rupture strength stability between 700 ℃and 850 ℃[2]. This level of matrix strengthening was explained by the ability of dislocation pinning of the coarsened γ'-particles [22].

As exposure to sCO_2 presents an oxidizing environment, it is worthwhile to discuss the subject of high-temperature oxide scale systems. Emphasis will be put on the

different possible measures for oxidation resistance, along with stability of different oxide scales during high temperature exposure, an overview is presented in Figure 5.4 [1, 23–25]. It is apparent that Al_2O_3 presents a number of advantages over Cr_2O_3 and SiO_2. Majorly, these include improved scale adhesion and the absence of volatility, as Cr_2O_3 tends to form volatile CrO_3 above 800 °C. Further, Al_2O_3 shows higher stability than the other oxide phases, when water vapor is present [23].

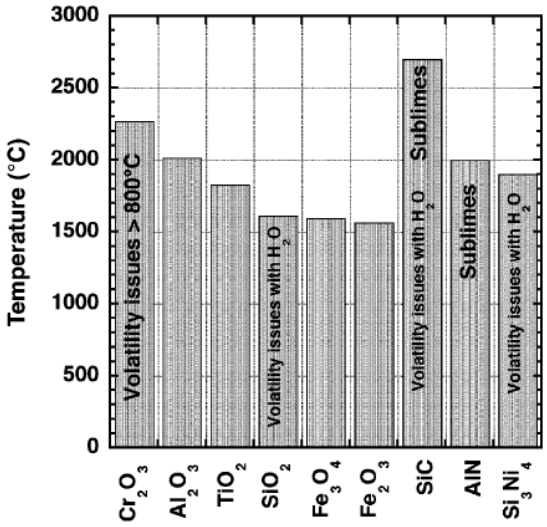

(a)

Oxide	Oxide–metal-volume ratio
K_2O	0.45
MgO	0.81
Na_2O	0.97
Al_2O_3	1.28
ThO_2	1.30
ZrO_2	1.56
Cu_2O	1.64
NiO	1.65
FeO (on α-Fe)	1.68
TiO_2	1.70–1.78
CoO	1.86
Cr_2O_3	2.07
Fe_3O_4 (on α-Fe)	2.10
Fe_2O_3 (on α-Fe)	2.14
Ta_2O_5	2.50
Nb_2O_5	2.68
V_2O_5	3.19
WO_3	3.30

(b)

Figure 5.4: a) Maximum-use temperature for various oxides used as protective coatings or scales (Pint, DiStefano, Wright, Oxidation resistance: One barrier to moving beyond Ni-base superalloys, 2006) and b) Oxide-metal ratios or Pilling-Bedworth-ratios for common oxides (Birks, Meier, Pettit, 2006).

Alloys that utilize these kind of scales, are for example the selected alloy Haynes 214. Its design is based on the early trials of Ni-Cr-Al alloys, including various additions of Reactive Element Effect [7, 26, 27]. The addition of Yttrium has been discussed specifically, finding that, along with Thorium, it tends to cause improved scale

adhesion of the Al_2O_3, while Yttrium had a tendency to form large YAG (Yttrium-Aluminium-Garnet) crystals during longer holding times. There has later been some controversy about the amount of Y necessary to provide optimum scale adhesion and prevent shorter stress-rupture times as well as the effective presence [5, 7, 27]. The issue of incipient melting and lowered creep properties by high levels of Yttrium, was found to be mitigated by limiting the amounts of alloyed Yttrium to 100 ppm or 0.01 wt-%.

Preferentially, Yttrium goes towards the grain boundaries of Al_2O_3 and exert its influence by controlling the oxide grain growth and inhibiting Oxygen diffusion [5]. A similar effect has been reported for the formation of Yttrium monolayers at the metal-oxide interface, where Yttrium prevents void formation and thus effectively controls the scale growth and promotes columnar growth [25, 28].

The role of other elements, such as Hf, Re, Pt and Ru has also been discussed, the effects of their addition to a Ni-Al system are shown in Figure 5.5 [23, 24]. It is clear, that all aforementioned elements, besides Hf and Pt, result in lower scale adhesion and spallation. However, Hf can also exert a similar beneficial influence, when its levels are controlled to be around 500-1000 ppm, i.e. 0.05 0.1 wt-%. In general, Hafnium behaves similar to Yttrium by forming an oxide and reducing the oxidation rate of NiAl. In the presence of C, Hf will also form carbides, which are more thermodynamically stable than carbides formed with any other alloying elements present in Haynes 214 [29]. It was suggested that the presence of Hf-carbides improves ductility, likely by promoting γ' formation on the grain boundaries.

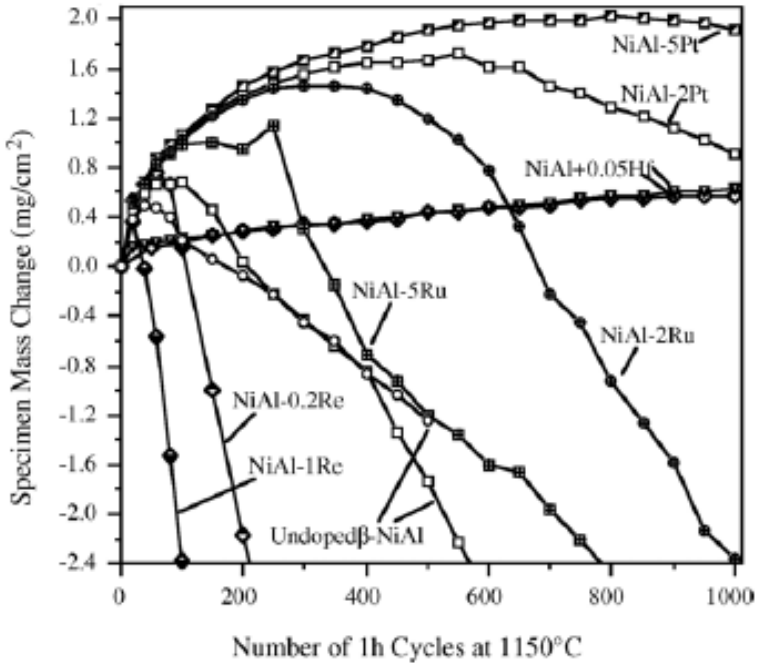

Figure 5.5: Mass change results for alloys of NiAl exposed to 1150 ℃ for increments of hundreds of hours [23]

5.4 Experimental methods

5.4.1 Small scale alloy manufacturing at OSU

Efforts have been undertaken to successfully melt and remelt various different trial alloys. Initial batches were made with commercially pure Ti as a getter element, in order to investigate O pickup during the process, since Ti has a much higher affinity to O than Ni, Cr, Co or Fe, illustrated by the Ellingham diagram for oxidizing conditions

[30]. It should be noted that these effects are partially mitigated by either a higher vacuum, i.e. less than 5 x 10^{-2} Torr, or 6 x 10^{-5} bar, or backfilling with an inert gas, such as Ar or N_2.

In a first round of trial melts, alloys with a composition closer to the target composition were chosen, that are readily available and tried for Vacuum Arc Remelt (VAR) systems. Inconel 625 and Inconel 718 were both extensively explored for their microstructural development and solidification behavior, see for example the dedicated Superalloys conferences [31, 32]. Commonly, the solidification reaction of these alloys ends with the formation of phases with low melting points, leading to the remaining liquid being enriched in alloying elements. These are often e.g., Nb-rich, such as the eutectic Laves-phases or carbide phases, e.g., MC type, where the latter is formed depended on any remaining, unbound carbon. In Figure 5.6 a starter charge for the VAR can be seen in the crucible in the chamber, along with the titanium button for oxygen gettering during the process. The starter charge consisted of a solid piece of either Haynes 230, Haynes 214 or Inconel 740H, depending on the specific model alloy. In order to achieve the target composition at 100g mass, the respective mass differences for each alloying element were calculated, and the pure element stock then added.

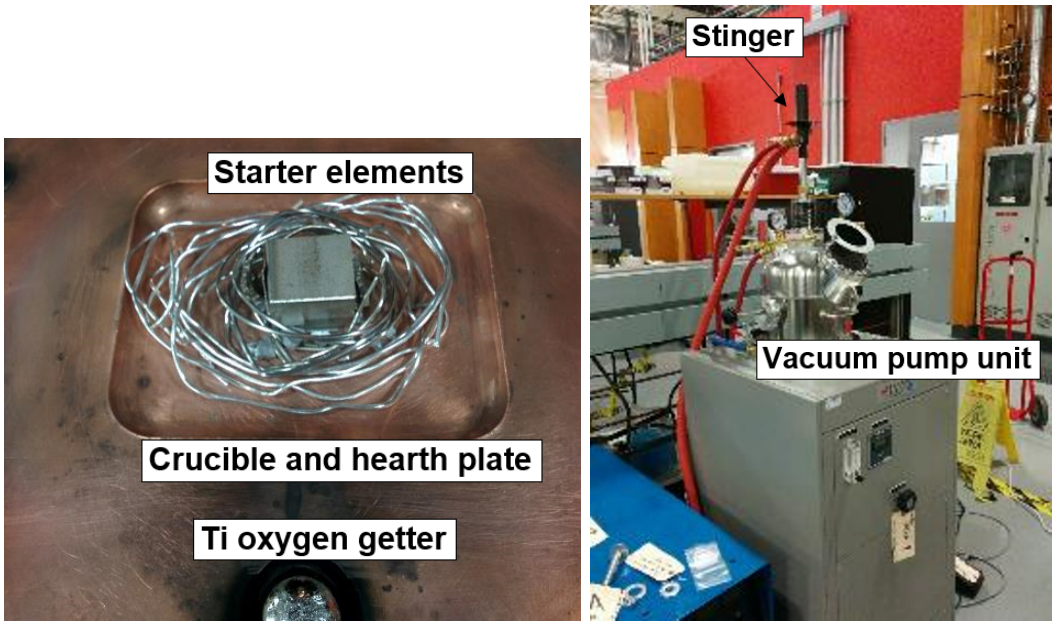

(a) (b)

Figure 5.6: a) Inside view of VAR system Centorr series 5BJ, showing the copper hearth plate and the tungsten-electrode, and b) outside view of the bell jar type furnace, with the stinger control, view-glass and pumping assemply.

The initial button melts produced in the VAR are shown in Figure 5.7, after the initial melt and a secondary remelt, which was performed to reduce the amount of oxidation and improve the cleanliness. However, in the end, all buttons were triple-remelted for optimal cleanliness. After the remelting process, the samples were cooled to room temperature in the chamber, in argon gas atmosphere to prevent any oxidation during cooldown. The melts were weighed and compared against the input weight to account for losses due to vaporization and gains due to oxidation and other contamination, seen in Table 5.2. In general, the noticed deviations are well within $\pm$ 1% of the target weight.

Figure 5.7: As-melted VAR buttons of YGR model alloys, in top row after initial melt in flowing Ar, and in bottom row, after secondary remelting.

Table 5.2: Mass statistics of VAR button of YGR alloys, before and after the melting process.

	YGR01A-1	YGR02A-1	YGR03A-1	YGR04A-1
Target weight [g]	100	100	100	100
Final weight [g]	100.077	99.656	101.315	100.569

5.4.2 Large scale manufacturing

During the production of wrought alloys, it is important to ensure a large enough melt size, assuming a desired minimum final plate thickness. Failure to do so can result in large forces during rolling that exceed the hot ductility at a given temperature and irreparably damage the workpiece. For this reason, large scale alloy making was employed, making ingots of at least 7-8 kg, with subsequent hot rolling.

After Vacuum Induction Melting (VIM)-casting of an ingot, an hydraulic press is used to reduce the initial ingot to a height suitable for the start of hot rolling, and to produce a first hot-worked microstructure. During subsequent hot-rolling, the height of the workpiece is further reduced in incremental steps, interrupted by reheating steps at constant temperature set points, in order to ensure a uniform material response throughout the rolling. All the processing steps are presented exemplary for alloy YGR01A in Table 5.3, which are generally applicable to all alloys made. The hot rolling stand used is presented in Figure 5.8, along with an exemplary image of an as-hot-rolled plate of YGR01A.

Table 5.3: Processing conditions for induction-melted YGR01A after hot forging, initial height and diameter 6.103 and 2.82, respectively, and constant reheat temperature of 1200 ℃.

Mill setting height [in]	Reheat time [min]	Reduction of area [%]
2	15	29
1.625	15	42
1.25	15	56
1.063	12	62
0.904	12	68
0.768	12	73
0.653	10	77
0.555	10	80
0.472	7	83
0.401	7	86

(Final dimensions [in]: 12 x 6 x 0.448)

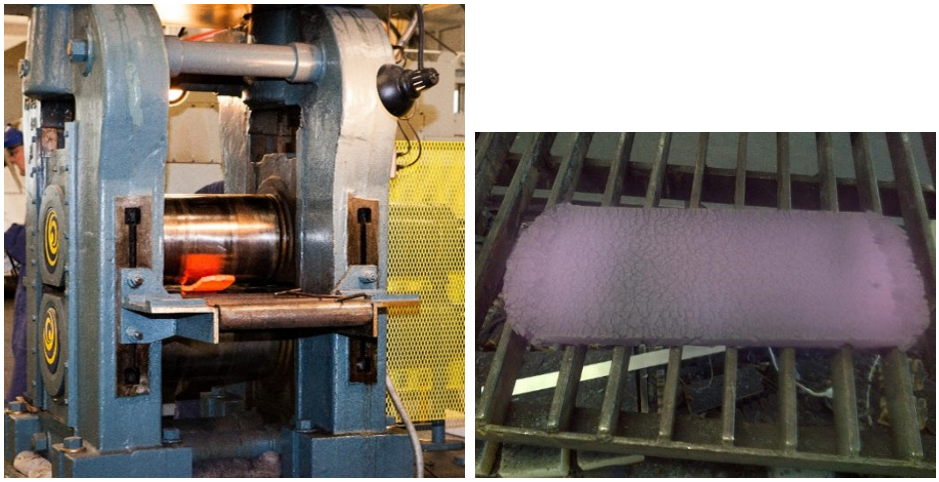

(a) (b)

Figure 5.8: a) Twin, reversed hot-rolling stand and b) image of as-hot-rolled plate of YGR01A.

5.4.3 Heat treatments based on Thermo-Calc/Dictra calculations

The melting of newly designed alloys necessitates an understanding of the solidification profile and segregation path of elements during the process. Physical characterization is one tool to investigate the final stages of these processes and to quantitatively and qualitatively assess the chemical segregation profiles and microstructures. However, it does not allow for understanding of the pathway or the processes that are leading up to this point. Thermodynamic modeling allows to study these processes and understand how additional heat treatments can mitigate these segregation profiles. Thermo-Calc ® and Dictra ® offer thermodynamic and kinetic modeling capabilities that address these topics well. For solidification reactions, Thermo-Calc uses a standard Scheil-Guliver approach [33], assuming infinite diffusion for all elements in the liquid phase and none in all solid phases. The optional backdiffusion in solid phases, for interstitial elements such as C, O, N, was not used in this case, as it provides a more conservative approach, closer to actual production environments [34]. For the Scheil calculations, a temperature step of ΔT of 5 ℃ was determined and the final fraction of liquid phase was set at 0.01. The Scheil simulations for the alloys YGR01A, YGR02A, YGR03A and YGR04A are shown in Figure 5.9. For comparison, the equilibrium results using a stepping calculation are shown in Figure 5.10 for the same four alloys.

The Scheil calculations further allow to assess the specific segregation of each element, to either the liquid or the solid matrix phase forming. For this approach, the elemental distribution in the solid is used, taking the composition of the first

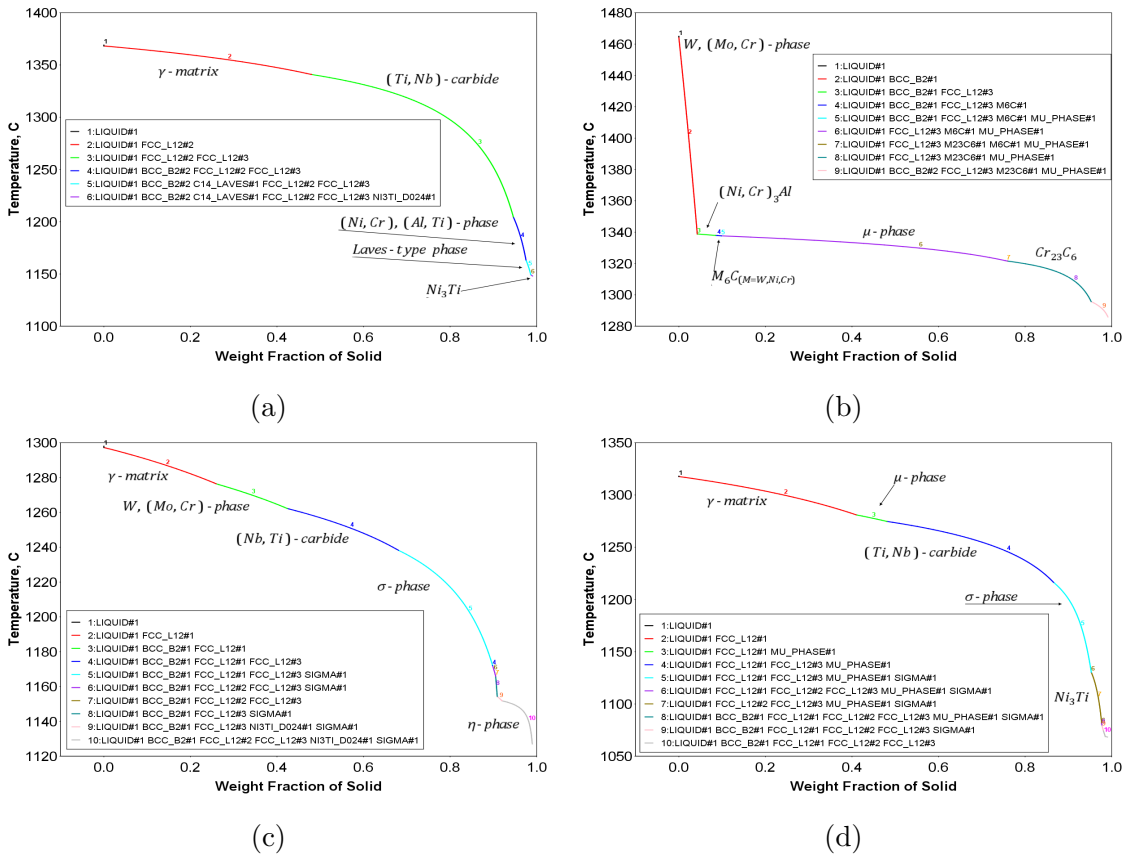

Figure 5.9: Scheil-Guliver solidification plots from ThermoCalc for alloys a) YGR01A, b) YGR02A, c) YGR03A and d) YGR04A

solid formed. Then the partition coefficient k can be defined as the composition of the solid over the composition of the liquid, $k = \frac{C_S}{C_L}$ [35]. This represents an idealized system, where k is linear and thus the liquidus and solidus lines are as well. Here, for the case of the first fraction solid formed, that is $f_s = 1\%$, the approximation can be made that c_L is close to the nominal composition.

The results are shown in Figure 5.11 for the four YGR alloys. The partition coefficient is larger than unity for elements that preferentially segregate towards the

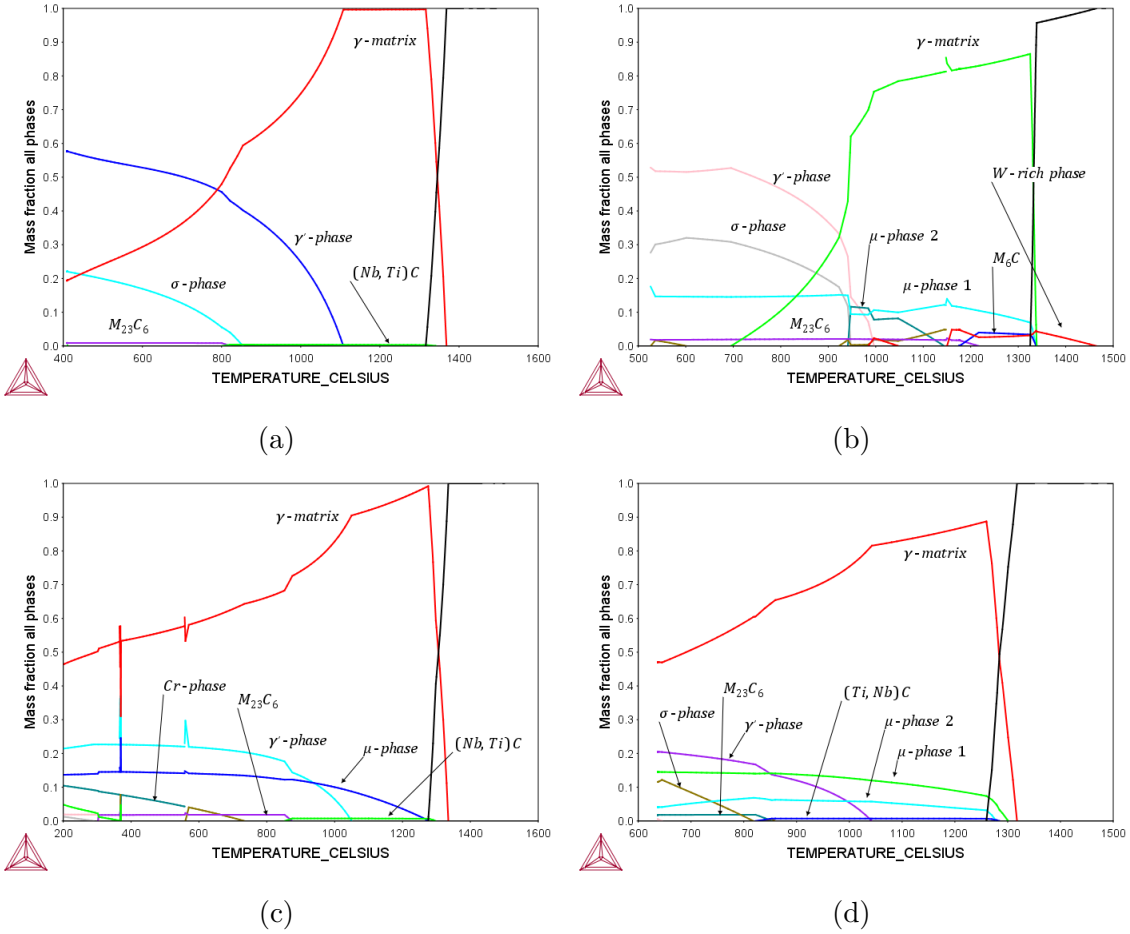

Figure 5.10: Equilibrium plots from ThermoCalc for alloys a) YGR01A, b) YGR02A, c) YGR03A and d) YGR04A

dendrite or first solid forming, and vice versa, if k is less than unity, elements preferentially segregate towards the interdendritic regions, or remain in the liquid. Further, it can be seen that the major alloying elements Ni, Cr, Co, Fe, and Al, to some degree, are all close to unity, suggesting very little tendency to segregate to either phase. However, Mo, W, and more so, Nb, Ti and C, are all segregating towards the interdendritic regions, thus are enriching in the liquid during the solidification progresses.

Both Mo and W are expected to form secondary phases early on, as indicated by the Scheil plots, while Ti and Nb are highly likely to precipitate out together with C, forming very stable carbide phases at high temperatures.

The segregation in Ni-base alloys can also be assessed along a line in between dendrites, this distance is also termed secondary dendrite arm spacing (SDAS). Using this distance as a length scale, a diffusion simulation can be performed, to evaluate the necessary time to equilibrate any slope or profile by following a heat-treatment. In the case of the alloys used here, a maximum deviation from the nominal composition of $\pm 1\%$ is targeted, along with an assumed SDAS of 50 μm, based on which the actual profiles were designed, seen in Figure 5.12. It can be seen that all heat treatments, which are involving increasing steps in temperature, also show an increase in homogenizing temperature, representative of the iterative nature of the simulation. Here, every homogenization procedure allows for a certain increase in maximum heat-treat temperature. This is due to an increase in incipient melting temperature caused by reducing local chemical gradients and gradually destabilizing higher-melting secondary phases.

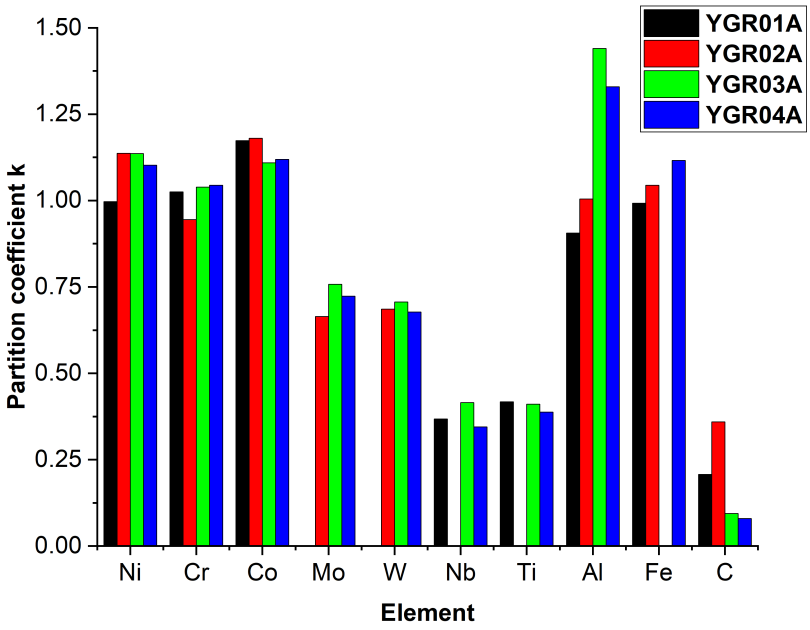

Figure 5.11: Partition coefficient as calculated by Scheil-module in ThermoCalc for all four YGR alloys.

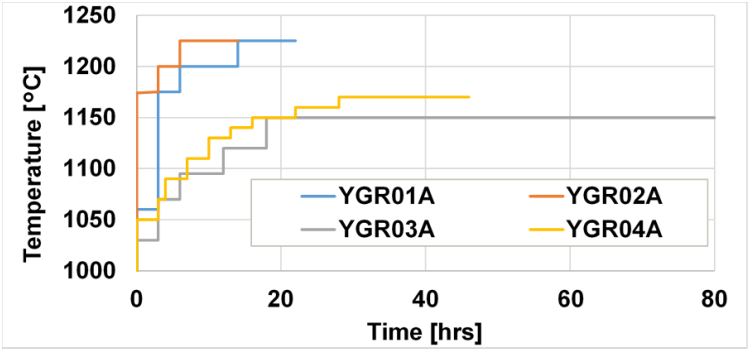

Figure 5.12: Simulated homogenization treatment schedules for YGR alloys based on Dictra calculations for homogenizing the segregation profile in SDAS of 50 μm to 1%.

5.5 Microstructural characterization of as-cast samples

After successful homogenization according to the heat-treatment plan, all buttons were cut into quarter sections, and then subsequently hot-mounted and polished to a 0.04 μm finish. Scanning electron microscopy was used to evaluate the microstructures after homogenization with regards to the dissolution of cast structures, any inhomogeneities, and chemical segregation. For YGR01-A in Figure 5.13, in a low magnification overview image, a high contrast setting in backscatter mode is used to highlight any remaining chemical variations across grains. Some segregation is still faintly visible, suggesting minor but negligible variations. At the same time, the up-close microstructure in the matrix contains few constituents, mainly inclusions, seen as black spheres in Figure 5.13a, which can be identified as SiO_2, Ti(C,N) and Al_2O_3. The matrix itself, shows, upon higher magnification, jagged, semi-cuboidal structures, which turned out to be γ', most likely secondary γ', assuming full dissolution during the homogenization cycle. The area fractions measured, for the amount of γ' present, were 19% at an average size of $0.15\mu m \pm 0.019\mu m$.

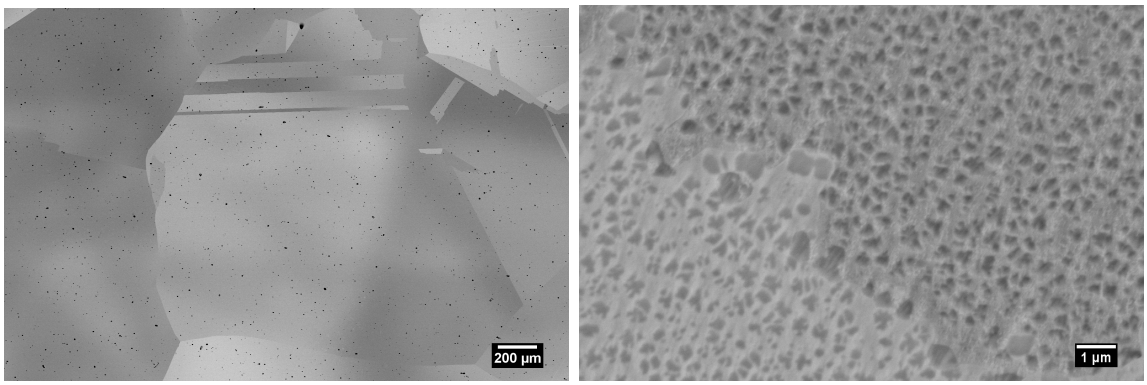

(a) (b)

Figure 5.13: Microstructure of YGR01A as homogenized showing a) high-contrast overview and b) the matrix background with γ' precipitates

Analysis of YGR02A showed a more complex microstructure after homogenization than YGR01A did, which is mostly owed to the increased amounts of transition-metal elements that are heavily segregating, Mo and W at 5 and 15 wt-%, respectively. At low magnifications, the general microstructure showed signs of directional solidification, with considerable remnants from the cast structure, in Figure 5.14a. The grains that have formed, as well as the prior dendrite boundaries, are lined with a nearly continuous network of phases, all appearing to be heavier than the matrix, based on their high-contrast response in backscatter mode. Upon higher resolution, in Figure 5.14b, the intragranular and intradendritic areas show precipitates of similar Z-contrast, which are uniformly distributed, sizes between $1 - 4\mu m$. Chemical analysis of these phases indicate that both types of precipitates are indeed similar in composition, suggesting a W-Ni-Cr-(Mo,Co) phase, which is found to be predicted by the earlier ThermoCalc simulations as a γ-phase type with a stoichiometry of $(Cr_{0.23}W_{0.26}Mo_{0.15})(Ni_{0.25}Co_{0.05})$. Based on equilibrium and Scheil-Guliver calcula-

tions, this phase is predicted to precipitate out of the liquid and have stability close to the Liquidus temperature. Its area size fraction was calculated to be 9.44%.

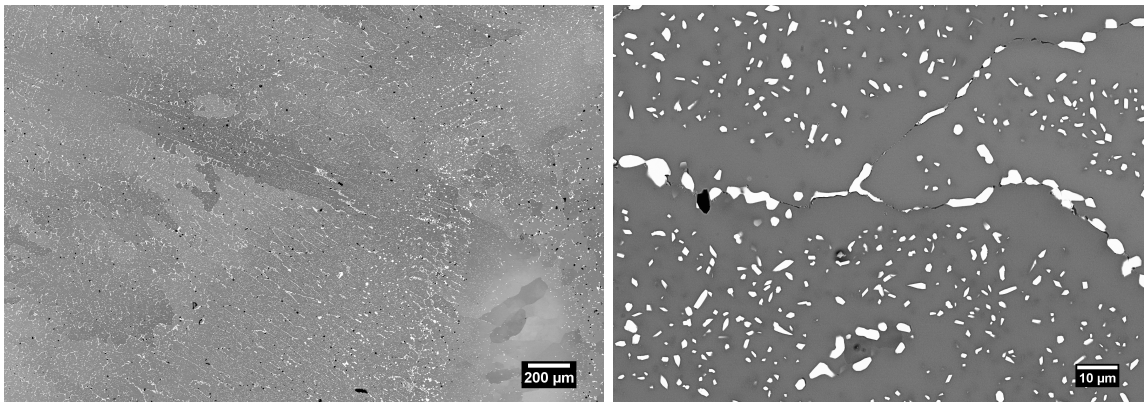

(a) (b)

Figure 5.14: Microstructure of YGR02A as homogenized showing a) general matrix overview and b) the grain structure and the matrix background with precipitate phases

The alloy YGR03A shows an even more segregated microstructure, resembling more an as-cast structure, Figure 5.15a. The high-contrast backscatter mode highlights the stronger chemical gradient as well as the interfaces between the prior dendrites, which are still showing significant remnants of the dendrite branches and interdendritic spaces. This can be seen in more detail in Figure 5.15b, where the secondary phases, which precipitated out of the melt, are also apparent. In contrast to YGR02A, YGR03A has Ti and Nb added, more Cr and less Al, giving a Ti/Al-ratio of 2:1, favoring stable γ'-formation. This prevented the formation of the same α-W network, and instead favored a similarly shaped extensive network of precipitate phases, that

were identified as μ-phases of the $(Cr_{0.45}Mo_{0.08}W_{0.1})(Ni_{0.3}Co_{0.06})$ kind. The second phase, appearing white and more evenly distributed in the background, appears to be another kind of μ-phase, resembling the one found in YGR02-A, adjusted for the higher Cr amounts and the reduced amounts of transition metal elements available. The stoichiometry found is rather shifted towards $(Cr_{0.3}Mo_{0.11}W_{0.21})(Ni_{0.27}Co_{0.07})$. The average size fraction for the larger grey μ-phase was estimated at 12.6% with an average size 42.663 μm^2, and the smaller white phase at 4.5% with an average size of 1.477 μm^2.

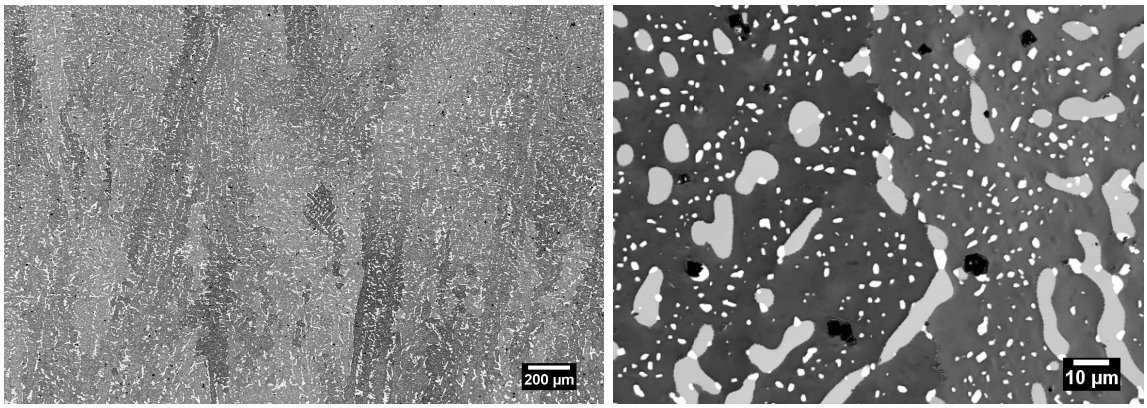

(a) (b)

Figure 5.15: Microstructure of YGR03A as homogenized showing a) the grain and dendritic structure and b) the boundary between two prior dendrites.

Lastly, YGR04A presents a similar microstructure to YGR03A, as remnants of the cast structure are still present and the prior dendrites and dendrite arms are still faintly visible, see Figure 5.16a. Boundaries are visible between dendrite cores and interdendritic areas, as well as newly formed grains, where there is a network of

discontinuous phases, which resembles YGR02A more than YGR03A. This phase appears grey in constrast and has the composition $(Cr_{0.45}Mo_{0.08}W_{0.1})(Ni_{0.3}Co_{0.06})$, which is similar to the first μ-phase found in YGR03A. The difference between both μ-type phases can be explained by the shifted Co/W-ratios between both alloys, with YGR04A having a 1:1 ratio, while YGR03A has a ratio of 1:3. In YGR04A, these phases are present at roughly 2% with an average size of 19.041 μm^2. There is also a finer, more uniformly distributed white phase within the prior dendrite area that can also be identified as μ-phase with the stoichiometry $(Cr_{0.29}Mo_{0.11}W_{0.2})(Ni_{0.24}Co_{0.11})$, which is similar to the comparable high-W μ-phase found in YGR03-A. Its size fraction is estimated at 3.767% with an average size of 1.21 μm^2.

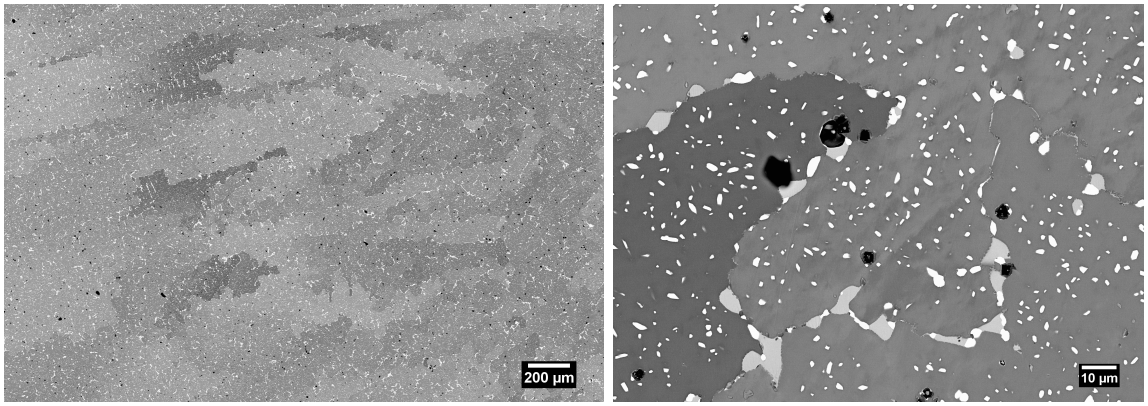

(a) (b)

Figure 5.16: Microstructure of YGR04A as homogenized showing a) the grain and dendritic structure and b) boundary microstructures.

5.5.1 Discussion

From the measurements taken in the as-homogenized condition, seen in Table 5.4, it is clear that there are strong influences of the base chemistry of the model alloys on the chemical homogeneity and stability of the precipitated phases. The existence of these phases is somewhat contradicting a successful homogenization treatment, usually designed to eliminate these types of phases. The microstructure is more resembling the Scheil than the equilibrium phases predicted by ThermoCalc calculations, as well as the comparable microstructures found in as-cast Ni-base alloys of similar composition.

The likely cause for the deviation is the fact that no quenching but mere furnace cool was performed after homogenization, allowing secondary phases to form during the cooling process. Additional heat treatments of these structures could lead to further exacerbated segregation phenomena by uphill-diffusion enhanced formation of low-melting Ni-Mo eutectics, for example, as seen by Ru et al. [36] or Hegde et al. [37]. Some of this can be attributed to stepwise increase of temperature in the field between solvus and solidus, while a gradual temperature increase from solvus to final temperature appeared more beneficial.

Comparison with literature data gives a general visual and chemical agreement of some of the putative μ-phases found with Cr-rich transition phases in Haynes 230 [11], or μ-phases and carbide phases in Hastelloy X, Hastelloy C-276 or Hastelloy C-22 [13, 17, 18]. One of the main issues in phase detection using SEM-EDX, is the inability to quantitatively, and often times, even qualitatively, detect carbon. However, the carbide phases, such as $M_{23}C_6$ and M_6C, often have very similar chemical

compositions to the Topologically Close-Packed (TCP) phases μ and σ, which are prone to precipitate in alloys with high Mo and W contents [38, 39]. In order to distinguish and characterize these phases successfully, it is necessary to use diffraction techniques, e.g. by SAED in TEM or high resolution XRD. Similarly, chemical microanalysis, which can account for C, would need to be more sophisticated, this could be EDX in thinned specimens for TEM use, or Electron Energy Loss Spectroscopy (EELS), being more sensitive to low-Z elements. Further, heat treatment operations such as solution treatment and aging treatment cycles are necessary for understanding of precipitation reactions. This would allow a supersaturation of the matrix with the elements that are forming some of the desired secondary phases, such as W, Cr, Mo, and Co. Subjecting these samples to specific time-temperature cycles, following both the equilibrium phase diagram considerations as well as kinetic and diffusion model-based designs, would then cause desired precipitation.

Table 5.4: Comparison of chemical compositions of different secondary phases found in model alloys and comparable secondary TCP-type phases in commercial alloys.

Phase [at-%]	Cr	Ni	W	Co	Mo
μ_I (YGR03A, -04A)	45	26-30	9-10	6-10	7-9
μ_{II} (YGR03A, -04A)	29-30	24-27	20-21	7-11	11
μ_{III} (YGR02A)	23	25	26	5	15
Transition phase in Haynes 230 [11]	46.93-47.35	38.53-41.48	9.27-10.3		1.9-4.24
μ or M_6C in C-22 [13]	24.73	53.16			22.11
μ in C-276 [17]	16.19	36.51	3.12	1.95	49.5
M_6C in C-276 [17]	20.83	34.84	2.06	1.93	37.49
σ in alloy 800 [40]	54	22	5	12	6

5.6 Microstructural characterization of as-wrought samples

The general microstructural makeup, grain size and evolution of the γ'-phase were analyzed for the as-wrought, aged, and solution treated specimens. The goal for the solution treatment was to assess whether an additional heat-treatment after hot-working would have significant impact on the microstructure and, further, on the mechanical properties. The same goals applied to the aging treatment, but in addition, the γ'-coarsening behavior was investigated, and compared with the as-wrought and solution-treated samples. The aging treatment was conducted at 700 ℃ for 200 h in ambient still air in a Leco tube furnace, followed by air-cooling. Temperature control was performed with a type-K thermocouple. The temperature was in congruence with sCO_2 test temperatures. The solution treatment was conducted at 1150 ℃ for 15 min in still air in a Thermcraft box furnace, followed by air-cooling. Temperature control was performed with a two type-R thermocouples as part of an integrated PID loop for accurate temperature control. All heat-treated samples were hot-mounted in conductive resin and mechanically ground and polished to 0.04 μm surface finish, followed by ultrasonic cleaning in methanol. Surface characterization was performed using a Zeiss Sigma SEM at 15 kV, using secondary electron (SE) and backscatter electron (BSE) detectors, while chemical microanalysis was performed using an Oxford Instruments EDS detector. Statistical image analysis on SEM images for particle and grain size analysis was performed using ImageJ2.

The phase diagram calculated for YGR01A, with Thermo-Calc ® 2017a, using the TCNi7 database, is shown in Figure 5.10a. It suggests that after successful

homogenization and solution heat-treatment, all secondary phases except the MC-type carbide should be in solution. For comparison, the expected phases that occur during solidification are presented in Figure 5.9a. In the case of the as-wrought specimens, it was assumed that while the Laves and BCC-type phase dissolved during hot-working some of γ'-phase may still be present due to the slow cooling of the final plate material. Since the phase stability for the γ'-phase ends at around 1100 ℃, the solution treatment temperature was set at 1150 ℃, with a holding time of 15 min, in order to minimize excessive grain growth. These modeling results were compared with the characterization results for the as-wrought, solution-treated and aged specimens. The matrix overview images for all samples, taken in SEM-BSE mode, are shown in Figure 5.17. In general, all three conditions showed a similar microstructure, with large austenite grains, and two obvious phases present. These were a white, irregularly-shaped phase, identified as Nb-carbide, and, less commonly, a black, blocky phase, found to be Ti-Nb-carbides. Further, upon higher magnification, for all three conditions, uniformly distributed γ'-phase was found. The statistical image analysis, seen in Table 5.5, showed that the solution treatment was effective in starting to dissolve the γ'-phase, but required additional time to complete the process. The average matrix grain size notably decreased during the solution treatment. This can be attributed to both short holding times, where large grain growth could be minimized, and recrystallization effects that allowed for smaller grains to nucleate and grow. The aging treatment, in turn, showed no significant effect on the γ' average size, while slightly increasing its volume fraction.

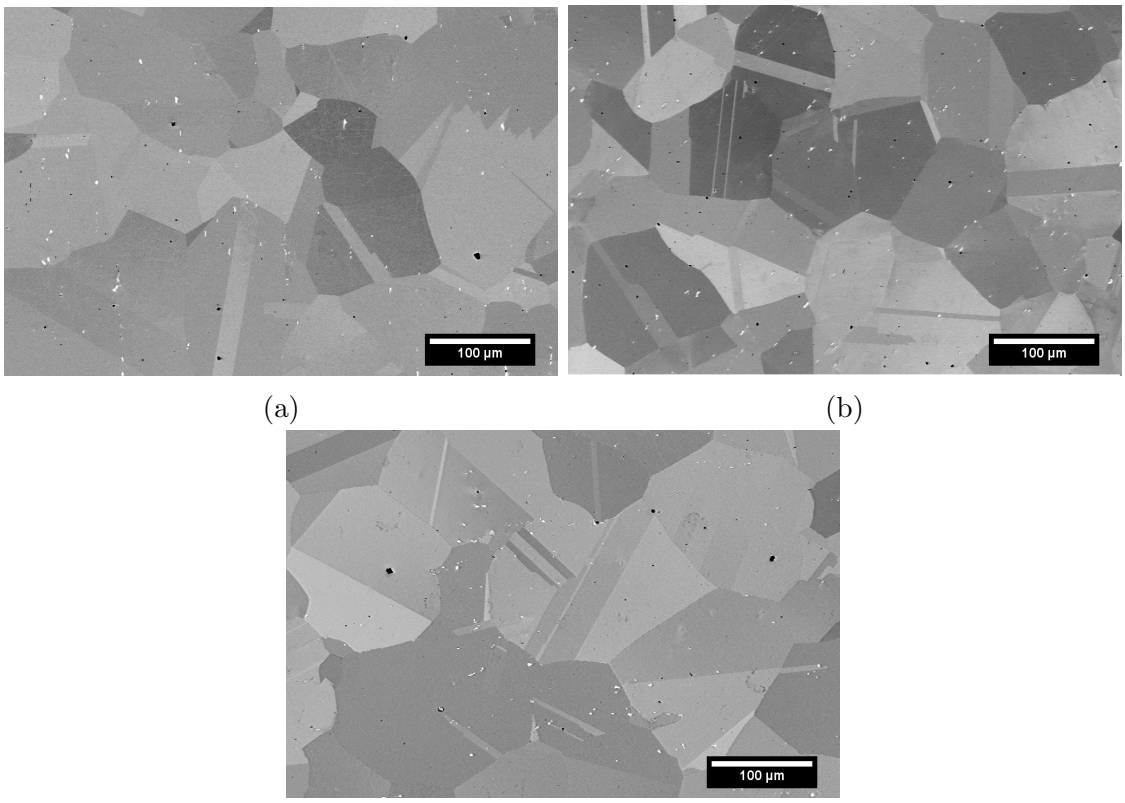

(a) (b)

(c)

Figure 5.17: SEM-BSE images of cross-sections of YGR01A showing the general matrix for a) as-wrought, b) solution-treated and c) aged specimens.

Table 5.5: Results of statistical image analysis on YGR01A samples based on SEM overview images of matrix.

Sample	γ' vol.fraction [%]	γ' avg. size [nm]	Grain size avg. [μm]	Grain size SD [μm]
As-wrought	15	75	115	45
ST	13	30	75	33
As-wrought and aged	20	75	87	51

The effect of the aging treatment on the average γ' size was compared to the thermodynamic modeling results of YGR01A, based on the measured matrix grain size of the as-wrought specimens. In Figure 5.18a, the coarsening behavior of YGR01A has been modelled in JmatPro 6.0 ® and plotted against time for a range of temperatures. Comparing with the curve for 75 ℃, the measured results show good agreement, as negligible growth is predicted for all temperatures below 750-800 ℃. The general precipitation behavior of γ' was also modelled in a Time-Temperature-Transformation (TTT) diagram in Figure 5.18b. Here, the thermodynamically stable phases are modeled for a wide temperature range, taking kinetic influences into account, based on holding time and temperature. It can be seen that the σ-phase, as predicted from equilibrium calculations, is not expected to form for more than 130 h, when holding at 700 ℃. At the same time, γ' is predicted to form after only 47 min at temperature. Indeed, high-resolution BSE images of the aged specimen show γ' precipitation at the grain boundaries, seen in Figure 5.19. Chemical analysis using EDS suggests substantial Cr enrichment and depletion of Ni, and minor enrichment for all other alloying elements. While more precise chemical and crystallographic analysis will be required to identify this phase, they are expected to be the predicted σ-phase.

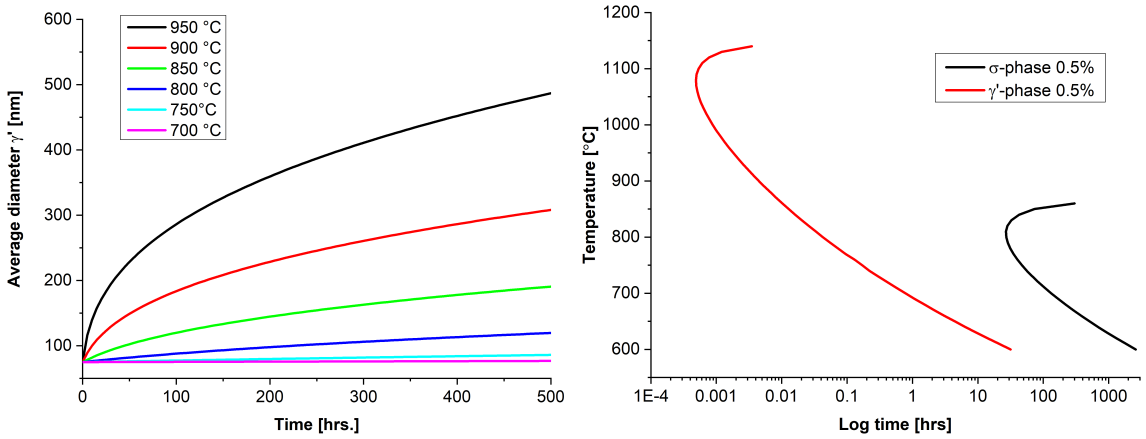

(a) (b)

Figure 5.18: a) Coarsening plot for γ'-phase in YGR01A and b) TTT diagram for YGR01A as modeled by JmatPro 6.0 ®.

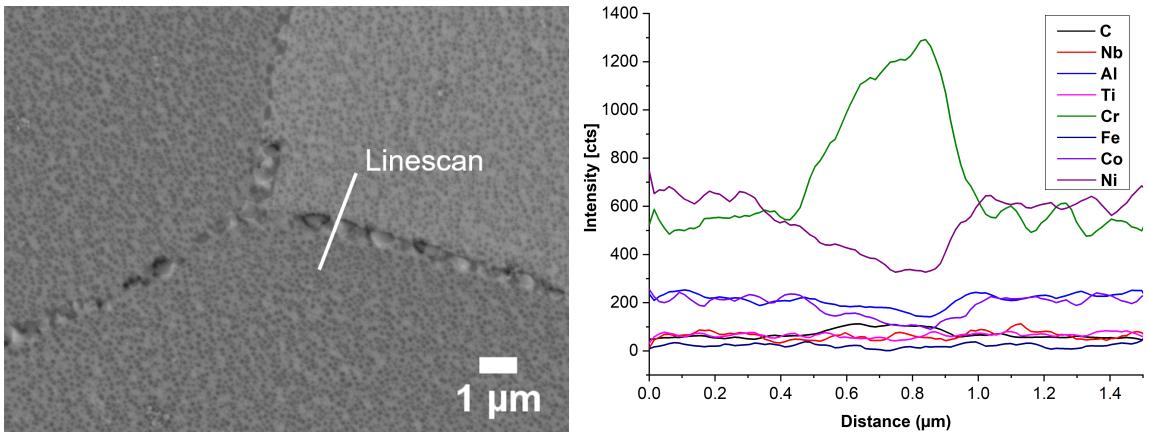

(a) (b)

Figure 5.19: a) High-resolution BSE image of triple grain boundary of aged YGR01A, showing precipitation at the grain boundary and b) EDS linescan across grain boundary as indicated in a).

5.7 Characterization of mechanical properties

Thermo-mechanical testing in a Gleeble 3500 ® unit was performed to study the response of the as-wrought alloy YGR01A to hot-deformation processing conditions, as seen during manufacturing of final shapes, such as heat-exchanger coils and tubes. The temperature ranges selected were similar to the hot-working temperatures the alloy would experience during initial hot-rolling. Using hot compression testing, the influence of different strain rates and temperatures for a true strain of 0.7 is analyzed, as well as the effect of prior additional solution treatment. The strain rates used are, 1.0/s and 0.1/s, for temperatures between 900 ℃ and 1200 ℃ in 50 ℃ increments. Comparisons are made between the different testing conditions and with modeling results for flow-stress using JmatPro 6.0 ®.

In Figure 5.20 the flow-stress results for YGR01A in the as-wrought and solution-treated conditions are shown. Notably, the results for 900 ℃ are missing, which is due to severe, complete fracturing and material degradation at this temperature, for all strain rates and heat-treat conditions. As temperatures increase, the cracking susceptibility decreased, while samples exposed at 1000 ℃ all fractured, which occurred for both heat-treat conditions, at around the same true strain of $\varepsilon = 0.45$. However, from temperatures of 1050 ℃ and higher, no fracturing or cracking was observed. Beyond that, all samples show rather common flow stress behavior for austenitic alloys with low stacking fault energies. This is indicated here by a strong yield-point-temperature dependence and relatively low temperature-strain hardening dependence. Further, the characteristic onset of dynamic recrystallization is visible,

indicated by a peak in the flow stress before the strain hardening becomes negative and the curve drops. This is evidently more notable for the as-wrought samples than for the solution-treated ones, e.g. at 1050 ℃ and 1000 ℃. The reason can be, that the microstructure after hot-rolling retained some inhomogeneities or phases, which did not dissolve or even precipitated during hot-rolling. These then can become nucleation sites for an earlier, more pronounced onset of dynamic recrystallization. This is also likely the reason for a generally higher flow stress for the as-wrought samples. The larger average γ' size, as compared to the solution-treated samples, is likely to increase flow-stress as well.

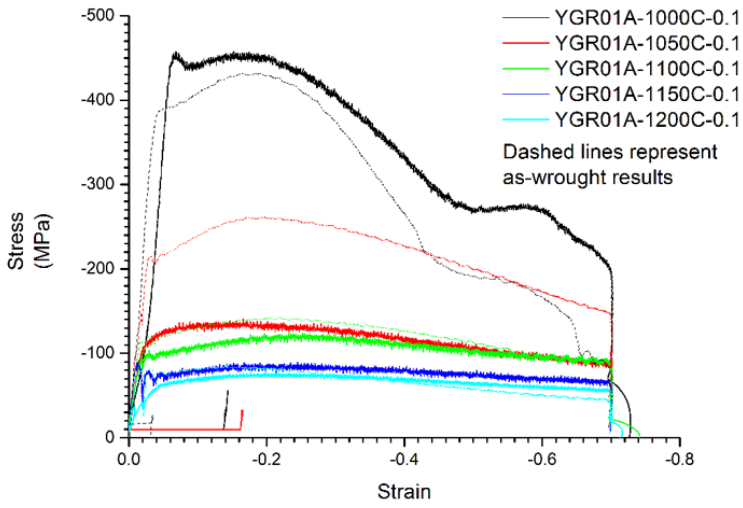

Figure 5.20: True stress true strain plot of YGR01A for as-wrought and solution-treated results for different temperatures.

The influence of the different strain rates of 0.1/s and 1.0/s is shown in Figure 5.21. The stress-strain curves show generally comparable strain hardening behavior

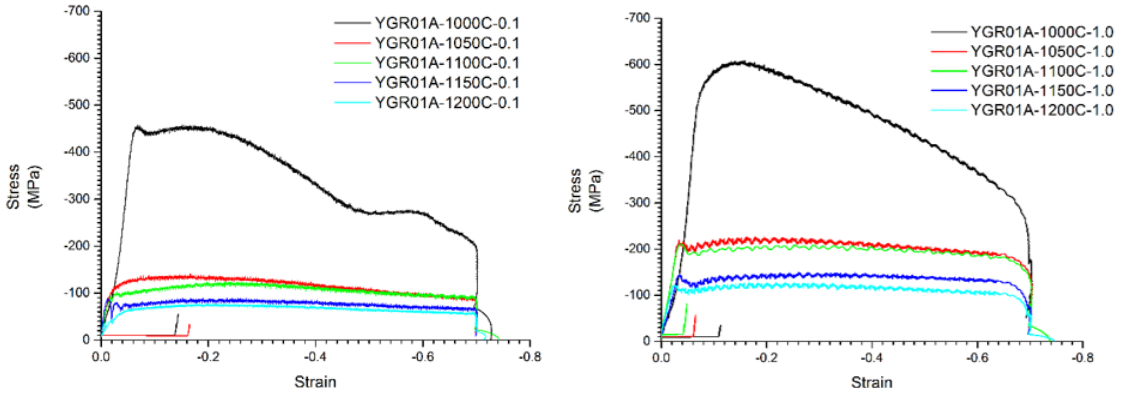

(a) (b)

Figure 5.21: True stress true strain plot of YGR01A for strain rates of a) 0.1/s and b) 1.0/s, both in solution-treated condition results for different temperatures

between the two strain rates. Notable differences are the overall flow stress values, which are in all cases higher for the faster strain rate of 1.0/s. Below 1000 ℃, the flow-stress values are twice as high as at the lower strain rate. At the same time, the relative difference between the flow-stress levels for the different temperatures appeared the same for both strain rates. Further, it is noteworthy, that the sample at 1000 ℃ for the strain rate of 1.0/s did not show fracturing during the upset or in the stress-strain curve, but the sample did show circumferential cracking after cooling. Comparison with thermodynamic modeling data from JmatPro 6.0 ® for flow stress, based on calculations for the solution-treated matrix grain size, is presented in Figure 5.22. Generally, for both strain rates, there is a large deviation between the calculated and the experimental results, especially for temperatures below 1050 ℃. At lower temperatures, the agreement between the datasets improves, while the calculated

results still not reflect the different strain hardening behaviors or events like dynamic recrystallization.

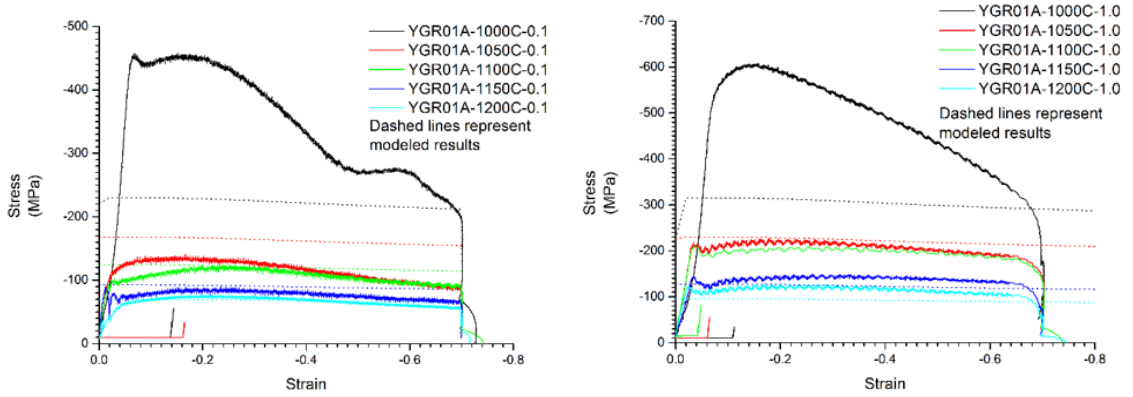

(a) (b)

Figure 5.22: True stress true strain plot of YGR01A compared with calculated flow stress results from JmatPro 6.0 ® for strain rates of a) 0.1/s and b) 1.0/s, both in solution-treated condition results for different temperatures

5.8 Conclusions

A development approach for model alloys intended for sCO_2 use was presented. The process started with a novel alloy design approach, which was based upon the commercially available base alloys Haynes 214, Haynes 230 and Inconel 740H. The most advantageous features of each base alloy were defined and incorporated in the alloy design. Thermodynamic modeling of the new compositions showed the stable phases, and, together with solidification models, heat-treatment schedules could be defined. Initial small-scale melting was performed, and the subsequent analysis informed downselection process, from four initial alloys to the final one, YGR01A. The successful hot-rolling of a larger melt of this alloy proved some early scalability and processing feasibility. Samples taken from the hot-rolled stock were utilized for the optimization of aging treatments, and to showcase microstructural homogeneity after solutionizing. The hot-working behavior of as-hot-rolled material was investigated and the preferred hot-working ranges for subsequent forming operations were clearly defined.

5.9 Bibliography

[1] B. Pint, R. Brese, and J. Keiser, "Effect of pressure on supercritical CO 2 compatibility of structural alloys at 750 C," *Mater. Corros.*, vol. 68, no. 2, pp. 151–158, feb 2017. [Online]. Available: http://doi.wiley.com/10.1002/maco.201508783 5.3, 5.3

[2] S. Zhao, F. Lin, R. Fu, C. Chi, and X. Xie, "Microstructure evolution and precipitates stability in 740H during creep," in *Adv. Mater. Technol. Foss. Power Plants*, 2013. 5.3, 5.3

[3] J. J. D. Barbadillo, R. D. Gollihue, and B. A. Baker, "Nickel-Base Superalloys for Advanced Power Systems An Alloy Producer's Perspective John," *4th Int. Symp. - Supercrit. CO2 Power Cycles*, pp. 1–15, 2014. [Online]. Available: http://www.swri.org/4org/d18/sCO2/papers2014/materials/03-deBarbadillo.pdf 5.3

[4] C. J. Cowen, P. E. Danielson, and P. D. Jablonski, "The microstructural evolution of inconel alloy 740 during solution treatment, aging, and exposure at 760C," *J. Mater. Eng. Perform.*, vol. 20, no. 6, pp. 1078–1083, 2011. 5.3, 5.3

[5] H. M. Tawancy, "On the Role of Yttrium during High-Temperature Oxidation of an Ni-Cr-AI-Fe-Y Alloy," *Metall. Mater. Trans. A*, vol. 22, no. JUNE, pp. 1463–1465, 1991. 5.3, 5.3

[6] I. Haynes® International, "HAYNES 214 alloy," Tech. Rep. 765, 2010. 5.3

[7] R. B. Herchenroeder, G. Y. Lai, and K. V. Rao, "A New, Wrought, Heat-Resistant Ni-Cr-Al-Fe-Y Alloy," *J. Met.*, no. November, pp. 16–22, 1983. 5.3, 5.3, 5.3

[8] I. Haynes® International, "HAYNES ® 230 ® alloy," Tech. Rep. 5.3

[9] J. Veverkova, A. Strang, G. R. Marchant, G. M. Mccolvin, and H. V. Atkinson, "High Temperature Microstructural Degradation of Haynes Alloy 230," *Superalloys*, pp. 479–488, 2008. [Online]. Available: http://www.tms.org/superalloys/10.7449/2008/Superalloys{_}2008{_}479{_}488.pdf 5.3, 5.3

[10] M. Agilan, T. Venkateswaran, D. Sivakumar, and B. Pant, "Effect of post weld heat treatment on mechanical properties and microstructure of nickel based super alloy welds," *Adv. Mater. Res.*, vol. 585, pp. 435–439, 2012. 5.3

[11] J. Veverkova, "EFFECTS OF LONG-TERM HIGH TEMPERATURE EXPOSURE ON THE MICROSTRUCTURE OF HAYNES ALLOY 230," Ph.D. dissertation, University of Leicester, 2010. 5.3, 5.5.1, 5.4

[12] C. J. Boehlert and S. C. Longanbach, "A comparison of the microstructure and creep behavior of cold rolled HAYNES® 230 alloy and HAYNES® 282 alloy," *Mater. Sci. Eng. A*, vol. 528, no. 15, pp. 4888–4898, 2011. 5.3

[13] X. Xie, Y. Zeng, L. Kou, J. Dong, L. M. Pike, and D. Klarstrom, "The Precipitation and Strengthening Behavior of Ni2(Mo,Cr) in HASTELLOY C-22HS Alloy, a Newly Developed High Molybdenum Ni-Base Superalloy," *Superalloys 2008 (Eleventh Int. Symp.*, vol. 2, pp. 799–805, 2008. [Online]. Available: http://www.tms.org/Superalloys/10.7449/2008/Superalloys{_}2008{_}799{_}805.pdf 5.3, 5.5.1, 5.4

[14] X. M. Li, J. W. Bai, P. P. Liu, Y. M. Zhu, X. S. Xie, and Q. Zhan, "Coherent Ni2(Cr, Mo) precipitates in Ni-21Cr-17Mo superalloy," *J. Alloys Compd.*, vol. 559, pp. 81–86, 2013.

[15] H. M. Tawancy and L. M. Al-Hadhrami, "A nanocrystalline Ni2(Cr,Mo) intermetallic with potentially useful combination of properties for gas turbine seal ring applications," *J. Mater. Eng. Perform.*, vol. 21, no. 7, pp. 1374–1379, 2012.

[16] J. W. Bai, Q. Zhan, X. M. Li, and R. Yu, "Enhanced stability of the strengthening phase Ni<inf>2</inf>(Cr,Mo) in Ni-Cr-Mo alloys by adjacent instability," *Comput. Mater. Sci.*, vol. 109, pp. 111–114, 2015. [Online]. Available: http://dx.doi.org/10.1016/j.commatsci.2015.07.011 5.3

[17] M. Raghavan, B. J. Berkowitz, and J. C. Scanlon, "Electron Microscopic Analysis of Heterogeneous Precipitates in Hastelloy C-276," *Metall. Trans. A*, vol. 13, no. 6, pp. 979–984, 1982. 5.3, 5.5.1, 5.4

[18] J. C. Zhao, M. Larsen, and V. Ravikumar, "Phase precipitation and time-temperature-transformation diagram of Hastelloy X," *Mater. Sci. Eng. A*, vol. 293, no. 1, pp. 112–119, 2000. 5.3, 5.5.1

[19] H. M. Tawancy, "Long-term ageing characteristics of Hastelloy alloy X," *J. Mater. Sci.*, vol. 18, no. 10, pp. 2976–2986, 1983. 5.3

[20] K. Mo, G. Lovicu, H.-M. Tung, X. Chen, and J. F. Stubbins, "High Temperature Aging and Corrosion Study on Alloy 617 and Alloy 230,"

J. Eng. Gas Turbines Power, vol. 133, no. 5, p. 052908, 2011. [Online]. Available: http://gasturbinespower.asmedigitalcollection.asme.org/article.aspx?articleid=1429350 5.3

[21] S. Zhao, X. Xie, G. D. Smith, and S. J. Patel, "Microstructural stability and mechanical properties of a new nickel-based superalloy," *Mater. Sci. Eng. A*, vol. 355, no. 1-2, pp. 96–105, 2003. 5.3

[22] N. D. Evans, P. J. Maziasz, R. W. Swindeman, and G. D. Smith, "Microstructure and phase stability in INCONEL alloy 740 during creep," *Scr. Mater.*, vol. 51, no. 6, pp. 503–507, 2004. 5.3

[23] B. A. Pint, J. R. DiStefano, and I. G. Wright, "Oxidation resistance: One barrier to moving beyond Ni-base superalloys," *Mater. Sci. Eng. A*, vol. 415, no. 1-2, pp. 255–263, 2006. (document), 5.3, 5.3, 5.5

[24] B. A. Pint, K. L. More, and I. G. Wright, "Effect of quaternary additions on the oxidation behavior of Hf-doped NiAl," *Oxid. Met.*, vol. 59, no. 3-4, pp. 257–283, 2003. 5.3

[25] F. H. Stott, G. C. Wood, and J. Stringer, "The influence of alloying elements on the development and maintenance of protective scales," *Oxid. Met.*, vol. 44, no. 1-2, pp. 113–145, 1995. 5.3, 5.3

[26] A. Kumar, M. Nasrallah, and D. L. Douglass, "The effect of yttrium and thorium on the oxidation behavior of Ni-Cr-Al alloys," *Oxid. Met.*, vol. 8, no. 4, pp. 227–263, 1974. 5.3

[27] I. A. Kvernest, "The Role of Yttrium in High-Temperature Oxidation Behavior of Ni-Cr-AI Alloys *," *Oxid. Met.*, vol. 6, no. 1, pp. 45–64, 1973. 5.3

[28] A. B. Anderson, S. P. Mehandru, and J. L. Smialek, "Dopant Effect of Yttrium and the Growth and Adherence of Alumina on NickelAluminum Alloys," *J. Electrochem. Soc.*, vol. 132, no. 7, pp. 1695–1701, 1985. [Online]. Available: http://jes.ecsdl.org/content/132/7/1695.abstract 5.3

[29] M. J. Donachie and S. J. Donachie, *Superalloys, A Technical Guide*, 2nd ed., 2002. 5.3

[30] N. Birks, G. H. Meier, and F. S. Pettit, *Introduction to the High Temperature Oxidation of Metals*, 2006. [Online]. Available: http://www.cambridge.org/gb/knowledge/isbn/item1110694/?site{_}locale=en{_}GB 5.4.1

[31] F. Zanner, R. Williamson, R. Harrison, H. Flanders, R. Thompson, and W. Szeto, "Vacuum Arc Remelting of Alloy 718," *Superalloys 718 Metall. Appl.*, pp. 17–32, 1989. [Online]. Available: http://www.tms.org/Superalloys/10.7449/1989/Superalloys{_}1989{_}17{_}32.pdf 5.4.1

[32] M. Cieslak, "The Solidification Behavior of an Alloy 625/718 Variant," *Superalloys 718, 625 Var. Deriv.*, pp. 71–80, 1991. [Online]. Available: http://www.tms.org/Superalloys/10.7449/1991/Superalloys{_}1991{_}71{_}80.pdf 5.4.1

[33] G. Gulliver, "The Quantitative Effect of Rapid Cooling Upon the Constitution of Binary Alloys," *J. Inst. Met.*, vol. 9, pp. 120–157, 1913. 5.4.3

[34] P. D. Jablonski and C. J. Cowen, "Homogenizing a Nickel-Based Superalloy: Thermodynamic and Kinetic Simulation and Experimental Results," *Metall. Mater. Trans. B*, vol. 40, no. 2, pp. 182–186, 2009. [Online]. Available: http://link.springer.com/10.1007/s11663-009-9227-1 5.4.3

[35] D. C. Tung and J. C. Lippold, "Weld Solidification Behavior of Ni-Base Superalloys for use in Advanced Supercritical Coal-Fired Power Plants," *Superalloys 2012*, pp. 563–567, 2012. 5.4.3

[36] Y. Ru, S. Li, Y. Pei, J. Zhou, S. Gong, and H. Xu, "Interdendritic Mo homogenization and sub-solidus melting during solution treatment in the Mo-strengthening single crystal superalloys," *J. Alloys Compd.*, vol. 662, pp. 431–435, 2016. 5.5.1

[37] S. R. Hegde, R. M. Kearsey, and J. C. Beddoes, "Designing homogenization-solution heat treatments for single crystal superalloys," *Mater. Sci. Eng. A*, vol. 527, no. 21-22, pp. 5528–5538, 2010. [Online]. Available: http://dx.doi.org/10.1016/j.msea.2010.05.019 5.5.1

[38] C. Sims, "Prediction of Phase Composition," in *Superalloy II*, C. Sims, N. Stoloff, and W. Hagel, Eds. New York: John Wiley and Sons, 1987, pp. 217–220. 5.5.1

[39] J. Mihalisin and D. Pasquine, "Phase Transformations in Nickel-Base Superalloys," *Int. Symp. Struct. Stab. Superalloys*, pp. 134–170, 1968. [Online]. Available: http://www.tms.org/Superalloys/10.7449/1968/Superalloys{_}1968{_}134{_}170.pdf 5.5.1

[40] R. Darolia, D. Lahrman, and R. Field, "Formation of Topologically Closed Packed Phases in Nickel Base Single Crystal Superalloys," *Superalloys*

1988 (Sixth Int. Symp., no. January 1988, pp. 255–264, 1988. [Online]. Available: http://www.tms.org/Superalloys/10.7449/1988/Superalloys{_}1988{_}255{_}264.pdf 5.4

Chapter 6: Conclusions

This work was focused on the advancement of understanding how materials behave with respect to sCO_2 exposure. The stated objectives were assessment of the corrosion performance of commercial alloys, the investigation of mechanical properties at elevated temperatures and the development of novel alloys.

The corrosion analysis of alloys intended for use in sCO_2, focused on the more established alloys in the power industry, alloy 800H, HR120 and IN625. All alloys, in all conditions, showed formation of a continuous and adherent chromia scale, and no evidence of breakaway corrosion was found. The TEM analysis for IN625 and HR120 revealed the presence of silica in the chromia layer, which was attributed to the early preferential oxidation of silicon, followed by an inward growth of the chromia. The influence of exposure time on the scale thickness was analyzed in the alloy 800H, where for the exposure times of 200 and 600 hrs the material showed little change. Common to all alloys were both a depletion zone underneath the scale as well as recrystallization zone, which was collocated with it.

In order to understand the influence that sCO_2 has on the recrystallization zone, for 800H specifically, comparison exposures were undertaken in air and argon, at the same temperatures and times. It was found that the sCO_2-exposure did indeed result in a wider RX zone, which led to the conclusion that both the local chromium depletion and epitaxial growth stress from the oxide film may have contributed to

its existence. In general, a higher density of internal carburization than in air- or argon-exposed samples was found in all alloys as well. Here the causes may be a combination of the available carbon, after diffusion through the scale, and the high density of grain boundaries in the RX zone, acting as diffusion pathways for the carbon to the base-metal. Alloys IN625 and HR120 were exposed at 550 ℃ for 1000 hrs, which did result in similar microstructures as exposures at 650 ℃ for 800H. In particular, the alloy HR120 showed similar presence of internal carburization as 800H did, both alloys being Fe-Ni-based alloys. These are known to have higher affinity to carbon compared to Ni-based alloys, such as IN625, without considerable amount of iron.

Another part of this work focused on the aspect of hot workability, when these alloys are being formed into final shapes for use in sCO_2 systems. The Ni-based alloys tested were Haynes 230, Haynes 214 and Inconel 740H, which were all tested hot-deformed at conditions expected in industrial environments. This study focused on the materials in their as-received condition, before final heat treatment, solutionizing or aging, to demonstrate an in-line processing to the final product. Optimum working ranges based on strain rate and temperature were outlined for all alloys, which allowed for avoidance of areas with irregular or unstable flow behavior. Further, analysis of the flow stress curves and the associated stress-strain data showed that material behavior is markedly different from the same alloys tested in different heat-treatment conditions. It was assumed that chemical differences from undissolved secondary phases, as well as the initial grain microstructure played a major role.

Finally, this work studied the complete process of alloymaking, over design and

making, to processing and testing. The motivation was to design an alloy that more directly meets the requirements for sCO_2 uses. The base alloying concept is based on four different alloy systems, and their associated major beneficial features. These alloys are Haynes 230, Haynes 214 and Inconel 740H, with high temperature oxidation resistance, solid-solution and creep strength as well as age-hardenability as the main desirable features. With the use of thermodynamic modeling, the stability of alloys and phases were analyzed, and initial homogenization heat-treatments derived. First alloy batches were cast, and the as-cast microstructure analyzed, in order to verify computationally derived results, showing good agreement. Larger castings were then made for subsequent hot-rolling for samples for mechanical and corrosion testing. Wrought alloy samples were solution-treated and aged in order to study the evolution of the microstructure. The material showed good response to the proposed treatment in terms of dissolving γ'-phase for precipitation during aging. Lastly, the mechanical properties of the studied alloy design at high temperatures showed strain rate and temperature ranges, which were most suitable for subsequent forming.

In conclusion, the exposure of Ni-based alloys in sCO_2 showed that all alloys formed similar, stable chromium oxide phases on the surface. With iron as an alloying element in the base-metal, internal carburization occured, which increased with longer exposure times. Comparisons with exposures in air and argon showed that sCO_2 increased the amount of internal carburization. The hot-working behavior of the tested Ni-based alloys suggested clear regions for good workability when forming these alloys under expected conditions. It should be noted that the activation energy for plastic flow was measurably lower than for other comparable alloys. The alloy

development showcased a fully integrated approach from alloy conception to property testing, based on the motivation of designing an alloy best suited for sCO_2 use. The preliminary results of the mechanical and corrosion testing were promising and comparable with other targetted candidate alloys.

Chapter 7: Future work

The sCO_2-exposure testing of commercial alloys will be continued, and the database of available information on the performance further populated. Based on sufficient early data, it will be necessary to build prediction models for longer-term corrosion behavior as well as the creep life assessments. An increased understanding of the underlying principles that govern the corrosion reactions that are occurring will be necessary. Similarly, microstructural and compositional changes in response to the exposure need to be investigated further, not least due to their influence on creep properties and rupture strength.